Observational Aspects of Hard X-ray Polarimetry

A thesis submitted in partial fulfilment of
the requirements for the degree of

Doctor of Philosophy

by

Tanmoy Chattopadhyay

(Roll No. 11330008)

Under the guidance of

Dr. Santosh V. Vadawale

Associate Professor
Astronomy & Astrophysics Division
Physical Research Laboratory, Ahmedabad, India.

DISCIPLINE OF PHYSICS

INDIAN INSTITUTE OF TECHNOLOGY GANDHINAGAR

2015

to

my family

Declaration

I declare that this written submission represents my ideas in my own words and where others' ideas or words have been included, I have adequately cited and referenced the original sources. I also declare that I have adhered to all principles of academic honesty and integrity and have not misrepresented or fabricated or falsified any idea/data/fact/source in my submission. I understand that any violation of the above will be cause for disciplinary action by the Institute and can also evoke penal action from the sources which have thus not been properly cited or from whom proper permission has not been taken when needed.

(Signature)

(Name: Tanmoy Chattopadhyay)

(Roll No: 11330008)

Date: November 26, 2015

CERTIFICATE

It is certified that the work contained in the thesis titled **"Observational Aspects of Hard X-ray Polarimetry"** by **Mr. Tanmoy Chattopadhyay** (Roll No. 11330008), has been carried out under my supervision and that this work has not been submitted elsewhere for a degree.

Dr. Santosh V. Vadawale
(Thesis Supervisor)
Associate Professor,
Astronomy & Astrophysics Division
Physical Research Laboratory,
Ahmedabad, India.

Date:

Acknowledgements

First and foremost, I would like to express my sincere gratitude to my advisor Dr. Santosh Vadawale for his continuous support in my Ph.D study and related research. His guidance helped me throughout the time of PhD and writing of this thesis.

Besides my advisor, I would like to thank the rest of my thesis committee: Prof. N. M. Ashok, Prof. Janardhan Padmanabhan, and Dr. Sachindra Naik, for their insightful comments and encouragement.

My sincere thanks also goes to Prof. A. R. Rao, Prof. Dipankar Bhattacharya, who provided me an opportunity to join Astrosat-CZTI team, giving me access to the laboratory and research facilities. Without their precious support it would not be possible to conduct this research. I would like to thank other team members of the CZTI team Dr. Varun Bhalerao, Rasika, Pramod, Kutty, Malkar sir, Amir, Anish, Nilkanth, Rakesh, Mithun and others for their continuous support in my research work in PRL, TIFR and IUCAA.

I would like to thank all the faculty members in Astronomy & Astrophysics division, PRL, specially Prof. B. G. Anandrao, Prof. T. Chandrasekhar, Dr. Ashok Singal, Prof. U. C. Joshi, Prof. H. O. Vats, Prof. N. M. Ashok, Prof. D. P. K. Banerjee, Prof. P. Janardhan, Prof. K. S. Baliyan, Dr. A. Chakraborty, Dr. Sachindra Naik, Dr. S. Ganesh, Dr. Mudit Srivastava and Dr. V. Venkataraman for their useful comments and suggestions and continuous support during my PhD tenure.

I thank my fellow labmates in PRL – Mr. Shanmugam M., Mr. Shivkumar Goyal, Mithun, Rishab, Arpit, Tinkel, Mr. A. B. Shah and others for the stimulating discussions and helping me out in my research work.

Also I thank my batchmates and friends for their continuous support and all the fun we have had in the last five years. I am grateful to Priyanka, Arko, Monojit, Balaji, Pragya and Golu, Naveen, Sneha, Shweta and others for spending valuable time with me in the last five years, which I will cherish throughout my life. I take this opportunity to thank my B.Sc. and M.Sc. batchmates and friends – Rupomoy, Abhisek, Sudip, Rajib, Dhrubo, Debraj, Someswar, Kousik K., Kousik B., Tanmoy R., Suman, Saptorshi, Abhivav, Avdesh, Mayukh da, Aniruddha da, Biswarup, Sibu, Jitu, Bablu who had directly and indirectly helped me achieved this goal.

I am grateful to Prof. Hiralal Yadav in B.H.U., Prof. Bhabani Prasad Mandal in B.H.U., and Prof. Ashok Banerjee in T.D.B. college for enlightening me the first glance of research. I am thankful to all my teachers especially Amitabha sir

and Phonibhusan sir for teaching me not only the academic subjects but also the important lessons in life.

Last but not the least, I would like to thank my family: my parents and to my sisters for their encouragement, support and attention throughout my life.

(Tanmoy Chattopadhyay)

Abstract

Sensitive polarization measurements in X-ray may address a wealth of astrophysical phenomena, which so far remain beyond our understanding through available X-ray spectroscopic, imaging, and timing studies. Though scientific potential of X-ray polarimetry was realized long ago, there has not been any significant advancement in this field for the last four decades since the birth of X-ray astronomy. The only successful polarization measurement in X-rays dates back to 1976, when a Bragg polarimeter onboard OSO-8 measured polarization of Crab nebula. Primary reason behind the lack in progress is its extreme photon hungry nature, which results in poor sensitivity of the polarimeters.

Recently, in the last decade or so, with the advancement in detection technology, X-ray polarimetry may see a significant progress in near future, especially in soft X-rays with the invention of photoelectron tracking polarimeters. Though photoelectric polarimeters are expected to provide sensitive polarization measurements of celestial X-ray sources, they are sensitive only in soft X-rays, where the radiation from the sources is dominated by thermal radiation and therefore expected to be less polarized. On the other hand, in hard X-rays, sources are expected to be highly polarized due to the dominance of nonthermal emission over its thermal counterpart. Moreover, polarization measurements in hard X-rays promises to address few interesting scientific issues regarding geometry of corona for black hole sources, emission mechanism responsible for the higher energy peak in the blazars, accretion geometry close to the magnetic poles in accreting neutron star systems and acceleration mechanism in solar flares. Compton polarimeters provide better sensitivity than photoelectric polarimeters in hard X-rays with a broad energy band of operation. Recently, with the development of hard X-ray focusing optics e.g. NuSTAR, Astro-H, it is now possible to conceive Compton polarimeters at the focal plane of such hard X-ray telescopes, which may provide sensitive polarization measurements due to flux concentration in hard X-rays with a very low background. On the other hand, such a configuration ensures implementation of an optimized geometry close to an ideal one for the Compton polarimeters. In this context, we initiated the development of a fo-

cal plane Compton polarimeter, consisting of a plastic scatterer surrounded by a cylindrical array of CsI(Tl) scintillators. Geant−4 simulations of the planned configuration estimates 1% MDP for a 100 mCrab source in 1 million seconds of exposure. Sensitivity of the instrument is found to be critically dependent on the lower energy detection limit of the plastic scatterer; lower the threshold, better is the sensitivity. In the actual experiment, the plastic is readout by a photomultiplier tube procured from Saint-Gobain. We carried out extensive experiments to characterize the plastic especially for lower energy depositions. The CsI(Tl) scintillators are readout by Si photomultipliers (SiPM). SiPMs are small in size and robust and therefore provide the compactness necessary for the designing of focal plane detectors. Each of the CsI(Tl)-SiPM systems was characterized precisely to estimate their energy threshold and detection probability along the length of the scintillators away from SiPM. Finally, we integrated the Compton polarimeter and tested its response to polarized and unpolarized radiation and compared the experimental results with Geant−4 simulation.

Despite the growing realization of the scientific values of X-ray polarimetry and the efforts in developing sensitive X-ray polarimeters, there has not been a single dedicated X-ray polarimetry mission planned in near future. In this scenario, it is equally important to attempt polarization measurements from the existing or planned instruments which are not meant for X-ray polarization measurements but could be sensitive to it. There have been several attempts in past in retrieving polarization information from few of such spectroscopic instruments like RHESSI, INTEGRAL-IBIS, INTEGRAL-SPI. Cadmium Zinc Telluride Imager (CZTI) onboard Astrosat, India's first astronomical mission, is one of such instruments which is expected to provide sensitive polarization measurements for bright X-ray sources. CZTI consists of 64 CZT detector modules, each of which is 5 mm thick and 4 cm × 4 cm in size. Each CZT module is subdivided into 256 pixels with pixel pitch of 2.5 mm. Due to its pixelation nature and significant Compton scattering efficiency at energies beyond 100 keV, CZTI can work as a sensitive Compton polarimeter in hard X-rays. Detailed Geant−4 simulations and polarization experiments with the flight configuration of CZTI show that

CZTI will have significant polarization measurement capability for bright sources in hard X-rays.

CZTI is primarily a spectroscopic instrument with coded mask imaging. To properly utilize the spectroscopic capabilities of CZT detectors, it is important to generate accurate response matrix for CZTI, which in turn requires precise modelling of the CZT lines shapes for monoenergetic X-ray interaction. CZT detectors show an extended lower energy tail of an otherwise Gaussian line shape due to low mobility and lifetime of the charge carriers. On the other hand, inter-pixel charge sharing may also contribute to the lower energy tail making the line shape more complicated. We have developed a model to predict the line shapes from CZTI modules taking into account the mobility and lifetime of the charge carriers and charge sharing fractions. The model predicts the line shape quite well and can be used to generate pixel-wise response matrix for CZTI.

Keywords: X-ray polarimetry, Compton scattering, Hard X-ray telescopes, Geant−4 simulation, Instrumentation, Astrosat, Cadmium Zinc Telluride Imager (CZTI), Response matrix, Cygnus X-1, Crab pulsar.

Contents

List of Figures

List of Tables

Chapter 1

Introduction

X-ray astronomy, a branch of astrophysics, deals with the detection of high energy electromagnetic radiation from celestial astrophysical sources. Since high energy photons or X-rays do not reach the surface of earth owing to absorption by earth's atmosphere, to observe the sources in X-rays, the instruments have to be taken above the atmosphere which makes the field of X-ray astronomy quite challenging. One of such attempts back in 1949, detection of X-rays from solar corona, marks the beginning of X-ray astronomy. Despite this fact, it took fifteen years for detection of X-rays from the first extrasolar source, Scorpius X-1 which in led to the birth of X-ray astronomy in true sense. Scorpius X-1 was found to be a neutron star binary system. Such binary systems, where one of the companions is a compact object (e.g. black hole, neutron star, or white dwarf) are the potential sources for X-ray radiation. The release of large amount of gravitational energy due to accretion of matter around the compact object makes these systems bright in X-rays. Isolated rotating pulsars are also known to radiate in high energies converting their rotational energy into X-ray radiation. Study of X-ray astronomy, therefore, allows understanding of accretion process around the compact objects and the related emission mechanism, geometry of the sources at the close vicinity of emission region, behaviour of matter in extreme gravitational and magnetic field. Since the birth of X-ray astronomy, X-ray spectroscopy (detection of photon energy), X-ray timing (photon timing properties), and X-ray imaging (based on spatial information photon carries) have met significant advancement, while the study of the fourth parameter of radiation i.e. polarization or the orientation of the electric field vector, remains majorly unexplored. However, the fact that polarization information of the sources single-handedly or in unison with other radiation properties might lead to a better understanding of various physical processes and their geometries, was well known since a long time.

The only successful measurement of polarization in X-ray astronomy dates to 1976 when an X-ray polarimeter onboard OSO-8 mission, measured $\sim$19% polarization at 2.6 keV and 5.2 keV for the Crab nebula [1, 2]. There were attempts to measure X-ray polarization, with the same polarimeter as well as few other space-borne and balloon-borne experiments [3–9] but these could yield only upper-limits at best, due to low sensitivity of these measurements. After these initial efforts, no real experiments to measure X-ray polarization from celestial X-ray sources were carried out for more than three decades. Though there were some attempts to design and build the X-ray polarimeters (e.g. [10, 11]) and few concept proposals for space missions (e.g. XPE, [12]; PLEXAS, [13]), only one instrument (SXRP, [14]) was actually selected for flight onboard Russian mission Spectrum X-Gamma, but unfortunately this mission could not materialize. However, in the absence of any dedicated X-ray polarimetry experiment, in the last decade there have been few attempts to measure polarization of bright X-ray sources by standard spectroscopic instruments which have significant polarization measurement capability. To name a few most important results are the detection of high polarization of Cygnus X-1 and Crab nebula by IBIS and SPI onboard INTEGRAL [15–18]. However, polarimetric sensitivity of these instruments being on the lower side, those detections are far from being conclusive. Therefore, apart from these coarse polarization detections, there have not been any dedicated X-ray polarization measurement experiments and this lack is mainly due to the very low sensitivity of polarimetry compared to spectroscopy, imaging or timing; which results due to extremely photon hungry nature of the X-ray polarimetry.

In the next section, we briefly describe the scientific potential of X-ray polarimetry in general, followed by a discussion on the polarization measurement techniques. The thesis work presented here, is broadly based on hard X-ray polarimetry; in Sec. 1.3, the importance of hard X-ray polarimetry, both from scientific and technical point of view, has been discussed elaborately including an overview of the thesis.

1.1 Science Drivers for X-ray Polarimetry

The importance of X-ray polarization measurement has been well known as these measurements provide two independent parameters, i.e. degree and angle of polarization characterizing the incoming radiation from any X-ray source. These parameters can provide a unique opportunity to study the behavior of matter and radiation under extreme magnetic and gravitational fields. Scientific importance of X-ray polarimetry has been extensively discussed in literature [19–21]. Here we provide a brief outline of various classes of X-ray sources for which X-ray polarimetry observations can provide significant insights.

Binary black Hole Systems: For accreting black hole systems, the lower energy flux is dominated by thermal radiation, which is polarized owing to scattering in the disk atmosphere, where the degree of polarization strongly depends on the inclination of the system. Polarization angle is expected to be parallel or perpendicular to the disk axis depending on the optical depth. Recent theoretical and simulation studies [22] suggest that due to GR effects e.g aberration and gravitational dragging (in case of Kerr black hole), there would be a change in polarization angle for each photon at infinity depending upon the emission location from the disk. This results in a depolarizing effect when all the photons are added up at infinity. The depolarizing effect is more prominent for the photons emitted closer to the black hole, lower inclination and higher spin of the black hole. Closer to the black hole, temperature of the disk is higher, and therefore emits high energy photons. Therefore, polarization is expected to be energy dependent with a smooth swing in polarization direction from parallel to the disk towards its perpendicular direction or vice versa depending upon the optical depth. At lower energies ($E \leq 0.1$ keV), the degree of polarization is expected to be same as that for flat space time, but with the increase in energy ($0.1 - 10$ keV), polarization degree decreases. Effect of returning radiation which is the radiation deflected by the strong gravity of the black hole and scatters off the disk before reaching the distant observer is also significant in the overall change in the polarization degree and polarization angle as a function of energy [23]. Polarization measurements, therefore, in thermal state may be extremely useful in probing properties of inner accretion flow and constraining the disk inclination and black hole spin.

At energies beyond 10 keV, the flux is dominated by the coronal emission. Therefore, polarimetry in low hard state can give vital information about the corona geometry. Schnittman and Krolik [24] investigated the polarimetric signatures for various corona geometries (see Fig. 1.1). For a homogeneous sandwich corona, at higher inclination, the photons move through the disk and are vertically polarized with respect to the disk plane. While moving parallel to the disk, they are inverse Compton scattered multiple times and boosted to very high energies. This causes polarization to be energy dependent. At 100 keV, the expected

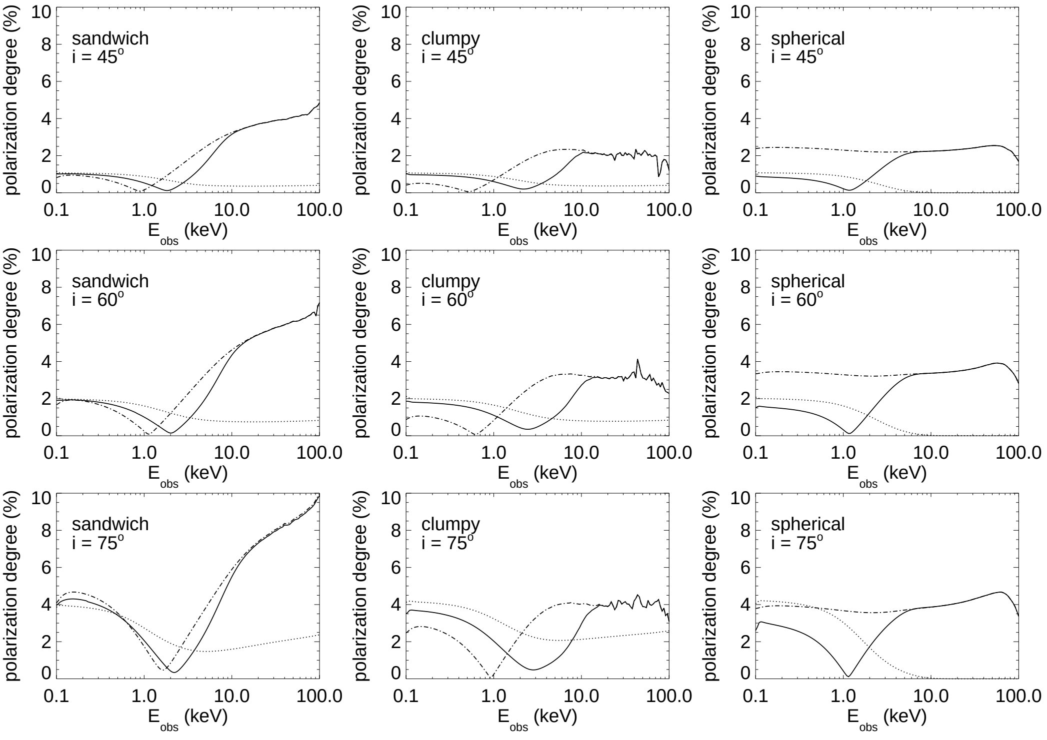

Figure 1.1: Polarization characteristics for various black hole coronal geometries as a function of observed energy and inclination. The dotted lines represent disk emission, whereas the dot-dashed and solid lines represent coronal and total (disk+corona) emission respectively. The figure has been taken from [24]

degree of polarization is about 10% at high inclination, whereas for lower inclination, fraction of polarization decreases. On the other hand, for an inhomogeneous clumpy corona, the polarization decreases to $3-4\%$ for the same energy. This is because the photons after being inverse Compton scattered multiple times in one spherical clumpy corona, emerge in all directions, consequently decreasing the net polarization. For a simple spherical corona geometry, the expected polarization fraction is about 4% at 100 keV, almost independent of the inclination because of the spherical symmetry. Polarization measurements in low hard states of black hole systems, therefore, will be a key to probe the geometries of corona.

At energies beyond 100 keV, the radiation from black hole systems in its low hard state is supposed to be of jet origin [25–27]. Recent findings of high polarization measured for high mass black hole binary, Cygnus X-1, at energies spanning from few hundreds of keV to few MeVs [15, 16] also suggests the jet origin of the hard X-ray emission. However, multi-wavelength SED modeling of Cygnus X-1, shows insignificant contribution of jet in hard X-rays [28]. On the other hand, there are studies reported in literature suggesting radiation in hard X-rays to originate from lepto-hadronic corona of black holes due to synchrotron radiation, predicting radiation to be highly polarized independent of its state [29]. Careful polarization measurements of black hole systems in both low hard state and high soft state may lead to a proper understanding of hard X-ray origin of these sources.

Active Galactic Nuclei: Active Galactic Nuclei (AGNs) emit thermally in UV from the disk which is expected to be Comptonized by corona giving rise to a powerlaw component in their spectra. The scattered coronal emission is polarized, around 8%, higher compared to that of the stellar massive black hole systems. This is due to the fact that the UV photons from the disk, in order to upscatter to energies > 10 keV, move parallel to the disk and corona suffering a large number of interactions [24]. Spectro-polarimetric studies are expected to be useful for investigating corona geometry in details by constraining the number of clumps and their over-density especially in case of clumpy corona geometry. The disk photons may also be scattered by the molecular torus. Thus, X-ray polarimetry may as well constrain the geometry of the torus which is still poorly known [30]. Polarization measurement of the reflected radiation from the disk or the torus may therefore complement the reverberation studies for AGNs to study the geometry of the reflector by estimating the time delay between the direct and reflected component of radiation [31].

Blazars: Broadband multi-wavelength polarimetry for blazars may probe the origin of second characteristic emission peak in their spectral energy distribution. For low energy peaked blazars, the low energy peak occurs at optical regime whereas the high energy peak occurs in MeVs. The low energy peak is expected to be due to synchrotron radiation of the relativistic electrons, whereas the high energy peak, according to the Synchrotron Self Compton model (SSC, [32]) is due to the inverse Compton scattering of the synchrotron photons off the relativistic electrons itself. Polarization fraction for synchrotron radiation is higher ($>$ 60% for uniform magnetic field) compared to the SSC radiation ($>$ 30%), where the polarization fraction depends on the spectral index of the electron energy distribution. However, in both cases polarization directions in optical light and X-rays are expected to be identical. On the other hand, in External Compton model (EC), where it is believed that for high energy peak the seed photons are the accretion disk photons or the emission from broad line region or from dusty molecular torus instead of the synchrotron photons (as in SSC model), the polarization fraction is below 5% [33].

For high energy peaked blazars, the low energy flux peaks in X-ray band whereas the high energy peak occurs in GeV to TeV range. Polarization measurement of Synchrotron X-ray radiation can indicate the structure of the magnetic field close to the base of the jet. High degree of polarization close to the theoretical values would imply the presence of uniform magnetic field.

Besides the leptonic models, there exists a completely different approach based on lepto-hadronic models which can produce equally good fits to the SEDs of blazars. Polarization is one of the possible diagnostics to distinguish between these two approaches. In case of hadronic models, whereas the source of low energy peak is the synchrotron radiation from ultra-relativistic electrons same as that for leptonic models, the high energy peak is because of the high energy proton induced radiation mechanisms. Because of the dominance of synchrotron radiation in hadronic models, a high polarization is expected compared to that for leptonic models, where the radiation is either because of SSC emission or EC emission [34].

Neutron Stars: X-ray polarimetry may lead us to a better understanding of emission mechanism and emission geometry of isolated pulsars, accreting pulsars, magnetars and behaviour of matter in strong magnetic fields [35].

The details of emission mechanism and emission site for rotation powered pulsars have been a subject of debate. Controversy is whether the high energy pulsar radiation originates directly above the polar cap (polar cap model, [36]), or in the outer magnetosphere (outer gap model, [37]), or all the way from the polar cap to the light cylinder along the last open field line (slot gap model, [38]). All these models predict quite distinct phase dependent polarization properties due to the rotation of the pulsar. Fig. 1.2 shows variation of optical linear polarization with pulse phase for Crab pulsar [39, 40], along with the predictions of these models. Therefore, phase resolved polarimetry can test these models and help in understanding the emission sites and emission mechanisms in isolated X-ray pulsars.

In case of magnetars, the magnetic field is extremely high (10^{14-15} G). such high magnetic field powers high energy radiation through seismic activity and heating of the stellar interior [41]. Radiation emitted in such strong field should be highly polarized. Magnetar's persistent emission is faint in soft X-ray, however there is a bright hard X-ray tail ($20-100$ keV). This range is promising for hard X-ray polarimetry, as it will be helpful in understanding the nature of magnetars and the physical processes in extremely strong magnetic fields.

In accretion-powered pulsars, theoretical models predict high polarization owing to the high magnetic field (10^{12-13} G) in those systems. Polarization is expected to be maximum for emission perpendicular to the magnetic field. Therefore, phase resolved polarization can be used to determine the beam shape of pulsar. For example, for pencil beam the oscillations in polarization fraction are

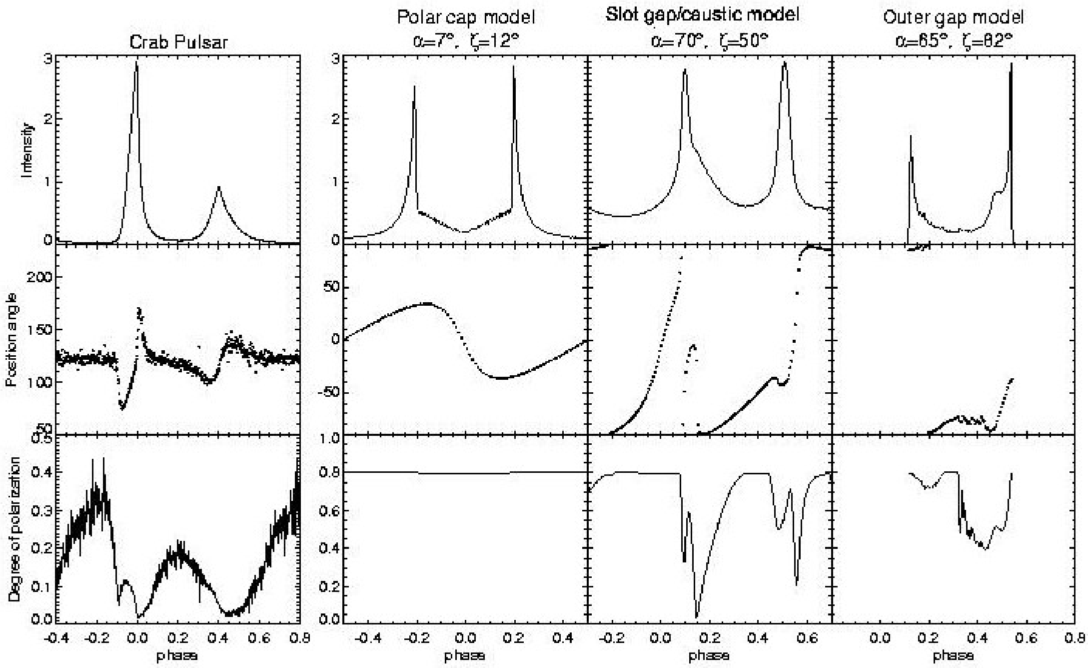

Figure 1.2: Phase resolved optical polarimetry of Crab pulsar along with the predictions from various pulsar models [39, 40]. The figure has been taken from [35]

expected to be out of phase with pulse phase, whereas for fan beam the opposite case is expected [42]. It will in turn help in understanding the accretion flow to the magnetic poles of the pulsars. This effect is more prominent at energies near cyclotron resonances. Many accretion-powered pulsars have been found to exhibit cyclotron features in energy range 15-50 keV. A polarimeter sensitive in the energy band near cyclotron energies will be able to distinguish between the pencil and fan radiation patterns in these systems.

Millisecond X-ray pulsars are accretion-fed systems where the pulsar is spun up to high rotation speed with period of few milliseconds due to accretion. Polarization at higher energies in these systems derives from Compton scattering of photons in accretion shock [43] or possibly from accretion disk [44]. Polarization measurements for these sources may test these models and put tighter constraints on geometrical parameters like orbital and dipole axis inclination in the models.

Gamma Ray Bursts: Gamma Ray Bursts (GRBs) are brief intense flashes of gamma rays at cosmological distances (prompt emission) followed by radiation in

X-rays, UV, and higher wavelengths (afterglow). Though radiation from GRBs is expected to be from outflows moving towards us with relativistic speed, the emission mechanism for prompt emission is poorly understood. There are various theories for prompt emission,namely, synchrotron emission from relativistic electrons energized in internal shocks within jet either in globally ordered magnetic field derived from the central engine (Synchrotron Ordered or SO model) or in random magnetic field generated in the shock plane within the jet (Synchrotron Random or SR model). Comptonization of the soft photons (Compton Drag or CD model) by the relativistic jet is also a possible explanation for prompt emission. Polarization is expected to be high in SO model except for a special case where line of sight coincides with the jet axis, as the local polarization vectors are axisymmetric around the line of sight and therefore nullify each other. On the other hand, polarization in the SR and CD model will be dependent on the geometry of the viewing angle, as for certain viewing angles, net polarization remains. Recently, Toma et al. (2008), [45] showed that statistical distribution of GRB polarizations may efficiently lift the degeneracy of these theoretical models. On the other hand, in case of poynting flux dominated flow [46, 47] as against to the matter dominated outflow, the electrons, energized due to reconnection of magnetic field, emit synchrotron radiation. Since synchrotron radiation is intrinsically polarized, we expect high polarization in GRB prompt emission.

Afterglow, on the other hand, is expected to be due to synchrotron emission of electrons accelerated in shocks due to interactions of jet with the surrounding medium. Afterglow polarization measurements and its time variability may test the GRB jet structure and magnetic field geometry.

Solar Flares: Solar flares are the powerful events due to magnetic reconnection in Sun's corona, accelerating the electrons towards the chromosphere. Radiation at soft X-rays is due to thermal heating at the reconnection site and are therefore expected to be unpolarized in nature. However, because of anisotropies in electron distribution the thermal radiation may have low level of polarization [48].

On the other hand, hard X-ray radiation is due to non-thermal Bremsstrahlung emission by high energy electrons and thus expected to be highly polarized with

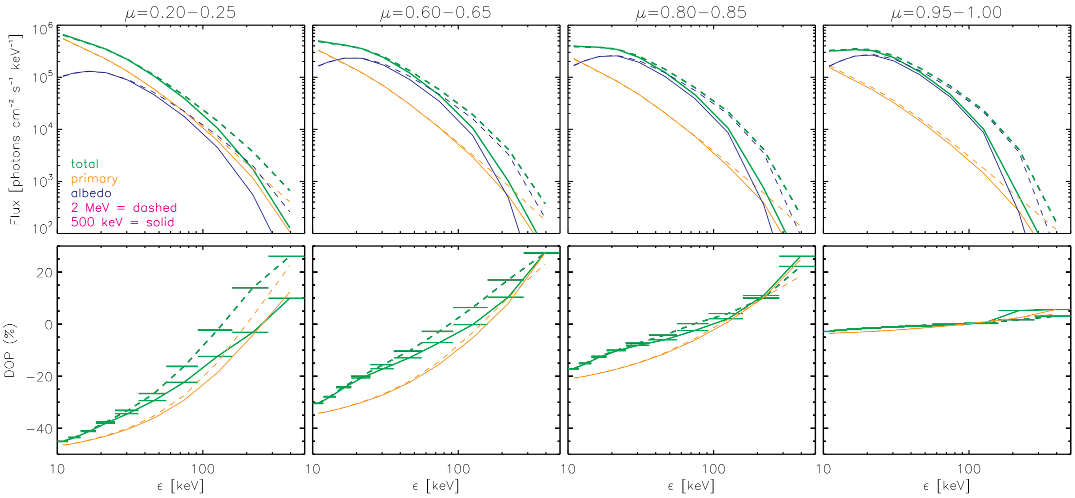

Figure 1.3: Variation of flux (top row) and spatially integrated polarization (bottom row) with observed energy for an extremely beamed electron distribution. μ ($= \cos\theta$) refers to the direction of emission where $\theta = 0°$ is the local solar vertical. Green, orange and blue denote the total source, primary and albedo components respectively, whereas the solid and dashed lines refer to electron cut off energy of 500 keV and 2 MeV respectively. The figure has been taken from [49]

degree of polarization depending on the beaming of electron beam, magnetic field structure, backscattering of the photons from the photosphere [49, 50] (see Fig. 1.3) etc. Because of sufficient photon flux in X-rays, solar flares are the potential targets for X-ray polarimetry, specially in hard X-rays.

Besides providing an opportunity to deal with these exciting astrophysical problems, X-ray polarimetry may also be useful in testing few fundamental physical phenomena as well. For example, QED effects in very high magnetic field e.g. in magnetars, is expected to exhibit observational effects in terms of change in polarization degree and angle due to vacuum resonance and vacuum birefringence. Presence of Axion Like Particles (ALP), a prediction of beyond standard model, can also be tested by means of X-ray polarimetry observations.

1.2 X-ray Polarization Measurement

Polarization is not a directly measurable quantity, therefore, its measurement requires conversion to some observable quantity while interacting with the detector material. The common feature of any X-ray interaction with matter, is the dependence of interaction cross-section on polarization, giving rise to a variable intensity (number of photons or electrons converted) with position (or azimuthal angle with respect to some detector reference axis) on the detector plane. Based on this, there are three basic techniques to extract polarization information from sources, namely, Compton / Rayleigh scattering, photo-electron imaging and Bragg reflection [51], where the variability in intensity is fitted with a suitable modulation function, with amplitude of modulation (measure of the degree of polarization) being obtained from non-linear regression. In all these processes the detected polarization signal on the detector plane can be described as

$$S = \bar{S}[1 + a_0 \cos 2\,(\phi - \phi_0)], \tag{1.1}$$

where, ϕ is an angle with respect to the detector reference axis on the detector plane, perpendicular to the photon incidence direction and $\bar{S}$ is the mean number of events / counts in ϕ bins. It is evident from Eq. 1.1, that the distribution of the events, as discussed earlier, is modulated with ϕ having an amplitude a_0 and position angle of ϕ_0, where a_0 is proportional to the degree of linear polarization.

However, in presence of noise (which we assume to be of Poisson distribution), there is a certain probability, $P(a, \phi)$, to measure an amplitude of a and phase ϕ, even though the actual amplitude and position angle in the source signal are a_0 and ϕ_0 respectively, given by,

$$P(a, \phi) = \frac{Na}{4\pi} \exp\left[-\frac{N}{4}\left(a^2 + a_0^2 - 2aa_0 \cos(\phi - \phi_0)\right)\right], \tag{1.2}$$

where, $N(= n\bar{S}$, n is the number of ϕ bins) is the total number of detected events. Since, modulation is always positive definite, even if the source is unpolarized (a_0 = 0), there is still a finite probability to measure an amplitude a (i.e. $P(a) \neq 0$).

From this the sensitivity or the minimum polarization that the instrument will be able to detect, can be established by estimating the value of modulation amplitude for unpolarized source signal ($a_0 = 0$), which is exceeded by chance with 1% probability, i.e.

$$\frac{N}{2} \int_{a_{1\%}}^{\infty} a \exp\left[-\frac{Na^2}{4}\right] da = 0.01 \,. \tag{1.3}$$

Solving Eq. 1.3, we get modulation amplitude for unpolarized source,

$$a_{1\%} = \frac{4.29}{\sqrt{N}}. \tag{1.4}$$

Eq. 1.4 leads to the Minimum Detectable Polarization (MDP) or the sensitivity of the instrument in terms of source and background event rate (R_{src} and R_{bkg} respectively) and modulation amplitude for 100% polarized signal (μ_{100}), derived in the absence of background,

$$MDP_{99\%} = \frac{4.29}{R_{src}\,\mu_{100}}\sqrt{\frac{R_{src}\,+\,R_{bkg}}{T}}, \tag{1.5}$$

where, T is the total exposure time for polarization measurement. In order to study polarization of astrophysical sources, MDP should always be smaller than the degree of polarization to be measured. For a given source and exposure time MDP is small for high μ_{100} and high efficiency, values of which are different for different polarization measurement techniques.

Once the modulation curve is obtained for any unknown polarized radiation, the conventional way to measure polarization fraction, P, is to first obtain the modulation amplitude from the modulation curve (with C_{max} and C_{min} being the maximum and minimum number of counts in the modulation curve),

$$\mu = \frac{C_{max} - C_{min}}{C_{max} + C_{min}}, \tag{1.6}$$

and then normalize it with respect to the modulation factor for 100% polarized beam, μ_{100}, which is typically estimated by simulation or experimentally,

$$P = \frac{\mu}{\mu_{100}}. \tag{1.7}$$

For any polarization measurement technique, μ_{100} and efficiency should be as high as possible to have sensitivity well above the expected degree of polarization from the celestial astrophysical sources. In the following sections, we briefly describe these techniques.

1.2.1 Scattering polarimetry

Scattering polarimetry is based on Compton or Rayleigh scattering, where the photon is scattered off an electron and imparts either a small energy to the electron (Compton scattering) or travels with same energy (Rayleigh scattering). The differential cross-section for Compton scattering of a polarized X-ray beam is given by Klein-Nishina formula [52],

$$\frac{d\sigma}{d\Omega} = \frac{r_e^2}{2}\left(\frac{E^{'}}{E}\right)^2\left(\frac{E^{'}}{E} + \frac{E}{E^{'}} - 2\sin^2\theta\cos^2\phi\right), \tag{1.8}$$

where E and $E^{'}$ are energies of incident and scattered photons respectively given by,

$$\frac{E^{'}}{E} = \frac{1}{1 + \frac{E}{mc^2}(1 - \cos\theta)}. \tag{1.9}$$

r_e is the classical electron radius, m is the mass of electron, θ is the polar scattering angle, and ϕ is the azimuthal scattering angle i.e. the angle between the electric vector of the incident photon and the scattering plane. Cross-section for Rayleigh scattering is obtained from Eq. 1.8 with $E^{'}$ made equal to E. In both Compton and Rayleigh scattering, the distribution of the scattered photons with azimuthal angle ϕ is modulated as $\cos^2\phi$. It is evident that the amplitude of modulation is maximum for polar scattering angle of 90°, however, the probability of scattering of photons is found to be minimum at 90° compared to that for forward and backscattering. This makes scattering polarimeters to have moderate or low modulation factors as compared to Bragg and photoelectric polarimeters.

Scattering polarimeters, being based on recording of the photons scattered at various azimuthal angles, they consist of scatterers to scatter the incident photons surrounded by absorbers in order to absorb the scattered photons. An important feature of the Compton polarimetry is the extremely low background in comparison with the Rayleigh mode, which is achieved due to the requirement of simultaneous detection of both, the primary Compton scattering event in the scatterer as well as the secondary detection of the scattered photon by the surrounding absorber. Since, the energy transferred to electron in the scattering event is typically a small fraction of the incident photon energy, scattering polarimeters working in Compton mode are unable to work at lower energies. On the other hand, since Rayleigh polarimeters do not require temporal coincidence between scatterer and absorber, these are sensitive to lower energies as well, where the lower energy cut off depends on the turn over of photoelectric and Rayleigh scattering probability.

1.2.2 Photoelectric polarimetry

In photo-absorption of the X-ray photons, the k-shell photo-electrons are preferentially emitted in the direction of polarization of the incident photons, constituting the basic asymmetric azimuthal angle distribution. Cross-section of photoelectric absorption is given by,

$$\frac{d\sigma}{d\Omega} = \frac{r_e^2 Z^5}{137^4}\left(\frac{mc^2}{E}\right)^{7/2}\frac{4\sqrt{2}\sin^2\theta\cos^2\phi}{(1-\beta\cos\theta)^4}, \tag{1.10}$$

where θ is polar angle between direction of incoming photon and ejected k-shell electron and ϕ is azimuthal angle of the ejected electron with respect to the polarization vector. Modulation in the ejected angle distribution is maximum for $\theta = 90^\circ$ (see Eq. 1.10). Since at energies of few keV, the photo-electrons are preferentially emitted at 90° polar angle, modulation amplitude is expected to be higher for photoelectric polarimeters compared to the scattering polarimeters. Furthermore, since at few keV, most of the photons interact via photoelectric absorption, polarimetric efficiency for the photoelectric polarimeters is high at soft X-rays making it intrinsically more sensitive instrument compared to scattering polarimeters at low energies. However, at higher energies, Compton polarimeters are more sensitive due to increase in scattering probability of photons in material. Therefore, these two techniques are sensitive in different energy ranges and thus actually are complimentary to each other.

[11, 53, 54] discuss the method to image the photo-electron track in pixelated semiconductor detectors. In semiconductor materials photo-electron track is very small ($\sim$1μm for 10 keV electron). Imaging these photo-electron tracks require pixels with size much less than the track length. With current solid state detectors having pixels of few μm, it is extremely difficult to image the photo-electron tracks, making these detectors insensitive to polarization measurements. On the other hand, since in gases, photo-electron tracks are typically of the order of few mm, Gas Electron Multiplier (GEM) based gas detectors [55] are expected to be more sensitive to imaging photo-electron track, where the image is either formed by two dimensional read out anode pixels in Gas Pixel Detectors (GPD, [56–58]) or with one dimensional read out strips in Time Projection Chambers (TPC, [59]), where the other dimension is obtained from the drift time of the electrons.

1.2.3 Bragg reflection polarimetry

Bragg crystal polarimeter [60–62] utilizes the polarization dependence of Bragg reflection, where the photons are preferentially reflected perpendicular to the polarization direction. Since, modulation in azimuthal reflection is found to be maximum at reflection angle of 45°, a crystal kept at angle 45° to the incident X-ray radiation, surrounded by a proportional counter in order to absorb the reflected X-rays, constitute a good polarization analyzer. Both the crystal and the detector are rotated about the incident flux direction to obtain count rates as a function azimuthal angle. Such a system provides modulation factor close to unity. However, perfect atomic crystals reflect X-rays with very narrow energy bandwidth extending over a small fraction of an eV, resulting in a very low polarimetric efficiency, making it insensitive to X-ray polarimetry measurements. Ideally imperfect crystals that are mosaic of small crystal domains with random orientations provide higher effective widths (few eVs) and therefore more suitable for Bragg polarimetry. The crystals can be made bent in order to focus the X-rays onto a small detector so that the background is minimized [63]. The Bragg polarimeter onboard OSO-8 used a parabolic mosaic graphite reflector [61] which obtained the most precise polarization measurement of Crab so far.

1.3 Hard X-ray Polarimetry – How and Why : Thesis Overview

The polarimetry techniques discussed above have their relative advantages and disadvantages. Bragg reflection, despite of achieving high modulation factor (close to unity), work only at discrete energies which results in low polarimetric sensitivity. Compton scattering polarimeters have a moderate modulation factor and polarimetric efficiency and are unable to work at lower energies where flux from X-ray sources is high. However, the advantage of Compton polarimeters is that it can work in a broad energy range in hard X-rays. On the other hand, photoelectric polarimeters possess high modulation factor. Since it is sensitive at soft X-rays where the flux from sources is relatively higher, these kind of detectors are expected to provide orders of magnitude improvement in the X-ray polarimetric sensitivity, when particularly used as a focal plane detector for soft X-ray telescopes. Consequently, in the last decade or so, few polarimetric missions were proposed based on the photoelectric polarimeters [64–68]. Gravity and Extreme Magnetism Small Explorer (GEMS), dedicated X-ray polarimetry mission [66], carrying a Time Projection Chamber (TPC) based photoelectric polarimeter [59] was actually selected for launch in 2014 (the mission was, however, eventually cancelled due to programmatic issues).

Though photoelectric polarimeters are expected to provide sensitive polarization measurements, these instruments are effective primarily in soft X-rays where radiation from the source is expected to be less polarized because of the dominance of thermal radiation over its nonthermal counterpart. For measurement of X-ray polarization at energies above 10 keV, it is necessary to employ polarimeters based on Rayleigh / Compton scattering principle, where Compton scattering based polarimeter has reasonable sensitivity compared to Rayleigh polarimeters because of their extremely low background. Consequently, many groups across the globe are now involved in developing Compton polarimeters effective in hard X-ray regime where the expected polarization is above the typical sensitivity level of the instruments [69–73]. These instruments are large area collimated detectors. Such non-focusing detectors, due to much larger detector area, are susceptible to large background which severely limits the polarimetric sensitivity of the instruments. With recent development of hard X-ray optics e.g. NuSTAR [74], Astro-H [75], hard X-ray polarimetry may see manyfold improvement in terms of sensitivity of the polarimeters. Compton polarimeters at the focal plane of hard X-ray telescopes are expected to provide sensitive polarization measurements because of two factors,

- compact focal plane detectors can be designed with an optimized configuration for polarimetry,

- concentration of flux in hard X-rays and narrow FOV of the telescopes reduces the background which significantly improves the sensitivity of the focal plane polarimeters.

On the other hand, as discussed in Sec. 1.1, polarization studies, specifically in hard X-rays, might address a few specific interesting astrophysical problems,

- binary black hole disk-corona geometry, contribution of reflection component and jet in the hard X-rays,
- emission geometry in isolated pulsars and accreting pulsars,
- emission mechanism behind the second peak of the blazars,
- electron acceleration mechanism in solar X-rays,
- GRB prompt emission mechanism.

Motivated by this, here we investigate a possible implementation of a Compton scattering based X-ray polarimeter and estimate its sensitivity when coupled with NuSTAR type of hard X-ray optics. The geometry we have considered is the most optimum geometry for a focal plane Compton polarimeter and thus the estimated sensitivities are the best possible results one can achieve with the assumed collecting area. Having these sensitivity results as a benchmark would be useful for quantitative comparison of sensitivity of any other configuration of a Compton polarimeter e.g. using different scatterer for additional spectroscopic sensitivity. The other objective of the study is to show our readiness level prior to proposing for a future hard X-ray polarimetry mission. In Chapter 2, we discuss the proposed geometrical configuration of the focal plane Compton polarimeter along with the expected polarimetric sensitivity of the instrument using simulation studies. Chapter 3 discusses the characterization of the active scatterer and the surrounding absorbers and final integration of the polarimeter.

With recent improvement in detection technology and growing realization of the scientific value of X-ray polarimetry, X-ray polarimetry will see significant progress in the coming years. Few dedicated polarimetry missions have been proposed worldwide based on both hard X-ray Compton polarimeter (X-Calibur [76], PolariS [77] and TSUBAME [78]) and photoelectric polarimeters in soft X-rays (with IXPE and PRAYXyS for NASA and XIPE for ESA, recently selected for phase A study in 2015). However, in absence of any dedicated X-ray polarimetry mission at present and in near future, it is important to explore the possibility of extracting polarimetric information from existing or upcoming spectroscopic and imaging instruments. There have been many efforts to recover polarimetric information from the existing data obtained by existing detectors like RHESSI, INTEGRAL-IBIS and INTEGRAL-SPI [15–18, 79–85]. Since these detectors are not designed or optimized for polarimetric observations, such results remain inconclusive [86, 87]. Still, these results carry significant insights into the geometry and emission mechanism in the sources and thus help to expand the so far limited field of X-ray polarimetry.

One of such instruments employing large pixelated CZT detector plane is the CZT-Imager (CZTI) onboard Astrosat [88,89]- the first Indian astronomy mission. CZT detectors are considered as workhorse for the hard X-ray astronomy because of its high efficiency and resolution at those energies [90–93]. Astrosat-CZTI is an imaging instrument using a coded mask and consists of a total 1024 cm^2 pixilated CZT detector array for hard X-ray imaging and spectroscopy in the 10 keV to 100 keV range. The detector plane of CZTI is composed of a total 64 CZT detector modules having integrated readout ASIC. Each module is 4 cm × 4 cm in dimension and thickness is 5 mm and is further pixelated in array of 16 × 16 pixels of dimension 2.5 mm × 2.5 mm. Such a configuration is expected to be sensitive to polarization measurements in hard X-rays. We explore the feasibility of polarization measurements based on simultaneous Compton scattering events in the pixels of CZTI detector modules as discussed in Chapter 4 with the help of detailed simulation and experimental studies.

Since CZTI is primarily a spectroscopic instrument sensitive in $20 - 100$ keV, apart from the polarimetry studies, it is important to fully utilize spectroscopic values of CZT detectors by generating accurate response matrix elements. Line profile of CZT for mono-energetic X-ray photons do not exhibit normal Gaussian feature. Instead it shows a long tail at the lower energies of an otherwise Gaussian profile due to insufficient charge collection in the electrodes because of low mobility and lifetime of the charge carriers. Since these are pixelated detectors, charge sharing becomes significant complicating the line profile further. Therefore, it is important to model the mono-energetic line precisely taking into account all these physical processes. In Chapter 5, we describe a numerical model based on charge trapping and charge sharing to predict the line profiles for CZT detector pixels and finally generate a pixel-wise response matrix. It is to be noted that the double pixel Compton scattering events in CZTI detector pixels which is required to extract polarization information might also be helpful in extracting spectroscopic information at energies beyond its primary energy range of spectroscopy. Simultaneous spectroscopic, timing and polarization studies from CZTI will be extremely useful in complete characterization of the X-ray sources.

Chapter 2

Polarimetric Sensitivity of a Focal Plane Hard X-ray Compton Polarimeter

As discussed in Chapter 1, X-ray polarization measurement of cosmic sources provides two unique parameters namely degree and angle of polarization which can probe the emission mechanism and geometry at close vicinity of the compact objects. Specifically, the hard X-ray polarimetry is more rewarding because the sources are expected to be intrinsically highly polarized at higher energies, due to the dominance of non-thermal radiation over the thermal counterpart. However, at energies > 10 keV, sensitivity of the X-ray detectors is limited due to the lack of photons in hard X-rays. Thus hard X-ray polarimetry so far has been a largely unexplored area. With the recent availability of hard X-ray optics (e.g. with NuSTAR, Astro-H missions) which can focus X-rays from 5 keV to 80 keV, sensitivity of X-ray detectors in hard X-ray range is expected to improve significantly. In this context, we explore feasibility of a focal plane hard X-ray polarimeter based on Compton scattering having a thin plastic scatterer surrounded by cylindrical array scintillation detectors. The geometrical configuration of the Compton X-ray polarimeter (CXPOL) is described in Sec. 2.1. We have carried out detailed Geant$-$4 simulation to estimate the modulation factor for 100% polarized beam as well as polarimetric efficiency of this configuration.

We have also validated these results with a semi-analytical approach discussed in Sec. 2.2. Here, we present the results of polarization sensitivities of such focal plane Compton polarimeter coupled with the reflection efficiency of present era hard X-ray optics in Sec. 2.3.

2.1 Proposed Detector Configuration

As discussed in the previous section, it is necessary to maximize both the modulation factor and the detection efficiency in order to maximize the polarimetric sensitivity. These two parameters are influenced by the type and shape of the scattering element used and must either be measured experimentally or must be determined by means of simulations [94]. The scattering element to be used must be made up of lowest possible Z material to obtain high efficiency (because the cross-section of the competing photoelectric interaction is proportional to Z^5) and it must be designed such that the incident photon sees a larger depth while passing through the volume (to have a significant probability for Compton interaction) and the scattered photon sees a smaller depth in the direction perpendicular to the direction of the incident photon (to minimize multiple interactions within the scattering volume itself). A narrow tube scatterer surrounded by a cylindrical array of detectors would satisfy the above criteria but for its small collecting area. Here, we consider a Compton polarimeter based on this configuration as a focal plane detector for hard X-ray optics. For the purpose of present simulations, we assume optics effective area similar to that of NuSTAR optics. The configuration has a low Z thin scatterer (plastic scintillator) surrounded by a cylindrical array of 32 CsI scintillators to record the azimuthal dependence of scattered X-ray photons. The plastic scintillator is used because of its low Z constituents (C and H) so that the photoelectric absorption is relatively low compared to Compton interaction probability. CsI has very high efficiency to photoelectrically absorb the scattered photons. The plastic scatterer is in cylindrical form of radius 5 mm and length 100 mm. Dimension of the absorbers is 5 mm $\times$ 5 mm$\times$ 150 mm each with total 32 elements in cylindrical array. The modelled configuration is shown in Fig. 2.1 and also include, additional housing structures (assumed to be made of thin Al) as would be required for a real detector. This configuration is very close to the ideal Compton polarimeter with very thin active scatterer (to scatter the incident photons) surrounded by a cylindrical detector (to detect scattered photons) and thus expected to have the best possible sensitivity to measure polarization of the incident X-rays. The exact specifications for the configuration are given in Table 2.1.

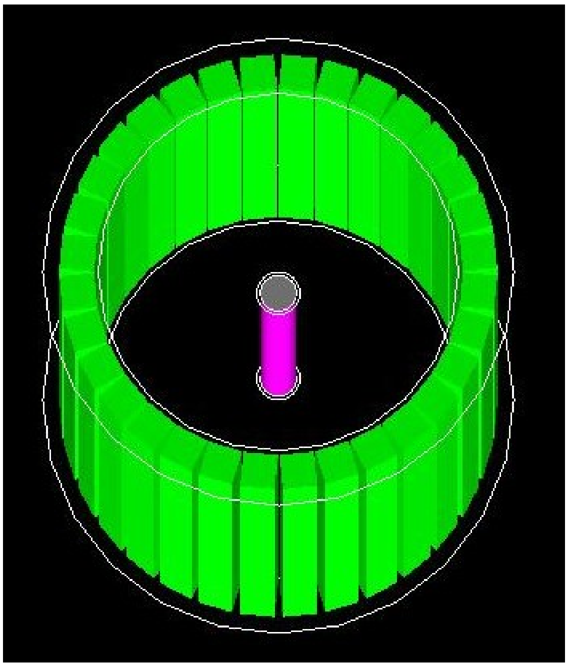

Figure 2.1: View of scattering geometry from the top. The cylindrical bar in pink refers to the plastic scatterer (5 mm diameter and 100 mm length) and the surrounding 32 CsI scintillators (5 mm × 5 mm × 150 mm) are shown in green. The supporting structure is made of aluminium

2.1.1 Comparison with contemporary hard X-ray polarimeters

Many groups worldwide are working for development of Compton hard X-ray polarimeter and some of them are likely to have actual testing / measurement with balloon-borne experiment e.g. GRAPE [72], POLAR [73], PoGOLite [71] etc. Among these, GRAPE and POLAR are open GRB detector and hence cannot

Table 2.1: Scattering geometry dimensions implemented in the application code

Scatterer	
Shape and material	Cylindrical, plastic
Height	100 mm
Diameter	5 mm
Scattering cover	Al with diameter 5 mm and height 5 mm
Absorber	
Shape and material	Cylindrical array of 32 CsI scintillators
Dimension	5 mm×5mm×150 mm
Dead space between scintillators	Al with 0.2 mm width
Distance between center of scatterer and front of scintillator	26.5 mm
Thickness of Al cylinder in between scatterer and absorbers	0.5 mm

be directly comparable. The PoGOLite is a large area, collimated detector. This type of non-focusing detector, due to much larger detector area, is susceptible to large background which severely limits the polarimetric sensitivity and hence it is not expected to match sensitivity of a small sized detector at the focal plane of focussing optics proposed here. There are few other polarimetric mission proposals based on hard X-ray focal plane Compton polarimeters like X-Calibur [76,95], PolariS [77] etc. Among these, our polarimetric configuration closely resembles with the scattering geometry used in X-Calibur [76], which is under active consideration for NASA's next small satellite mission PolSTAR. It consists of a thin scintillator rod surrounded by 2.5 mm × 2.5 mm pixelated CZT detectors from four sides. Thus, the only difference between the two configurations is that the surrounding detector is square rather than cylindrical as proposed here. However, the square surrounding detector has inherent preferred plane for the azimuthal distribution and thus is likely to introduce artificial modulation when the polarization direction of the incident X-rays has a particular alignment with respect to the detector. Further, this would typically result in different modulation factors for the cases when incident polarization plane is parallel to the detector plane or is at 45°. This limitation can be overcome by rotating the polarimeter with respect to the optical axis, however, this requirement of rotation leads to additional complication in the realization of the instrument. On the other hand, the cylindrical detector proposed here can avoid this additional requirement. Also due to the intrinsic symmetry, it is expected to have better and stable modulation factor without any preference to polarization direction of incident X-rays. The pixelated CZT detectors proposed for X-Calibur will have two-dimensional position sensitivity, however, position sensitivity along the length of the plastic scatterer cannot be used to determine the polar scattering angle because exact interaction position in the plastic scatterer cannot be determined. Thus two dimensional position sensitivity of CZT detector only adds additional complexity in electronics in terms of much larger number of readout pixels which can be avoided by simple cylindrical array of scintillators as proposed here. Therefore, we think that the proposed configuration is better alternative in terms of feasibility. However, it is to be noted that the 2 mm thick CZT detectors in X-Calibur would provide better energy resolution compared to any inorganic scintillator. Therefore, X-Calibur is expected to provide comparatively better spectroscopic sensitivity provided the interaction position in the plastic scatterer is known.

2.1.2 Simulation and data analysis

We use Geant−4 toolkit [96] to estimate the modulation factor for 100% polarized beam and efficiency of the instrument. Since we are mainly concerned with interaction of polarized X-ray photons up to energy of ∼100 keV, we employ the low-energy electromagnetic process. Specifically, we use *G4LowEnPolarizedPhotoElectric*, *G4LowEnPolarizedRayleigh*, *G4LowEnPolarizedCompton*, *G4LowEnBremss* and *G4LowEnIonization*.

For each of the energies, we carry out simulation for 1 million photons incident on the scatterer and store the output for each photon detected in the CsI scintillators. A valid event should be defined as one Compton scattering in scatterer and photoabsorption of that scattered photon in one of the absorbers. However in real life there is no way to recognize events involving multiple scattering in scatterer and events where photons suffer scattering in Al cylinder before being absorbed in an absorber. Therefore, only those events which satisfy the energy cuts in plastic and absorber and simultaneity between them have been declared valid and analysed further. Since it is a focal plane instrument, the photons are made to be incident within a very small perpendicular area of radius 2 mm in the scatterer. The output of each simulation run is stored in the form of event list. It should be noted that, though the event list has much more information, for further analysis, which is carried out separately using IDL, we consider only the information which would be available in the real detector such as deposited energy and CsI crystal number. Each event line contains the location of interaction in the plastic scatterer and the surrounding CsI scintillators. There are both Compton and Rayleigh scattering events (at lower energies) in the scatterer. We have to ignore the Rayleigh events and consider only the Compton events. The exact location of photon interaction in each scintillator is not possible. In the current design, there are 32 CsI scintillators surrounding the plastic scintillator; thus 32 bins for the azimuthal scattering angle. At each energy, simulation was done for 1 million photons. Sensitivity of instrument increases with the decrease in energy threshold in scatterer. We assumed energy thresholds of 1 keV and 2 keV for calculations. With this assumption first the azimuthal scattering angle is estimated for every valid event. The azimuthal angle distribution is then fitted with a $\cos^2\phi$ function,

$$C(\phi) = A\cos^2(\phi - \phi_0) + B, \tag{2.1}$$

where A, B, and ϕ_0 (angle of polarization) are the fitting parameters. Amplitude of modulation in the azimuthal angle distribution is given by modulation factor,

$$\mu = \frac{A}{A + 2B}. \tag{2.2}$$

Fig. 2.2 shows one of such modulation curves obtained for 30 keV incident photons. This particular plot is for 1 keV energy threshold. Efficiency at each energy is calculated by summing over all the valid Compton events and then dividing it

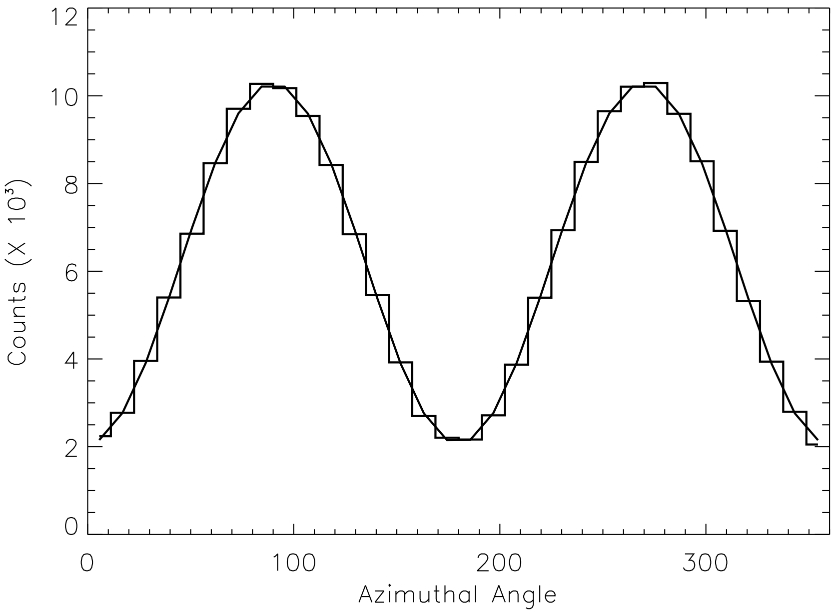

Figure 2.2: Azimuthal angle distribution of the scattered photons obtained from simulation of 30 keV incident photons

by total incident photons which in our case is 1 million. Estimated modulation factor, efficiency and figure of merit of the polarimeter have been shown in Fig. 2.4 as discrete points. Black and red are used to denote 1 keV and 2 keV threshold respectively.Modulation factor is low at lower energies; since the photons scatter at angles greater than 90°. As energy increases, value of modulation factor increases as now more and more photons are scattered at 90° and reaches maximum. The curve then almost flattens at higher energies. Efficiency of the polarimeter increases with the energy as expected. Figure of merit is defined as modulation factor multiplied by square root of the efficiency and is inversely proportional to the minimum detectable polarization if we neglect the source characteristics, time of observation etc.

2.2 Semi-analytic Calculation of Modulation Factor and Efficiency

Here we present a semi-analytical treatment to evaluate modulation factors and efficiencies at different energies for the scattering geometry to compare the results with the simulation results to see whether both the results are consistent or not. Advantage of this semi-analytic formulation is that it can be used for quick checking of some geometric variation of the configuration such as length of scatterer, diameter of the surrounding detector, length of the surrounding detector without running full simulation. Thus, multiple simulation runs can be avoided for minor changes of the geometrical configurations.

We have divided the scatterer into large number of segments (S). Idea is to calculate C$_{max}$ and C$_{min}$ in each segment starting from top to bottom and ultimately add them individually to calculate modulation factor. We also considered the transmission probability of the photons from one segment to another in the scatterer which is $\mathrm{e}^{-\mu_t \rho \frac{10}{S}}$. First step is to calculate the total number of photons scattered at polar angle θ by the scatterer in each segment for azimuthal angle $\phi = \frac{\pi}{2}$ and $\phi = 0$ separately,

$$C_{max}\left(i,\theta\right) = Ne^{-\mu_t \rho i \dfrac{10}{S}} \left(\frac{\mu_c}{\mu_t}\right)\left(1 - e^{-\mu_t \rho \dfrac{10}{s}}\right)\left(\frac{\left(\dfrac{d\sigma}{d\Omega}\right)_{\phi=\frac{\pi}{2}} \sin\theta d\theta d\phi}{\sigma_t}\right), \quad (2.3)$$

$$C_{min}\left(i,\theta\right) = Ne^{-\mu_t \rho i \dfrac{10}{S}} \left(\frac{\mu_c}{\mu_t}\right)\left(1 - e^{-\mu_t \rho \dfrac{10}{s}}\right)\left(\frac{\left(\dfrac{d\sigma}{d\Omega}\right)_{\phi=0} \sin\theta d\theta d\phi}{\sigma_t}\right), \quad (2.4)$$

where, i signifies each slice and goes from 0 to (S-1), N is number of incident photons, μ_c is the mass absorption coefficient of Compton scattering for plastic in $cm^2/gm.$ unit at energy E, μ_t is the mass absorption coefficient of total interaction for plastic in $cm^2/gm.$ unit at energy E, ρ is the density of plastic in gm/cm^3 unit. Thickness of each segment is $\dfrac{10}{S}$. σ_t is the total Compton scattering cross-section i.e.

$$\sigma_t = \int_0^\pi \frac{r_0^2}{2} \left(\frac{E'}{E_0}\right)^2 \left(\frac{E'}{E_0} + \frac{E_0}{E'} - \sin^2\theta\right) 2\pi \sin\theta \; d\theta. \tag{2.5}$$

The ratio of cross-sections (Eq. 1.8 and Eq. 2.5) gives the fraction of photons scattered at angle θ. Since only those photons which are scattered at a particular range of angles will be absorbed by the CsI scintillators, so the next step is to integrate the equation over the angular range covered by the surrounding scintillators for each segment. This angle range (θ_{min} to θ_{max}) depends on the geometry and energy deposition during scattering in plastic scintillator and the segment from where scattering takes place. Here we assume 100% detection efficiency of the CsI detectors. For each slice, θ_{min} and θ_{max} are calculated properly (see Fig. 2.3). From the scattering geometry, we obtain

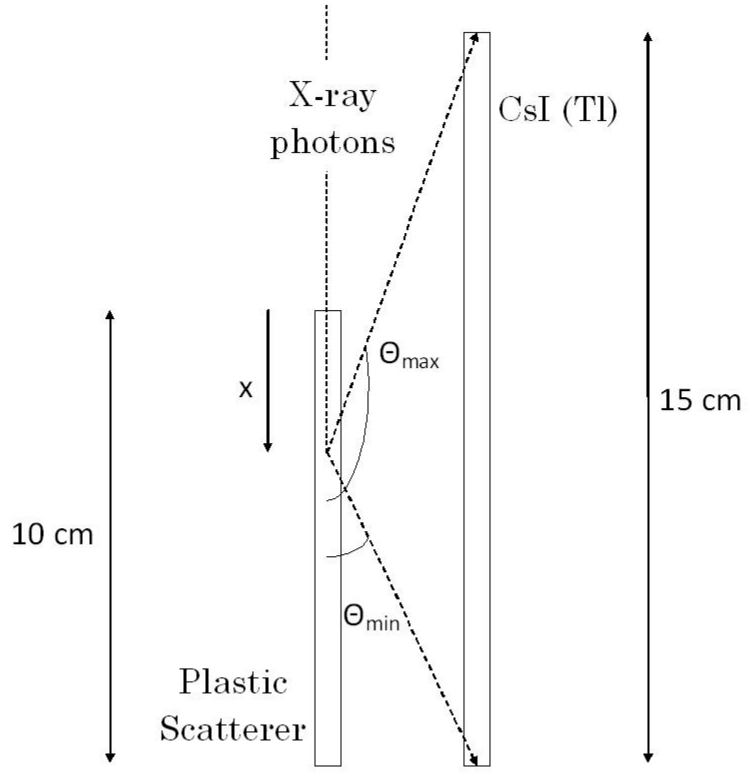

Figure 2.3: Schematic view of the scattering geometry. θ_{min} and θ_{max} are respectively the minimum and maximum scattering angle

$$\theta_{max} = \sin^{-1} \frac{x+5}{\sqrt{(x+5)^2 + (2.65+0.5)^2}}, \tag{2.6}$$

$$\theta_{min} = \sin^{-1} \frac{2.65 + 0.5}{\sqrt{(10 - x)^2 + (2.65 + 0.5)^2}}. \tag{2.7}$$

For high energy photons the scattering takes place in the forward direction. The minimum scattering angle depends on the threshold energy in the scatterer and is equal to $\cos^{-1}\left(1 - \frac{E_{thres} m_e c^2}{E\left(E - E_{thres}\right)}\right)$, where E_{thres} is the energy threshold in scatterer and E is energy of the incident photons. To make sure that only those photons scattered towards the CsI scintillators are counted, we have to take either sine or cosine function whichever is maximum as lower limit of integration. In the last step, the contributions from all the segments are summed over and we get

$$C_{max} = \sum_{i=0}^{i=S-1} N e^{-\mu_t \rho i \frac{10}{S}} \left(\frac{\mu_c}{\mu_t}\right) \left(1 - e^{-\mu_t \rho \frac{10}{s}}\right) \left(\frac{\int_{\theta_{min}}^{\theta_{max}} \left(\frac{d\sigma}{d\Omega}\right)_{\phi=\frac{\pi}{2}} \sin\theta \; d\theta \, d\phi}{\sigma_t}\right), \tag{2.8}$$

$$C_{min} = \sum_{i=0}^{i=S-1} N e^{-\mu_t \rho i \frac{10}{S}} \left(\frac{\mu_c}{\mu_t}\right) \left(1 - e^{-\mu_t \rho \frac{10}{s}}\right) \left(\frac{\int_{\theta_{min}}^{\theta_{max}} \left(\frac{d\sigma}{d\Omega}\right)_{\phi=0} \sin\theta \; d\theta \, d\phi}{\sigma_t}\right). \tag{2.9}$$

Modulation factor can be obtained from Eq. 2.8 and Eq. 2.9

$$\mu\left(E\right) = \frac{C_{max} - C_{min}}{C_{max} + C_{min}}. \tag{2.10}$$

Efficiency is calculated in a similar way. Assuming 100% efficiency of the CsI detectors in the energy range of operation, we estimate the polarimetric efficiency by calculating the total number of photons scattered by all the segments in the plastic scatterer towards the surrounding CsI scintillators. Using the same approach, the efficiency is determined as

$$\epsilon = \sum_{i=0}^{i=S-1} e^{-\mu_t \rho i \frac{10}{S}} \left(\frac{\mu_c}{\mu_t}\right) \left(1 - e^{-\mu_t \rho \frac{10}{s}}\right) \left(\frac{\int_{\theta_{min}}^{\theta_{max}} \left(\frac{d\sigma}{d\Omega}\right) 2\pi \sin\theta \; d\theta}{\sigma_t}\right). \tag{2.11}$$

To take care of the dead spaces in between the CsI detectors a factor of $1-\frac{32\times0.02}{2\pi\times2.65}$ is multiplied with the above equation.

Results of these calculations are shown in Fig. 2.4 as continuous lines. It can be seen that the semi-analytical results for modulation factor agree well with the simulation results for most of the energy range, though there is slight discrepancy at lower energies. In case of efficiency, the simulated efficiency is slightly lower than the calculated one. However, it should be noted that in this analytic calculation, we have ignored some of the second order effects such as the multiscattering in surrounding scintillators and the scatterer itself, escape of photons from the CsI detectors, the absorption of scattered photons within the Al in between the scatterer and surrounding scintillators. These factors are not significant for modulation factor, particularly when the number of detected photons is very large. Modulation factor will depend on the angle range mainly, that is why we see good agreement in the results of analytical and simulation results. However these factors are critical for efficiency calculation and as a result

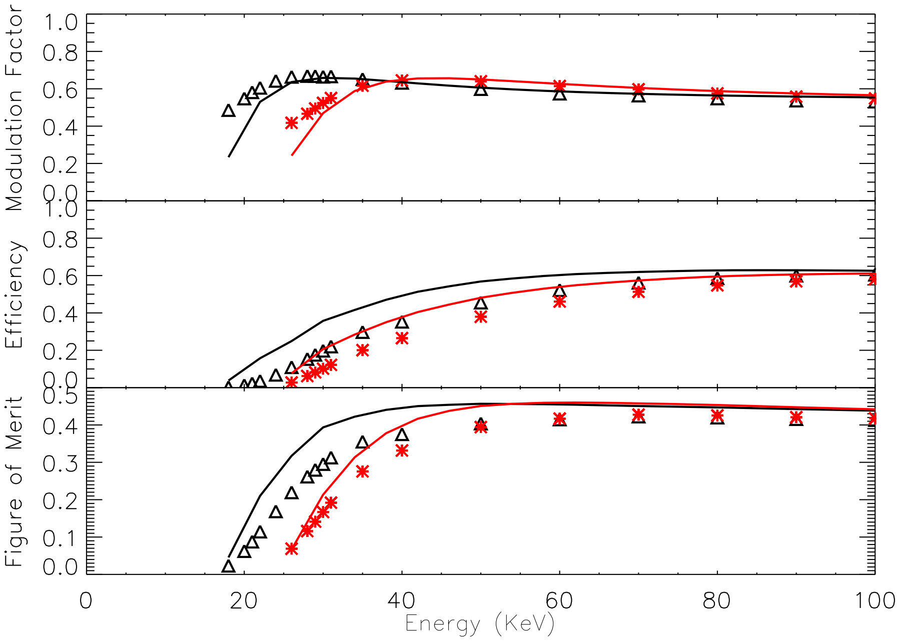

Figure 2.4: Modulation factor, polarimeter efficiency and figure of merit as a function of energy. Black triangles and black solid line represent simulation and analytical results respectively for 1 keV threshold. Red asterisks and red solid line represent the simulation and analytical results respectively for 2 keV threshold

analytical model gives slightly higher values of efficiency.

2.3 Polarimetric Sensitivity of CXPOL

Sensitivity of polarimeter (see Eq. 1.5 in Chaper 1) depends on energy integrated modulation factor in the energy range of operation for 100% polarized beam, exposure time, background and rate at which source photons are detected by the instrument which in turn depends on efficiency of polarimeter, source intensity and effective area of the mirror used to focus the X-rays. For MDP calculation we have used the NuSTAR optics effective area [97]. NuSTAR can focus photons from 5 keV to 80 keV. If the threshold is assumed to be 2 keV, polarimeter starts working from 26 keV whereas for 1 keV threshold lower cut off is 18 keV. First the average modulation factor is estimated in the working energy range ($18 - 80$ keV and $26 - 80$ keV) which for 1 keV and 2 keV threshold is around 60.5% and 60% respectively. This proves the excellent polarimetric performance of this focal plane polarimeter. Source count rate is calculated as follows

$$R_{src} = \int_{E_1}^{E_2} A_{eff}\left(E\right) I\left(E\right) \epsilon\left(E\right)\ dE, \tag{2.12}$$

where $A_{eff}(E)$ is the effective area of NuSTAR, $I(E)$ is the source intensity for Crab like spectrum, $\epsilon(E)$ is the polarimeter efficiency at energy E. Value of E_1 depends on threshold in scatterer and E_2 is 80 keV as we are considering NuSTAR optics. We have considered 100 ks and 1 Ms exposure for sensitivity estimation. Background calculation is discussed in detail below.

2.3.1 Spurious events calculation

Background for a focal plane Compton polarimeter is generally very small. The only source of spurious events in Compton polarimeters is the chance coincidence between the random background events in the scatterer and in the absorbers within the coincidence time window. Using Poissons statistics in the coincidence window one obtains the rate of spurious events due to the chance coincidence,

$$N_{sp} = \left(1 - e^{-N_{scatterer}T}\right) N_{absorber}, \tag{2.13}$$

where $N_{scatterer}$ $(= N_1 + N_2)$ is the sum of rate of random background events in the scatterer (N_1) and the cosmic X-ray background rate (N_2) in scatterer. N$_{absorber}$ is the rate of random instrumental background events in the absorbers. Rate at which the cosmic X-ray photons are detected in the scatterer has been calculated using cosmic X-ray background spectrum [98]. Since the FOV of focal plane detector is very small, this value is very small. The cosmic X-ray photons coming from the sky within the detector field of view may be scattered by the scatterer and absorbed by the absorbers. This may also lead to spurious Compton events (N_{sky}). Therefore the rate of total spurious events in the polarimeter can be written as

$$N_{sp} = \left(1 - e^{-N_{scatterer}T}\right) N_{absorber} + N_{sky}. \tag{2.14}$$

Since the value of N_{sky} is very small due to narrow FOV, the random particle events will dominate the background. Since the actual instrumental background generally depend on the variety of factors such as spacecraft, orbit, time etc. which cannot be estimated at present, we assumed a range of instrumental background rate from 0.5 $cnt\ cc^{-1}s^{-1}$ as a typical condition and 5 $cnt\ cc^{-1}s^{-1}$ as extreme condition. We calculated the spurious events rates corresponding to these two limiting instrumental background rates keeping the time coincidence window of 10 μs , which is then used for calculating MDP values.

2.4 Results and Discussions

With the method discussed in previous section, we estimated MDP for different Crab intensities which are shown in Fig. 2.5. We see for 100 mCrab source the MDP is 0.9% with 3σ confidence level with 1 Ms of exposure time (black solid lines, asterisks), which qualifies this focal plane polarimeter as a sensitive instrument. However for 100 ks exposure, the sensitivity decreases to 3%. We have also analysed the simulation data by selecting only valid/ideal Compton events and find that the results are almost identical, which suggests that this configuration

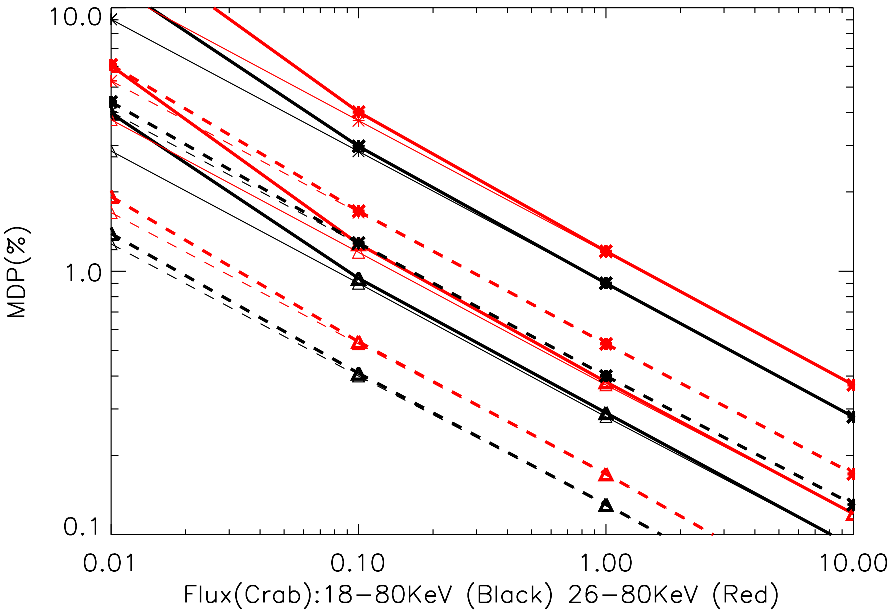

Figure 2.5: MDP as a function of source intensity in Crab unit. Solid lines represent results obtained assuming single NuSTAR mirror area. Dashed lines refer to 5 times larger NuSTAR area. 1 Ms and 100 ks exposure times are denoted by triangles and asterisks respectively. The backgrounds considered here are 0.5 $cnt\ cc^{-1}s^{-1}$ (thin lines) and 5 $cnt\ cc^{-1}s^{-1}$ (thick lines)

is very close to the ideal Compton polarimeter configuration. MDP values have been calculated for random instrumental background rate of 0.5 $cnt\ cc^{-1}s^{-1}$ (thin lines) and in extreme condition of 5 $cnt\ cc^{-1}s^{-1}$ (thick lines); however there is not much change in MDP with background beyond 100 mCrab. In Fig. 2.5, we have shown that sensitivity can be increased significantly using next generation of hard X-ray focusing optics with collecting area 5 times larger than that of NuSTAR area (dashed lines). With this configuration, MDP for 100 mCrab source decreases to 0.4% for 1 Ms exposure and 1.3% for 100 ks exposure. Fig. 2.5 clearly suggests that sensitivity of the polarimeter is improved for 1 keV energy threshold in scatterer instead of 2 keV. Here, it is to be noted that reflection off the hard X-ray mirror may introduce small artificial modulation in the azimuthal angle distribution due to the dependence of mirror reflectance on the polarization plane. Recent studies [99] suggest that change in polarization because of the hard X-ray mirrors is around ~1%, therefore limiting the sensitivity of the polarimeters at the focal plane of such hard X-ray telescopes to ∼1%. Another important point for this kind of focal plane polarimetric configuration is the strict requirement of co-alignment of the mirror optic axis and the scatterer axis. Sight deviation of the focal position from the scatterer axis, either permanent or temporal due to jitter, may introduce artificial modulation in the azimuthal angle distribution. These factors are important in optimizing the scatterer diameter for the polarimeter. The depth of the focus along the scatterer axis should also be optimized such that loss of photons due to leakage through the scatterer is minimized. It depends on the convergence of radiation from the mirror and the length of the scatterer which can be inferred by simulating the actual optics system along with the CXPOL configuration.

In Fig. 2.6, we have shown that energy dependent polarization measurement is possible with this focal plane polarimeter which is very useful to study the X-ray objects. Assuming energy resolution about 10 keV FWHM, estimated MDP

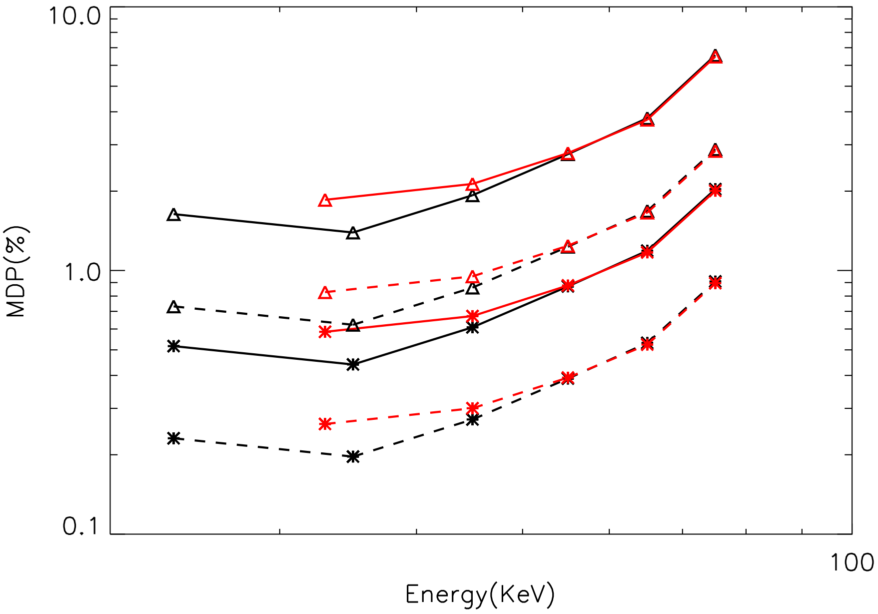

Figure 2.6: MDP of the Compton Polarimeter as a function of energy. Triangle and asterisks denote 100 mCrab and 1 Crab source intensity respectively. Red and black stand for 2 keV and 1 keV threshold respectively in the plastic scatterer. Dashed lines represent 5 times larger NuSTAR area. The exposure time considered here is 1 Ms and background is 0.5 $cnt\ cc^{-1}s^{-1}$

for 100 mCrab and 1 Crab have been shown in the figure (triangle and asterisks) for 1 Ms exposure. The dashed lines correspond to the 5 times larger NuSTAR area. The slight difference in sensitivity at lower energies for 1 keV (black) and 2 keV (red) threshold is due to higher modulation factor and efficiency for 1 keV threshold compared to 2 keV threshold. A particular energy bin corresponds to almost same amount of flux. As energy increases, modulation factor for 2 keV threshold exceeds that for 1 keV threshold, however due to low efficiency the MDP values remain almost same.

2.5 Summary

In this chapter, we described an optimized Compton polarimeter configuration at the focal plane of NuSTAR kind of hard X-ray optics. Geant−4 simulations suggest that we can achieve 1% MDP for 100 mCrab source with this instrument for 1 Ms exposure. To measure polarization of the celestial X-ray sources we need this kind of sensitivity. With the next generation of hard X-ray focussing optics, we can achieve even better sensitivity with this kind of focal plane polarimeter. As simulation results suggests, energy threshold in plastic scatterer is the key parameter which will decide the sensitivity of the instrument. Therefore, it is important to measure the threshold in plastic first and lower it down as much as possible before integrating the whole system to investigate its overall performance. The results of the prototype of the instrument are reported in the next chapter.

Chapter 3

Development of the Focal Plane Compton Polarimeter

In Chapter 2, we described detailed simulation study of the expected sensitivity of our planned configuration of the focal plane Compton polarimeter, when coupled to the NuSTAR type hard X-ray optics, assuming two different values of low energy thresholds - 2 keV and 1 keV, for the active plastic scatterer. In order to have better understanding of the behavior of the scatterer for very low energy deposition, we carried out a controlled Compton scattering experiment with the actual plastic scatterer. In this chapter, we describe the experiment in detail and present the experimental results. The photons scattered by plastic scatterer arecollected by a cylindrical array of CsI(Tl) scintillators which are read by Si Photomultiplier (SiPM). Use of the new generation SiPMs ensures the compactness of the instrument which is essential for the design of focal plane detectors. After complete characterization of the plastic scatterer, we characterize the CsI(Tl)-SiPM absorbers in Sec. 3.5. In Sec. 3.6, we finally present the experimental results from the fully assembled configuration of the Compton polarimeter.

3.1 Characterization of the Plastic Scatterer

Focal plane Compton polarimeter uses long thin low-Z scatterer, typically plastic scintillator, to maximize the Compton scattering probability. While it is possible to conceive Compton polarimeter configurations with Silicon (active detector with second lowest atomic number), polarimetric sensitivity of such configuration is significantly less than those using plastic scintillator as scatterer [100]. Other organic scintillators having higher density but same effective Z as plastic scintillator may be better suited for active scatterer. However, these need careful evaluation for comparative operational advantage. Therefore, plastic scintillators are the usual choice for dedicated hard X-ray polarimeters, when polarimetric information is the main concern. The central scatterer is surrounded by high Z absorbers to measure the azimuthal distribution of the scattered photons. In all such configurations of Compton polarimeters, the lowest possible energy for which polarization can be measured depends on the lower energy threshold of the active scatterer. The lower energy threshold for polarization measurement is a very important parameter for any Compton polarimeter because it determines the lower energy limit for the polarimeter and affects overall sensitivity of the polarimeter too. Since the number of source photons increases significantly as energy threshold decreases, improvement of lower energy threshold by even a few keV can greatly improve the sensitivity of the polarimeter (see Fig. 3.1).

Sensitivity of the polarimeter is generally given in terms of the Minimum Detectable Polarization (MDP) at the confidence level of 99% [101], and is defined as

$$MDP_{99\%} = \frac{4.29}{R_{src}\,\mu_{100}}\sqrt{\frac{R_{src}\,+\,R_{bkg}}{T}}, \tag{3.1}$$

where, μ_{100} is the modulation factor for 100% polarized beam. R_{src} and R_{bkg} are the source and background count rate respectively. T is the exposure time. The modulation factor, μ_{100}, depends on the geometry of Compton polarimeter and is typically in the range of 20% to 50%. The exposure time for the present generation polarimetric observations is of the order of 100 ks to 1 Ms. The dependence of MDP on the lower energy detection limit of the active scatterer comes form the source count rate, R_{src}; lower the threshold, higher the value of R_{src} and better is

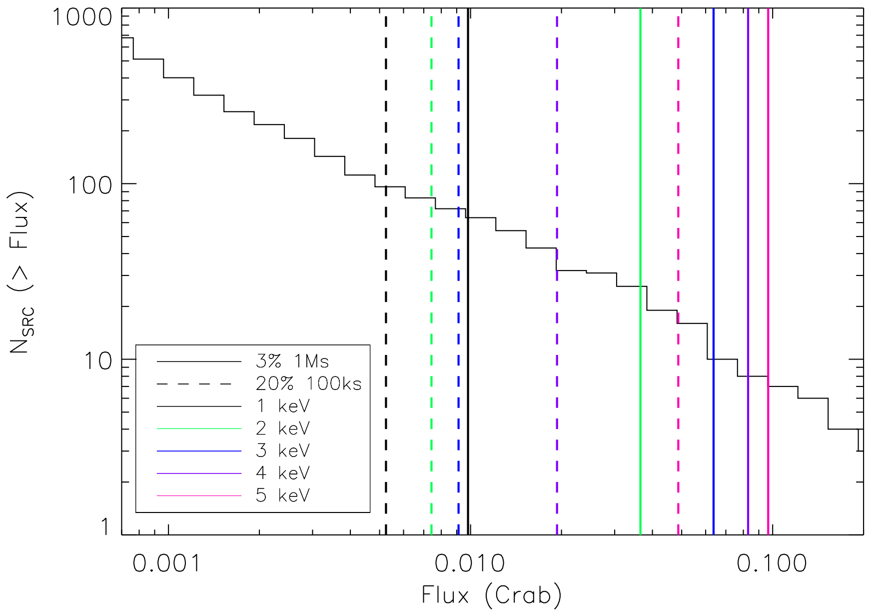

Figure 3.1: LogN-LogS plot obtained from Swift BAT 70 month hard X-ray survey. The vertical solid and dashed lines represent the source intinseties corresponding to the MDP of 3% with 1 Ms exposure and MDP of 20% with 100 ks exposure respectively. Different colors represent different threshold energies in the active scatterer

the sensitivity. The astrophysical significance of this dependence can be seen from Fig. 3.1, which shows the number of X-ray sources accessible for the polarimetric investigation for different lower energy thresholds of the active scatterer. This figure shows the $logN - logS$ plot based on the Swift-BAT hard X-ray catalog resulting from 70 months observations. There are total 1171 hard X-ray sources in the catalog, observed in 14 keV to 195 keV energy band. This $logN - logS$ plot is over plotted by the source intensities corresponding to the specified values of MDP, exposure time and the lower energy threshold of the scatterer. These source intensities are computed using Eq. 3.1 for different scatterer thresholds (1 keV, 2 keV, 3 keV, 4 keV and 5 keV) assuming Crab like spectra and convolving the source spectra with Nustar kind of hard X-ray mirror effective area. The modulation factor, μ_{100} used here is obtained from our Geant$-$4 simulations reported in chapter 2. The vertical solid and dashed lines represent 3% MDP in 1 Ms and 20% MDP in 100 ks respectively, whereas different colors represent different scatterer thresholds. It can be seen that for lower threshold, number of observable sources accessible for investigation of polarization greater than a particular MDP, is significantly larger than that for higher threshold. That is why, it is important to know the realistic threshold energy of the primary scatterer.

However, the plastic scatterer is not expected to have a sharp energy threshold because X-ray detection in the plastic scintillator is essentially a statistical process and depends on various factors such as location of the interaction, light collection efficiency etc. Therefore, such a detector is likely to have decreasing probability of low energy depositions in the plastic being recorded. Thus for any Compton polarimeter design, it is very important to have accurate understanding of the behavior of the active scatterer for low energy depositions so as to have more realistic estimate of the polarimetric sensitivity.

In this context, we carried out a Compton scattering experiment which directly probes the behavior of the active scatterer for very low energy depositions. The experiment uses the same configuration of the plastic scintillator planed to be used in the Compton polarimeter. Here we detect the Compton scattered X-rays using an independent detector at different scattering angles for an X-ray beam of known energy incident on the plastic scintillator along its axis. Recently, [102] have reported a similar study of the active scatterer based on the same concept. They concluded that the polarization measurements down to $\sim$20 keV are possible by using plastic scintillator as an active scatterer. However, their experimental setup was limited to a fixed geometry of the source, the scatterer and the absorber. We carried out a similar experiment, but with an improved experimental setup which allowed control over the scattering angle and thus the energy deposited in the scatterer, to investigate the response of the plastic scintillator at various deposited energies.

3.2 Description of the Experiment

3.2.1 Experiment setup

Typically, the lower energy threshold for an X-ray detector is measured either by directly measuring low energy X-rays from a suitable mono-energetic X-ray source or by extrapolating the peak positions to energy relation to the noise floor of the detector. However, these methods are not suitable for our present objective because of two reasons - 1. energy resolution of the plastic scintillator is very poor and hence extrapolation method can not provide accurate threshold, and 2. the encapsulation required for the scintillator prevents transmission of the X-rays with energies less than ∼5 keV. For typical detector applications in such conditions, the transmission of the entrance window would determine the lower energy threshold. In case of the plastic scintillator as scatterer for a Compton polarimeter, the energy range of interest for incident X-rays is $>$ 10 keV and hence very thin entrance window of Beryllium, as is typically used to achieve high window transmission, is not necessary. Here the energy range of interest for detection of the deposited energy is ∼1 keV to 5 keV. Therefore we employ the same principle of Compton scattering to investigate the response of plastic detector to small energy deposition.

If a photon of energy E is Compton scattered at an angle θ, the energy deposited (recoil energy of electron) is given by,

$$\Delta E = E - \frac{E}{1 + \frac{E}{m_e c^2}(1 - \cos\theta)}, \tag{3.2}$$

where, $m_e c^2$ is the electron rest mass. Fig. 3.2 shows variation of the deposited energy in scatterer as a function of scattering angle for different energies of the incident photon. It can be seen that the incident photons with energies of ∼20 keV to 60 keV and scattered between 30° - 150° angles, provide opportunity to investigate the scatterer threshold in ∼0.5 keV to 10 keV.

In the actual experiment, we detect the Compton scattered X-ray photons with energies of 59.5 keV and 22.2 keV (from radioactive sources ^{241}Am and ^{109}Cd respectively), in the scattering angle range of 25° - 140°, simultaneously with the trigger signal from the plastic scatterer. Fig. 3.3 shows the experimental setup, which uses the plastic scatterer identical to the one which will be used in our planned configuration of the focal plane Compton polarimeter. The scatterer is of 5 mm diameter and 100 mm length and is surrounded by 1 mm thick Aluminum cylinder and a 0.5 mm thick Aluminum entrance window. It was obtained from Saint-Gobain as an integrated module containing plastic scintilla-

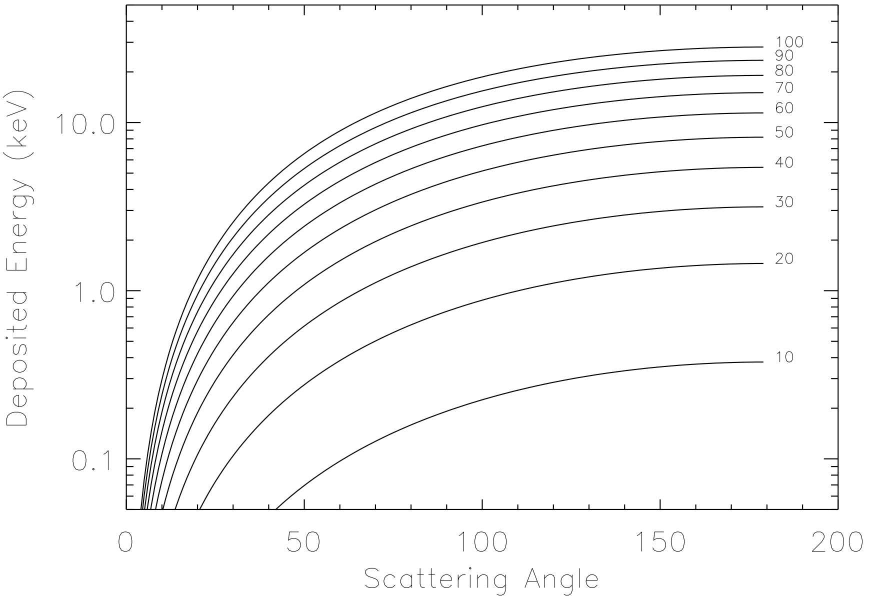

Figure 3.2: Deposited energy in Compton scattering as a function of scattering angle and photon energy. Each line corresponds to a particular incident photon energy in keV as mentioned in the plot

tor (BC404) coupled to a photo-multiplier tube (PMT - Hamamatsu R6095 with bialkali photocathode with maximum quantum efficiency of $\sim$ 25% at 420 nm). In the polarimeter configuration, the scatterer will be surrounded by a cylindrical array of CsI(Tl) scintillators, each of dimension 5 mm × 5 mm × 150 mm, to measure the azimuthal distribution of the scattered photons. In the present experiment, we are only interested in the polar scattering angle, and hence we use a small CdTe detector placed on a rotating arm. We used the standard X-123CdTe system from Amptek [103], which is kept on the rotating arm. The X-123CdTe is a compact integrated system consisting of 1 mm thick CdTe (9 mm^2 active area), pre-amplifier, digital pulse processor, MCA, and power supply. It also has a 'gated' mode of operation, in which it accepts an event only if the gate is kept 'ON' by applying a logic pulse. We use this mode to enforce the simultaneity between the plastic scatterer and the CdTe detector. As shown in Fig. 3.3, the source photons from radioactive source placed in front of the scatterer, are scattered by plastic and the scattered photons are detected by the CdTe detector kept at known angle. Positions of these two detectors can be adjusted in order to

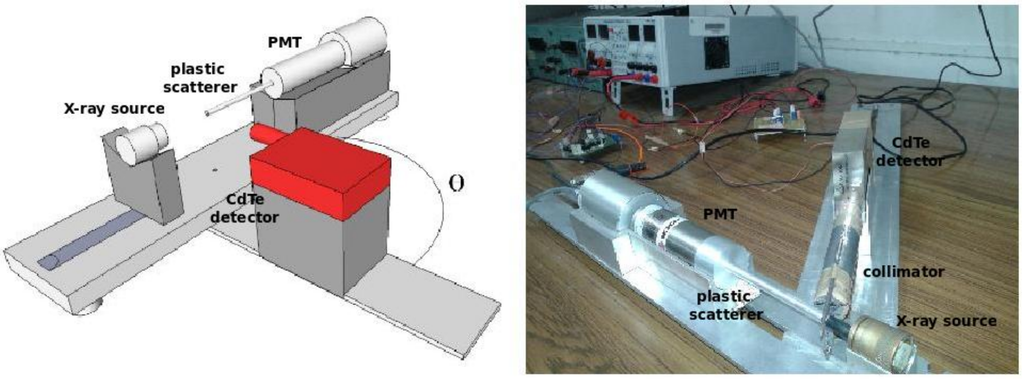

Figure 3.3: Left: Schematic view of our experiment setup. Scattered photons from plastic are absorbed by CdTe kept at angle θ. Right: actual experiment setup - Axes of plastic scintillator (along with PMT and CSPA), source, and CdTe are kept at the same plane using Al blocks. CdTe is kept on a rotating arm in order to detect photons at different scattering angles

optimize the interaction location. A collimator (70 mm long and 7 mm opening) made of Al is used in front of CdTe window to localize the scattering region. The collimator is wrapped by 1 mm thick lead to avoid contamination by any unwanted events. FOV of the collimator is around 10°, which allows to know the position of the interaction in the plastic scintillator within few mm. It is crucial to maintain the alignment of the axes of source aperture, plastic rod and CdTe collimator to keep them in the same plane and a special care was taken to maintain the alignment at different scattering angles. In order to maximise the scattered counts in CdTe, a region at the top of the plastic was localised.

When an incident photon deposits sufficient amount of energy in the plastic scintillator, either by the photoelectric interaction or Compton scattering, a logic pulse with fixed width of 3 μs is generated by the front-end electronics. The front-end electronics consists of a CSPA followed by a fast shaping amplifier (unipolar type with shaping time constant of 2.6 μs) and a comparator as shown in the block schematic in Fig. 3.4. Sensitivity of the scatterer also depends on the HV bias for the PMT and comparator threshold. The optimum values for HV and comparator threshold were found to be 1 kV and 50 mV respectively during the initial trials and then were fixed for the entire experiment. The logic pulse generated by the front-end electronics is then fed to the input of 'Gate' of the

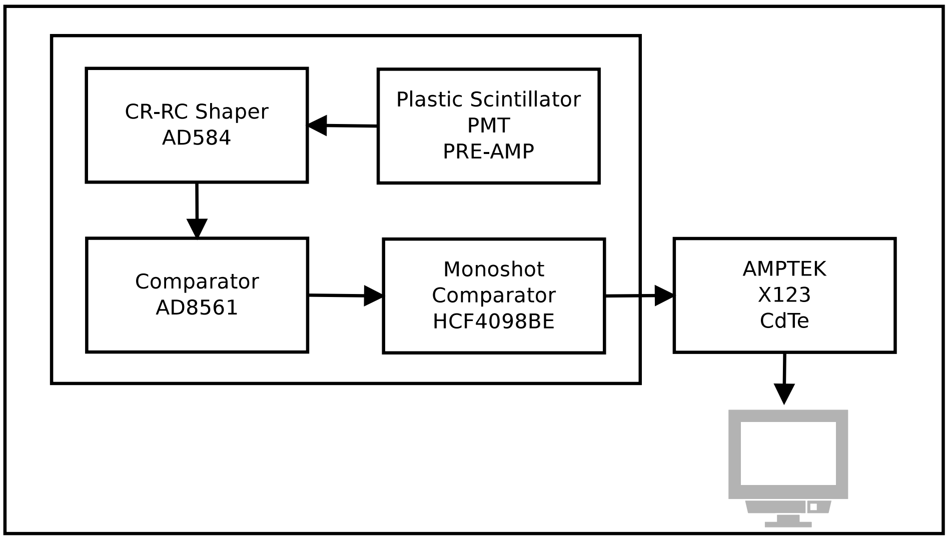

Figure 3.4: Block schematic for the coincidence unit between plastic scintillator and X123CdTe

X123CdTe system and thus it detects the photons only for the duration of 3 μs following a trigger from the plastic scatterer. For each scattering angle, we acquire two sets of spectra from CdTe - first, with the coincidence between CdTe and plastic enforced, which actually gives the Compton scattering events and second, without coincidence (PMT HV off), i.e. plastic behaving as a passive scatterer. With the simultaneity between plastic and CdTe enforced, it is expected that only a very small fraction of all the triggers would have simultaneous detection in the CdTe and hence total experiment duration has to be very large (few hours) but would result in relatively very short acquisition time of few minutes. This has important implication in our semi-analytical modeling as discussed in the following sections.

3.2.2 Results

The spectra acquired from the CdTe detector at three different scattering angles in both the modes i.e. in coincidence with the scatterer and without coincidence, for both 59.5 keV (from ^{241}Am) and 22.2 keV (from ^{109}Cd) incident X-rays are shown in Fig. 3.5. These spectra are normalized with respect to actual acquisition time (time for which CdTe 'Gate' was on during the exposure). In each plot, the solid line represents spectrum in coincidence mode and the dashed line represents spectrum in non-coincidence mode. The backgrounds in both coincidence and non-coincidence mode are negligible compared to the respective source counts. It can be seen that the count rate in the coincidence mode is higher than that in the non-coincidence mode as expected, because in coincidence mode, the CdTe detector accepts an event only for a short duration after each trigger in the plastic scatterer. The energy of the Compton peaks also changes with scattering angle as expected. The detection of Compton peak at 60° from 22.2 keV X-rays clearly shows that the plastic scatterer can detect energy depositions less than 1 keV. Fig. 3.6 shows the observed count rate at all measured angles for both the sources. Total counts for the ^{241}Am are obtained by summing over ±3 FWHM from the peak energy for each spectrum, however for the ^{109}Cd, total counts are obtained by summing over -3 FWHM to +1 FWHM in order to avoid contribution from

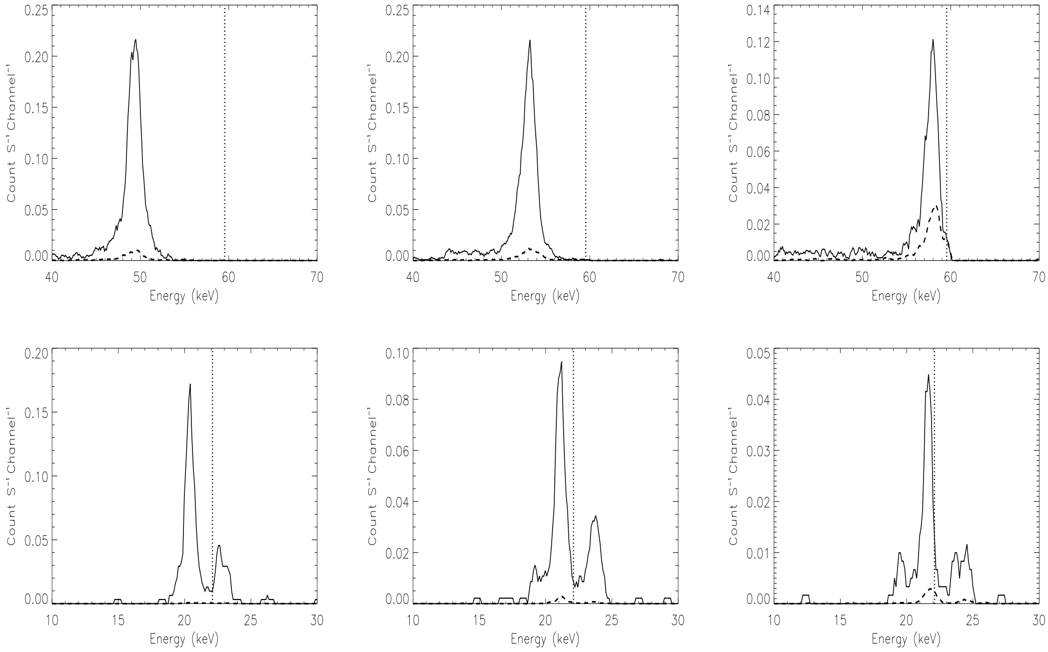

Figure 3.5: Coincidence (solid) and non-coincidence (dashed) spectra observed with the CdTe detector at different scattering angles. Upper panel (left to right) shows spectra for 59.5 keV from ^{241}Am at scattering angles 140°, 90°, 35° respectively. Lower panel (left to right) shows spectra for 22.2 keV of ^{109}Cd at scattering angles 140°, 90°, 60° respectively. Energy of primary incident photons have been represented by the dotted lines

the secondary peak at 25 keV. Again, for each spectrum the count rate is with respect to the actual acquisition time which is related to the exposure time by equation

$$T_{co} = T_{co}^{exp} T_{win} R_{trig}, \tag{3.3}$$

where, T_{co} (∼200 sec for ^{241}Am and ∼100 sec for ^{109}Cd) and T_{co}^{exp} (∼2 hrs for ^{241}Am and ∼7 hrs for ^{109}Cd) are acquisition time and exposure time respectively in coincidence condition, R_{trig} is trigger rate in plastic and T_{win} is the coincidence time window (∼3 μs). The acquisition time is measured by the CdTe detector, which allows to calculate trigger rate for each measurement.

The count rates in coincidence mode, R_{co}, and in non-coincidence mode, R_{nco}, are given by

$$R_{co} = \frac{N_{co}}{T_{co}}, \tag{3.4}$$

$$R_{nco} = \frac{N_{nco}}{T_{nco}}, \tag{3.5}$$

where N_{co} and N_{nco} are the summed counts under these peaks (Compton and Rayleigh) in coincidence and non-coincidence mode respectively for a particular angular position θ of CdTe. T_{nco} (0.5 hours for ^{241}Am and 1.5 hours for ^{109}Cd) is the acquisition time in non-coincidence mode.

Since, $T_{co} \ll T_{nco}$, $R_{co} \gg R_{nco}$ as can be seen in the figure with open circles and filled circles representing coincidence and non-coincidence modes respectively. At lower angles ($< 45°$), there is also a finite probability of the source photons directly entering into the CdTe detector, which leads to increase in count rate in both non-coincidence and coincidence mode due to the chance coincidences. This problem is only present for ^{241}Am source, because in case of ^{109}Cd, the measurements are limited to scattering up to 60°. To correct for the spurious count rate due to direct exposure, we measured number of counts at lower angles for ^{241}Am without having the plastic scintillator in place. This configuration then measures any 'leakage' of photons through the intervening material. However, direct subtraction of these counts from the observed counts for ^{241}Am at the respective lower angles would underestimate the non-coincidence count rate, because the plastic scintillator and the surrounding Aluminum may absorb some of these photons. We estimated this absorption fraction for different angles at energy 59.54 keV based on the geometry of our experiment setup. The observed count rate due to direct exposure (without the plastic scatterer) is then corrected by this absorption fraction and then subtracted from the observed count rate (with the plastic scatterer) to calculate correct count rate due to scattering only.

The error bars shown here combine both statistical and systematic uncertainties. The sources of systematics are misalignment between collimator and plastic scatterer, uncertainty in angle measurement, uncertainty in the center of rotation of CdTe around plastic and the uncertainty in the coincidence time window. The most prominent source of error is the misalignment of plastic and the collimator, for which we have tried to control within the experimental limits. The contributions of each of these sources to overall systematic error is estimated as per following discussion. Error due to misalignment between plastic axis and CdTe collimator axis is obtained by geometrically estimating the intersection area of CdTe field of view with the plastic for a given angle. A misalignment of 1 mm introduces a minimum of 9% error across all the angles, contribution is maximum (∼14%) for angles close to 90° and minimum for lower scattering angles (∼9%). Error due to uncertainty in angle measurement is computed by estimating the change in Compton and Rayleigh scattering cross-section and is found to be less than 0.1% at angles close to 90° and about 1% at other angles for an angle measurement uncertainty of 1°. Error due to uncertainty in coincidence time window is directly proportional to the amount of uncertainty present and its value is found to be 6% for uncertainty of 0.2 μs. Uncertainty in the central position of interaction reflects change in transmission probability of photons. Contribution of this is found to be of the order of 2% for 59.54 keV and 4% for 22.2 keV. Systematic errors are therefore angle dependent. We estimated combined systematic uncertainties to be 10% at lower and higher scattering angles and 16% at angles close to 90°. These are added to the statistical uncertainties in quadrature. Each measurement has been repeated several times to have confidence in the observed count rates and we have considered an average count rates from multiple measurements where necessary.

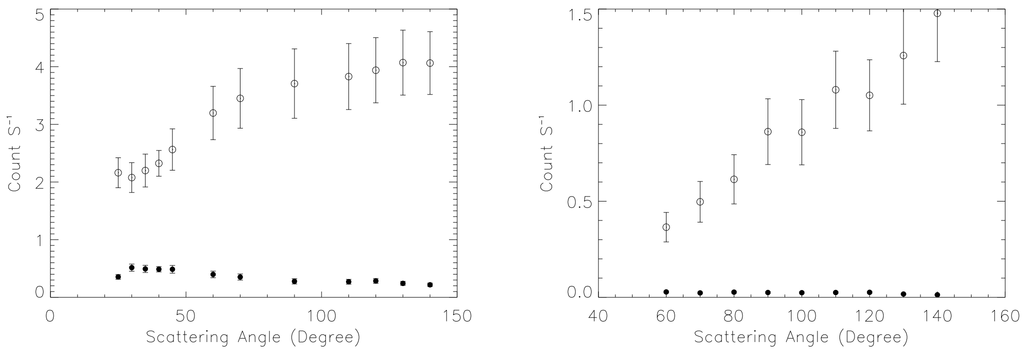

Figure 3.6: Observed count rate for 59.5 keV (left) and 22.2 keV (right) for coincidence (open circles) and non-coincidence (filled circles) modes as a function of scattering angles

Fig. 3.6 shows that, at higher angles the coincidence count rate is more than that in the non-coincidence count rate because of large energy deposition, which is above the threshold. As we move towards the lower scattering angles, because of lower energy deposition, fraction of valid Compton scattered photons decreases and consequently the coincidence and non-coincidence count rates tend to match each other. Thus this figure demonstrates the essence of our experiment in qualitative terms, that though the plastic scatterer is able to detect energy deposition as low as ∼1 keV, the efficiency of detection decreases gradually with decreasing energy.

However, these representations of count rate vs. scattering angles are not suitable for quantitative estimation of detection efficiency as a function of deposited energy in the scatterer because of the fact that the trigger rate in the plastic scatterer is not constant across all the scattering angles. In order to minimize the total exposure times, particularly in the coincidence mode, it is necessary to keep the source as close as possible from the scatterer. However, this distance is different for different scattering angles, which results in variation of the total trigger rate (i.e. total interactions including photoelectric and detectable Compton scattering interactions) in the plastic scatterer.

Therefore it is necessary to normalize count rates with respect to the number of triggers in plastic. If R_{trig} is the trigger rate in plastic for angle θ (obtained from Eq. 3.3), then normalized count rates, i.e. the number counts in the CdTe

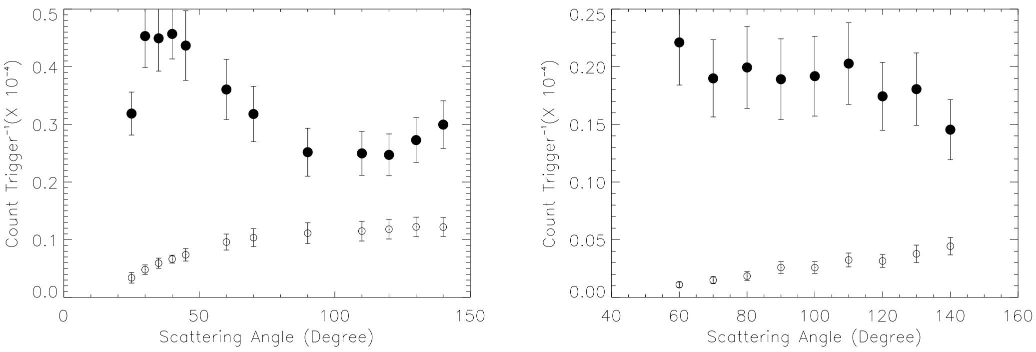

Figure 3.7: Normalised count rate with respect to the total number of triggers in plastic (see text for further details) for 59.5 keV (left) and 22.2 keV (right) as a function of scattering angles. Open and filled circles stand for coincidence and non-coincidence modes respectively.

detector per trigger in the plastic scatterer, at θ are given by

$$R_{co}^{norm} = \frac{N_{co}}{T_{co}^{exp} R_{trig}}, \tag{3.6}$$

$$R_{nco}^{norm} = \frac{N_{nco}}{T_{nco}^{exp} R_{trig}}. \tag{3.7}$$

Denominator in Eq. 3.6 and Eq. 3.7 is total number of triggers in plastic during the experiment. Fig. 3.7 shows the normalized rates in coincidence and non-coincidence modes for both the sources. Since, $T_{co}^{exp} \gg T_{nco}^{exp}$, the normalized rate in non-coincidence mode, represented by filled circles, is much higher than that in the coincidence mode, denoted by open circles. Since, statistical error on count rate is inversely proportional to exposure time, error in non-coincidence mode is larger too. We see that count rate in coincidence mode is decreasing in a steady manner. This clearly shows that the plastic scatterer does not have a sharp detection threshold, rather the detection efficiency gradually decreases with decreasing deposited energy.

It can be seen that the normalized count rate in non-coincidence mode is always greater than that in coincidence mode. For ^{241}Am, X-rays scattered at large scattering angles, the energy deposited in the scatterer is more than ~5 keV, which is always expected to generate a trigger in the scatterer. Thus it is expected that in this range the normalized rate in both non-coincidence and coincidence mode should be same, because of much smaller probability of the Rayleigh scattering at this energy. However, the fact that the observed normalized count rate in non-coincidence mode is higher than that in coincidence mode, suggests that the scattering events taking place in the material apart from the plastic scintillator, e.g. the surrounding Aluminum cylinder, because of the diverging beam, also contribute to the non-coincidence count rate. In coincidence mode, these events get suppressed due to the requirement of the simultaneity. This further suggests that the contribution of such events must be taken into account while estimating the number of chance coincidence events in the coincidence mode as well.

3.3 Numerical Modeling

Fig. 3.7 present the number of scattered photons detected by the CdTe detector at a given scattering angle for each trigger registered in the plastic scatterer. Since the scattering geometry of our experiment is fairly simple, in principle it should be possible to estimate this count rate using the knowledge of the Compton scattering cross-section of the plastic scatterer. However, we find that such simple minded calculation does not give count rate estimation, or the trend of its variation with scattering angle, which can be directly compared with the observed results. On further investigation, we find that it is essential to consider various factors such as -

- the finite scattering length as viewed by the CdTe detector through collimator,
- absorption of the incident photons by the entrance window in front of the plastic scatterer,
- absorption of the photons scattered from the plastic scatterer in the surrounding Aluminum,
- scattering of incident photons form the surrounding Aluminum itself,
- multiple-scattering within plastic and Al,

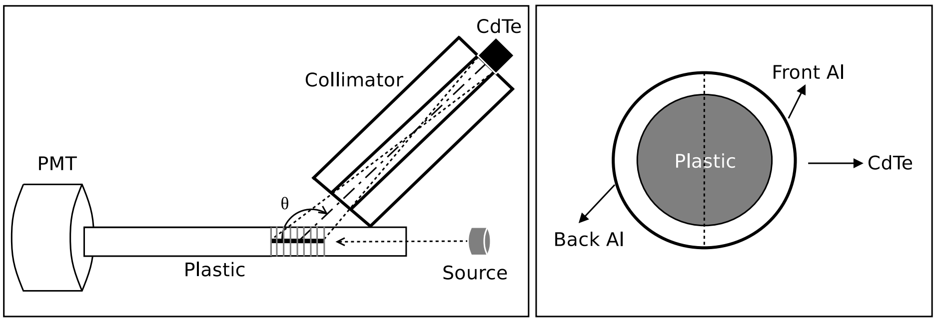

Figure 3.8: Left: Geometric representation of the experimental setup. In the model, total length of the plastic scatterer observed by the CdTe detector is calculated based on this geometry, which is then further divided into a large number of small segments as shown by the grey parallel lines. Right: Front surface of the plastic (5 mm diameter). Plastic is surrounded by 1 mm thick Al. Al surface facing the CdTe is named as front Al and opposite surface is back Al

- efficiency of CdTe at the scattered energies,
- scattering of photons from inner Aluminium surface of collimator etc.

We attempted to model the observed results including most of these factors.

We start with Klein Nishina cross-section [52] for Compton scattering

$$\frac{\mathrm{d}\sigma_{KN}}{\mathrm{d}\Omega} = \frac{r_0^2}{2}\left(\frac{E'}{E}\right)^2\left[\frac{E'}{E}+\frac{E}{E'}-\sin^2\theta\right], \tag{3.8}$$

where, E and E' are energies of incident and scattered photon respectively for scattering angle θ. From Eq. 3.8, one can obtain Thomson scattering cross section by substituting $E = E'$

$$\frac{\mathrm{d}\sigma_T}{\mathrm{d}\Omega} = \frac{r_0^2}{2}\left[1+\cos^2\theta\right]. \tag{3.9}$$

Here we assume that the photons from source are being scattered by plastic along its axis. For a given angle θ, range in angle of scattering and the scattering length are calculated from the known geometry (see Fig. 3.8).

Then we divide the scattering length into a large number of small segments and for each segment, both polar and azimuthal scattering ranges i.e. $\theta_{min,i}$, $\theta_{max,i}$ and $\phi_{min,i}$, $\phi_{max,i}$ subtended by the CdTe detector at the center of the i^{th} segment, are calculated. Cross-section of each segment for a photon to be scattered in the direction of the CdTe detector, is then estimated by integrating

Eq. 3.8 and Eq. 3.9 over these angle ranges,

$$\sigma_C(\theta, i) = \int_{\theta_{min,i}}^{\theta_{max,i}} \int_{\phi_{min,i}}^{\phi_{max,i}} \frac{\mathrm{d}\sigma_{KN}}{\mathrm{d}\Omega} \sin\theta \,\mathrm{d}\theta \,\mathrm{d}\phi, \tag{3.10}$$

$$\sigma_R(\theta, i) = \int_{\theta_{min,i}}^{\theta_{max,i}} \int_{\phi_{min,i}}^{\phi_{max,i}} \frac{\mathrm{d}\sigma_{T}}{\mathrm{d}\Omega} \sin\theta \,\mathrm{d}\theta \,\mathrm{d}\phi. \tag{3.11}$$

For integration over ϕ for i^{th} segment, we estimated ϕ_{min} and ϕ_{max} at both θ_{min} position and θ_{max} position and took average of ϕ_{min} and average of ϕ_{max} as limit of integration.

One important point to be noted here is the cross-sections in Eq. 3.8 and Eq. 3.9 are valid for scattering off free electrons. However, in case of realistic matters, the binding effect of electrons and their momentum distributions inside the atom introduces significant difference in the scattering distribution specially at the lower angles. Thus the numerical values obtained from Eq. 3.10 and Eq. 3.11 are expected to differ from the actual true values because of these effects. This point is specifically discussed in [104]. Though in our experiment forward scattering is not dominant, we accounted for these effects by considering more realistic scattering cross-sections by including atomic form factors and incoherent scattering functions into the calculations for the scattering atom under consideration as shown below,

$$\sigma_C(\theta, i) = \int_{\theta_{min,i}}^{\theta_{max,i}} \int_{\phi_{min,i}}^{\phi_{max,i}} \frac{\mathrm{d}\sigma_{KN}}{\mathrm{d}\Omega} S(x, Z) \sin\theta \,\mathrm{d}\theta \,\mathrm{d}\phi, \tag{3.12}$$

$$\sigma_R(\theta, i) = \int_{\theta_{min,i}}^{\theta_{max,i}} \int_{\phi_{min,i}}^{\phi_{max,i}} \frac{\mathrm{d}\sigma_{T}}{\mathrm{d}\Omega} |F(x, Z)|^2 \sin\theta \,\mathrm{d}\theta \,\mathrm{d}\phi. \tag{3.13}$$

where,

$$x = (E/hc)\sin(\theta/2) \tag{3.14}$$

$S(x, Z)$ and $F(x, Z)$ are the incoherent scattering functions and atomic form factors respectively for element of atomic number Z. The values of $S(x, Z)$ and $F(x, Z)$ as a function of x are obtained from [105]. For a given incident photon energy (E), it is possible to get these values as a function of scattering angle which typically ranges from 0° to 160°. For our purpose, we interpolated the form factor and scattering functions at each degree and used them in Eq. 3.12 and Eq. 3.13.

Since plastic is a compound material consisting of H and C atoms, form factors and scattering functions for plastic have been computed by taking proper weight factors into their individual form factors and scattering functions.

Dividing Eq. 3.12 and Eq. 3.13 by total Compton and Rayleigh cross-section for i^{th} section respectively, we get the probability of photons scattered by i^{th} segment reaching the CdTe detector, kept at angle θ,

$$P_C(\theta, i) = \frac{\sigma_C(\theta, i)}{\sigma_{C,tot}(i)}, \tag{3.15}$$

$$P_R(\theta, i) = \frac{\sigma_R(\theta, i)}{\sigma_{R,tot}(i)}, \tag{3.16}$$

where $P_C(\theta, i)$ and $P_R(\theta, i)$ are the fraction of total scattered photons by the i^{th} segment that reach CdTe. Total cross-sections have also been computed in a similar fashion by taking into account form factors and scattering functions.

To get the total number of Compton and Rayleigh scattered photons reaching the CdTe detector, it is necessary to multiply $P_C(\theta, i)$ and $P_R(\theta, i)$ by the probability of respective interaction taking place in the i^{th} segment. This probability is calculated using the mass attenuation co-efficients of Compton and Rayleigh scattering for the plastic scintillator obtained from the NIST data base [106].

If i^{th} segment has thickness 'S_p' ('p' stands for plastic), then the fraction of photons Compton scattered by that segment is $\frac{\mu_c^p}{\mu_t^p}[1 - \mathrm{e}^{-\mu_t^p \rho_p s_p}]$ and fraction of photons Rayleigh scattered is $\frac{\mu_r^p}{\mu_t^p}[1 - \mathrm{e}^{-\mu_t^p \rho_p s_p}]$. Here, μ_c^p, μ_r^p, μ_t^p are respectively the Compton, Rayleigh scattering attenuation coefficient and total attenuation coefficient of plastic at the incident photon energy, E. ρ_p is the density of plastic. Therefore, fraction of incident photons detected by CdTe at angle θ is given by

$$\begin{aligned} \frac{N_{nco}^p(\theta)}{N_0^p} = {} & \mathrm{e}^{-\mu_w \rho_w t_w} \sum_{i=0}^{N-1} \mathrm{e}^{-i\mu_t^p \rho_p S_p} \, \frac{\mu_c^p}{\mu_t^p} \, (1 - \mathrm{e}^{-\mu_t^p \rho_p S_p}) \, P_C(\theta, i) \\ & + \mathrm{e}^{-\mu_w \rho_w t_w} \sum_{i=0}^{N-1} \mathrm{e}^{-i\mu_t^p \rho_p S_p} \, \frac{\mu_r^p}{\mu_t^p} \, (1 - \mathrm{e}^{-\mu_t^p \rho_p S_p}) \, P_R(\theta, i). \end{aligned} \tag{3.17}$$

Summation is performed over all the segments (each of thickness 'S_p') in plastic. N is total number of segments. N_0^p refers to photons incident on plastic. The exponential term, $\mathrm{e}^{-\mu_w \rho_w t_w}$, takes into account the transmission through a thin window made of plastic (thickness, $t_w = 3$ mm; density, ρ_w; total absorption co-efficient at E, μ_w) at the front of plastic scintillator. The first and second part in Eq. 3.17 stands for Compton and Rayleigh events in plastic respectively. We have assumed 100% detection efficiency of CdTe which is a good approximation, as for 1 mm CdTe efficiency falls from 100% beyond 60 keV.

A fraction of these scattered photons will be absorbed by the surrounding front Al (see Fig. 3.8) of thickness 1 mm. However, the photon path length (absorption thickness) depends on scattering angle. Absorption coefficient of Al also depends on the scattered energy. Hence both these factors will vary from segment to segment. For simplicity in calculation, we estimated the photon path length corresponding to the mean of minimum and maximum scattering angle for each segment. Absorption co-efficient is also evaluated at energy corresponding to that mean scattering angle. The angle range being very small, this approximation holds good. If t^{fa} and $\mu^{fa}_{t,E'}$ (E' is the scattered energy corresponding to mean scattering angle) are the absorption thickness and total absorption co-efficient of front Al for i^{th} segment, then absorption factor is given by $\mathrm{e}^{-\mu^{fa}_{t,E'}\rho_a t^{fa}}$, where ρ_a is the density of Al and 'fa' stands for front Al. With the inclusion of this factor, Eq. 3.17 is modified to

$$\frac{N^p_{nco}(\theta)}{N^p_0} = \frac{N^{p,C}_{nco}(\theta)}{N^p_0} + \frac{N^{p,R}_{nco}(\theta)}{N^p_0}, \tag{3.18}$$

where, first (Compton) and second term (Rayleigh) are given by

$$\frac{N^{p,C}_{nco}(\theta)}{N^p_0} = \mathrm{e}^{-\mu_w\rho_w t_w}\sum_{i=0}^{N-1}\mathrm{e}^{-i\mu^p_t\rho_p S_p}\,\frac{\mu^p_c}{\mu^p_t}\,(1-\mathrm{e}^{-\mu^p_t\rho_p S_p})\,P_C(\theta,i)\,\mathrm{e}^{-\mu^{fa}_{t,E'}\rho_a t^{fa}}, \tag{3.19}$$

$$\frac{N^{p,R}_{nco}(\theta)}{N^p_0} = \mathrm{e}^{-\mu_w\rho_w t_w}\sum_{i=0}^{N-1}\mathrm{e}^{-i\mu^p_t\rho_p S_p}\,\frac{\mu^p_r}{\mu^p_t}\,(1-\mathrm{e}^{-\mu^p_t\rho_p S_p})\,P_R(\theta,i)\,\mathrm{e}^{-\mu^{fa}_{t,E}\rho_a t^{fa}}. \tag{3.20}$$

It is to be noted here that the attenuation coefficients of Aluminum needs to be taken at respective energies of the photon i.e. for Compton scattering it is the energy of the scattered photon and for Rayleigh scattering it is the energy of the incident photon.

As discussed earlier, it is essential to consider scattering from the Aluminum cylinder surrounding the plastic scatterer. Keeping the source opening and source-plastic distance in mind, it is assumed that radiation is uniform over the plastic and surrounding Al. We estimated the contribution in scattered photons from both front Al and back Al (see Fig. 3.8) with the same approach mentioned above. It is assumed that the photons are scattered along the axes of front and back Al and the angles of scattering have been calculated with respect to these axes. Therefore, the scattering angle range for any segment is different for different scatterers i.e. plastic, front Al and back Al. Fraction of photons scattered by front and back Al at angle θ is given by

$$\begin{aligned}\frac{N_{nco}^{fa}(\theta)}{N_0^{fa}} &= \mathrm{e}^{-\mu_w \rho_w t_w} \sum_{i=0}^{N-1} \mathrm{e}^{-i\mu_t^a \rho_a S_{fa}} \, \frac{\mu_c^a}{\mu_t^a} \, (1 - \mathrm{e}^{-\mu_t^a \rho_a S_{fa}}) \, P_C(\theta, i) \\ &+ \mathrm{e}^{-\mu_w \rho_w t_w} \sum_{i=0}^{N-1} \mathrm{e}^{-i\mu_t^a \rho_a S_{fa}} \, \frac{\mu_r^a}{\mu_t^a} \, (1 - \mathrm{e}^{-\mu_t^a \rho_a S_{fa}}) \, P_R(\theta, i), \end{aligned} \tag{3.21}$$

$$\begin{aligned}\frac{N_{nco}^{ba}(\theta)}{N_0^{ba}} &= \mathrm{e}^{-\mu_w \rho_w t_w} \sum_{i=0}^{N-1} \mathrm{e}^{-i\mu_t^a \rho_a S_{ba}} \, \frac{\mu_c^a}{\mu_t^a} \, (1 - \mathrm{e}^{-\mu_t^a \rho_a S_{ba}}) \, P_C(\theta, i) \, \mathrm{e}^{-\mu_{t,E'}^{fa} \rho_a t^{fa}} \, \mathrm{e}^{-\mu_{t,E'}^{p} \rho_p t^p} \\ &+ \mathrm{e}^{-\mu_w \rho_w t_w} \sum_{i=0}^{N-1} \mathrm{e}^{-i\mu_t^a \rho_a S_{ba}} \, \frac{\mu_r^a}{\mu_t^a} \, (1 - \mathrm{e}^{-\mu_t^a \rho_a S_{ba}}) \, P_R(\theta, i) \, \mathrm{e}^{-\mu_{t,E}^{fa} \rho_a t^{fa}} \, \mathrm{e}^{-\mu_{t,E}^{p} \rho_p t^p}, \end{aligned} \tag{3.22}$$

where, N_0^{fa} and N_0^{ba} are the incident photons on front Al and back Al respectively. Other symbols have their meaning as described earlier. It is to be noted that in Eq. 3.21, the absorption terms have been dropped because there are no source of absorption for photons scattered from front Al. However, the photons scattered from back Al will suffer absorption from the 5 mm plastic and the 1 mm front Al. These factors have been included in Eq. 3.22.

Now assuming uniform exposure of the incident X-rays over the plastic scatterer and surrounding Aluminum, it can be shown that if N_0^p is the number of photons incident on plastic, then number of photons incident on front and back Al are respectively $\frac{24}{50} N_0^p$ and $\frac{24}{50} N_0^p$ (diameter of plastic is 5 mm and diameter of plastic plus Al is 7 mm). Therefore, using Eq. 3.18, Eq. 3.21 and Eq. 3.22, one can obtain ratio of photons scattered into CdTe at angle θ to the number of photons incident on plastic as

$$\frac{N_{nco}(\theta)}{N_0^p} = \frac{N_{nco}^p(\theta)}{N_0^p} + \frac{24}{50} \, \frac{N_{nco}^{fa}(\theta)}{N_0^{fa}} + \frac{24}{50} \, \frac{N_{nco}^{ba}(\theta)}{N_0^{ba}}. \tag{3.23}$$

Now, the normalized count rate shown in Fig. 3.7, and as defined in Eq. 3.7, is the ratio of number of scattered photons detected by the CdTe detector to the total number of triggers in the plastic scatterer. Whereas the Eq. 3.23 gives the ratio of number of scattered photons likely to be detected by the CdTe detector to the total number of incident photons on plastic of the given energy, i.e. either 59.5 keV or 22.2 keV. These two ratios can not be compared directly because of the fact that both ^{241}Am and ^{109}Cd source emit photons of multiple energies and thus all triggers generated by the plastic scatterer included those generated by incident photons having energies other than that of interest. Here again it is possible to modify the ratio given by Eq. 3.23 based on the knowledge of the relative intensities of different lines emitted by both sources. However, exact values of relative intensities of the X-ray lines capable of generating triggers in the plastic scatterer are not available for the sources we have used during the experiment. Also, exact calculation of this ratio would require assumption of 100% trigger generation efficiency at all energies. Therefore, instead of calculating the ratio of incident photons to the triggers in the plastic scatterer, we modify Eq. 3.23 to include a fit parameter, α, representing this ratio. This parameter also takes into account any small deviation from the strict alignments of source to scatterer and scatterer to CdTe axis as assumed in the model, provided that the deviation is constant across all angles. Thus the final expression of the model is given by

$$\frac{N_{nco}(\theta)}{N_{trig}} = \frac{N^{p}_{nco}(\theta)}{\alpha\, N^{p}_{0}} + \frac{24}{50}\,\frac{N^{fa}_{nco}(\theta)}{\alpha\, N^{fa}_{0}} + \frac{24}{50}\,\frac{N^{ba}_{nco}(\theta)}{\alpha\, N^{ba}_{0}}. \tag{3.24}$$

Thus to quantitatively compare the observed results with expected values, we fit Eq. 3.24 to the results shown in Fig. 3.7 and obtain best fit value of the parameter, α, by χ^2 minimization.

3.4 Modeling Results and Discussions

Fig. 3.9 shows the fitted model (thick solid line, Eq. 3.24) with the experimental results. For ^{241}Am, the best fit value for parameter α is 3.65, whereas for ^{109}Cd, it is 0.88. These values are reasonably close to the values expected from the available data for relative intensities of different X-ray lines for both ^{241}Am and

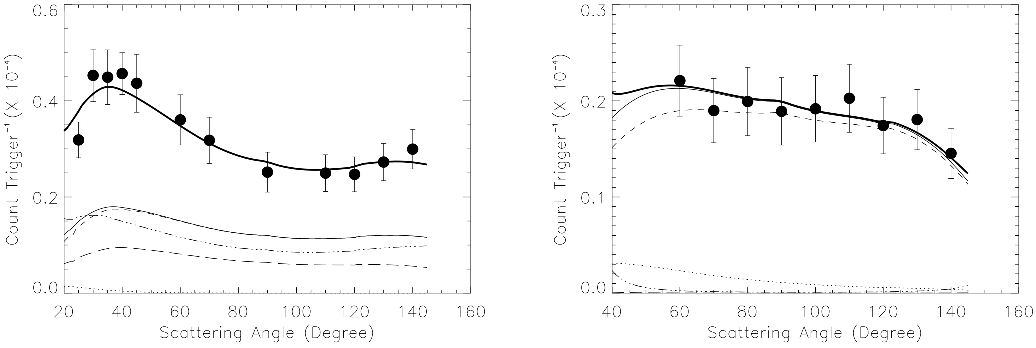

Figure 3.9: Observed count rate in the non-coincidence mode fitted by the model. Left plot corresponds to 59.5 keV and right plot corresponds to 22.2 keV photons. The thick solid line represents final model (Eq. 3.24) whereas the thin lines represents different components of the model - dashed lines: Compton scattering events from plastic; dotted lines: Rayleigh scattering events from plastic; solid lines: sum of Compton and Rayleigh events from plastic; dashed dot dot: scattering events from front Al; long dashed: scattering events from back Al. Best fit values of the parameter of the fitted curve are 3.65 and 0.88 for 59.5 keV and 22.2 keV respectively

^{109}Cd source. Different components of the model are shown in Fig. 3.9: Compton scattering events from plastic (dashed, Eq. 3.19), Rayleigh scattering events from plastic (dotted, Eq. 3.20), combined Compton and Rayleigh events from plastic (thin solid, 1st term of Eq. 3.24), scattering events (Compton + Rayleigh) from front Al (dashed dot dot, 2nd term of Eq. 3.24) and back Al (long dashed, 3rd term of Eq. 3.24) surrounding the plastic.

This model so far is aimed at reproducing the observed count rate in the non-coincidence mode i.e. the scatterer is considered to be passive. The observed count rate in the coincidence mode can be estimated from Eq. 3.19 along with the chance coincidence rate due to all other terms i.e. Rayleigh scattering in plastic scatterer (Eq. 3.20), scattering from the Aluminum cylinder (2nd and 3rd terms of Eq. 3.24) as well as chance coincidence of the real Compton scattering events which failed to generate trigger. The chance coincidence fraction of these terms can be given by the product of trigger rate in plastic scatterer and the width of the coincidence window i.e.,

$$f_{ch} = T_{win} R_{trig}, \tag{3.25}$$

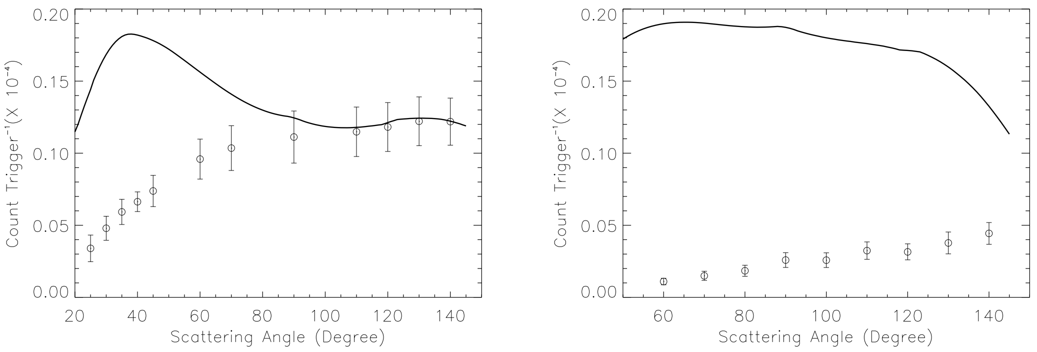

Figure 3.10: Comparison between experimentally obtained coincidence count rate and modelled count rate assuming 100% detection probability of plastic. Left plot shows the comparison for 59.5 keV. Right plot shows the comparison for 22.2 keV

where, f_{ch} is the chance coincidence factor. Thus the total expected count rate in the coincidence mode can be expressed as

$$R_{co}^{norm}(\theta) = \frac{N_{nco}^{p,C}(\theta)}{\alpha\, N_0^p}\, P(E) + \frac{N_{nco}^{p,R}(\theta)}{\alpha\, N_0^p}\, f_{ch} + \frac{24}{50}\, \frac{N_{nco}^{fa}(\theta)}{\alpha\, N_0^{fa}}\, f_{ch} + \frac{24}{50}\, \frac{N_{nco}^{ba}(\theta)}{\alpha\, N_0^{ba}}\, f_{ch} + \left(\frac{N_{nco}^{p,C}(\theta)}{\alpha\, N_0^p} - \frac{N_{nco}^{p,C}(\theta)}{\alpha\, N_0^p}\, P(E) \right) f_{ch}, \tag{3.26}$$

where, α is the best fit parameter obtained from fitting the non-coincidence mode data. The Compton scattering term is multiplied by the energy dependent probability of generating trigger in the plastic scatterer for given energy deposition. All the terms in this equation, except the detection probability $P(E)$, can be estimated using Eq. 3.6, Eq. 3.18, Eq. 3.21 and Eq. 3.22. Comparison of the expected count rate from Eq. 3.26, assuming the detection probability to 100%, with the observed count rate in the coincidence mode is shown in Fig. 3.10. We see that at higher scattering angles for ^{241}Am, modelled and experimental coincidence count rate agrees well with each other implying 100% detection probability at those energies. At lower angles for both the sources, experimental values are significantly less than the model values indicating lower detection probability at lower energies. This probability can be determined directly by comparing model values with the observed values and are shown in Fig. 3.11 for both ^{241}Am (represented by open triangles) and ^{109}Cd (represented by filled triangles) sources. Here the X-axes are converted from the scattering angles into the deposited ener-

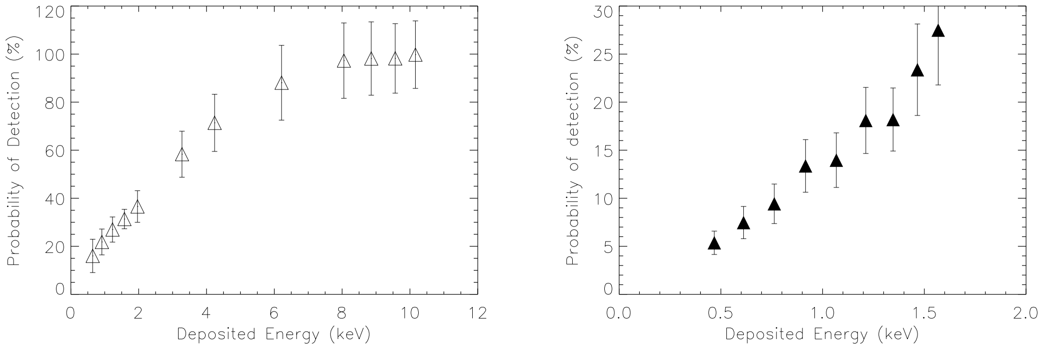

Figure 3.11: Detection Probability of plastic scintillator as function of deposited energy in plastic. Left: probability of event detection obtained 59.5 keV photons. Right: Detection probability estimated from 22.2 keV.

gies corresponding to scattering of incident photons (59.5 keV and 22.2 keV) at those angles. Fig. 3.12 shows combined data from both the sources as uniformly increasing trigger generation efficiency of the plastic scatterer in the energy range of 0.4 keV to 10 keV. It can be seen that there is common energy range of 0.65 keV to 1.55 keV, in the energy depositions by both the sources, corresponding to small angle of scattering of 59.5 keV photons and large angle scattering of 22.2 keV photons, and the observed values for both the sources agree well with each other. The small angle scattering of 22.2 keV photons gives ∼6% detection efficiency at energies down to ∼0.5 keV, which then increases almost linearly up to 3.0 keV. At energies greater then 7 keV, the detection efficiency almost saturates at 100%, as expected. The observed variation of detection efficiency can be fitted by an empirical polynomial given in Eq. 3.27,

$$P(E) = 0.028\,E^3 - 1.654\,E^2 + 24.218\,E - 5.5633\;. \tag{3.27}$$

It is important to note few points regarding our modeling - 1) This expression for the variation of detection efficiency as a function of energy depends on other experimental factors such as HV bias for the PMT and comparator threshold of the front-end electronics as well as the specific configuration of the plastic scatterer and its encapsulation. However, our modeling does not depend on these factors as the model fitting is with respect to the observations in the non-coincidence mode. Thus any further optimization of the experimental factors

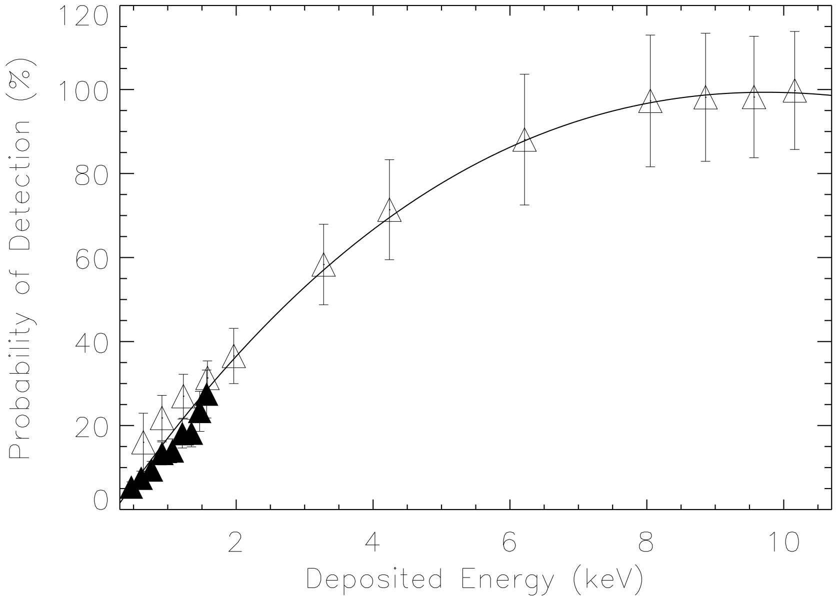

Figure 3.12: Detection probability as a function of deposited energy from 0.4 keV to 10 keV. Filled and open triangles correspond to 22.2 keV and 59.5 keV photons respectively. These data points have been fitted with an empirical polynomial shown by solid line.

would only influence the observed count rate in coincidence mode and thus would automatically result in better detection efficiency from the same model. 2) This expression represents the worst case scenario in terms of the interaction position within the plastic scatterer because in our present experiment, only the interactions within top couple of centimeters of the plastic scatterer are considered. For deeper interactions, the trigger generation efficiency may be slightly better due to reduced light path but surely not worse than the present case. 3) This empirical expression is valid for our configuration of the plastic scatterer (e.g. 10 cm long and 5 mm diameter BC404). For any other configuration, though the general trend is expected to be same, the exact expression needs to be measured separately. It is to be noted that our results agree well with the results reported in [102] particularly for higher energy depositions. At lower energies, detection probability for our plastic configuration is slightly less which could be because of the fact that they used a smaller scatterer (3 cm) with scattering material of higher light yield compared to BC404. On the other hand, detection probabilities of the plastic scatterer in X-Calibur/PolSTAR as reported in [76] are systematcally less compared to our results which is expected as the plastic in X-Calibur/PolSTAR is comparatively longer around 14 cm.

Now that we have an empirical expression representing the detection efficiency for our configuration of the plastic scatterer, we can use that to estimate the sensitivity of the Compton polarimeter more accurately. In Chapter 2, we investigated the sensitivity of a hard X-ray focal plane Compton polarimeter comprising the same configuration of the plastic scatterer and coupled to the NuSTAR type of hard X-ray optics. The MDP of this configuration of polarimeter was found to be 0.9% in 1 Ms for 100 mCrab source, when the threshold for the scatterer was assumed to be 1 keV. The MDP for threshold of 2 keV was found to be 1.2% for the same conditions. We reanalyzed the data from the same simulations using the above expression for energy dependent detection efficiency (see Eq. 3.27) of the plastic scatterer and the results are shown in Fig. 3.13. It can be seen that the MDP for the same conditions (1 Ms exposure for 100 mCrab source) is 1.2%, indicating slightly degraded but more realistic sensitivity. The lower energy limit for polarization measurement is also improved to ∼14 keV because of finite probability of detecting energy depositions as low as ∼0.5 keV by the plastic scatterer. However, it should be noted that at energies less than ∼20 keV, the properties of the material between the scatterer and the absorber, in our case 1 mm and 0.5 mm Aluminum surrounding scatterer and in front of the absorber respectively, become very important as the scattered photon has to pass through it without undergoing any further interaction. We attempted to replace the Aluminum by lower-Z materials in our simulations, but the results were not very encouraging because of the enhanced scattering in the intervening low-Z material, which degraded overall modulation pattern of the scattered photons. Thus we find that, in order to improve the sensitivity as well as overall efficiency of the Compton polarimeter, apart from the obvious optimization of the plastic scatterer configuration and associated electronics, it is equally important that the material between the scatterer and the absorbers has higher atomic number to reduce scattering, and is as thin and uniform as possible to enhance transmission

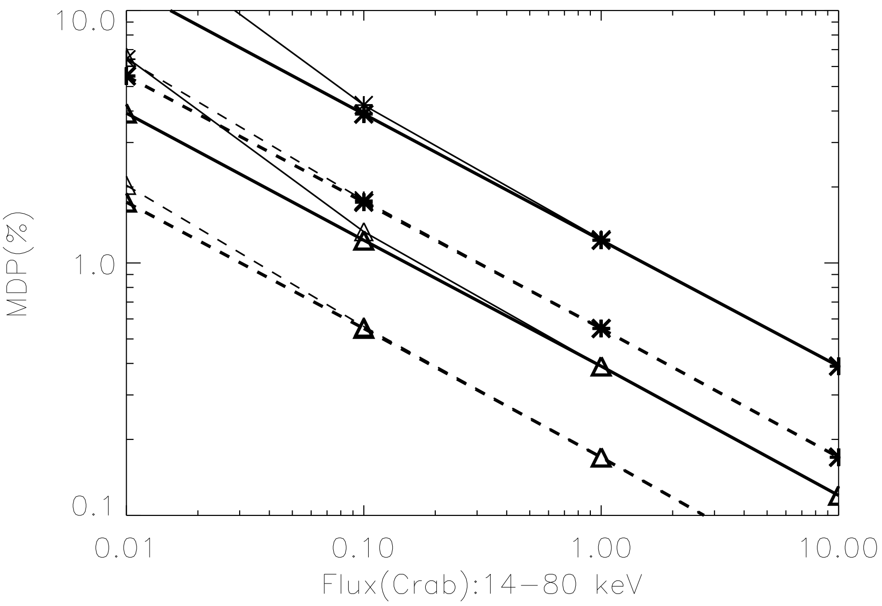

Figure 3.13: MDP as a function of source intensity. Triangles and asterisks stand for 1 Ms and 100 ks exposure respectively. Solid lines refer to single NuSTAR collecting area of mirror. Dashed lines refer to five times NuSTAR mirror area. Different background rates have been denoted by thick and thin lines. For bright sources, MDP is below 1%. However, it is to be noted that eventual polarization sensitivity will be limited by systematics of the instrument.

of the photon scattered from the central scatterer. Overall, we find that polarization measurements down to ∼15 keV are certainly possible using Compton polarimeter. Since many celestial sources are expected to have energy dependent X-ray polarization signatures, it is important to take into account the detection efficiencies of the active scatterer specially at the lower energies while interpreting the eventual energy integrated polarization measurements.

3.5 Characterization of CsI(Tl) Scintillators

In Chapter 2, we described simulation analysis of the Compton polarimeter assuming 32 CsI scintillators in cylindrical array. In the final experimental configuration of the Compton polarimeter, the scattered photons from the plastic scatterer are collected by 16 CsI(Tl) scintillators as shown in Fig. 3.14). Each of

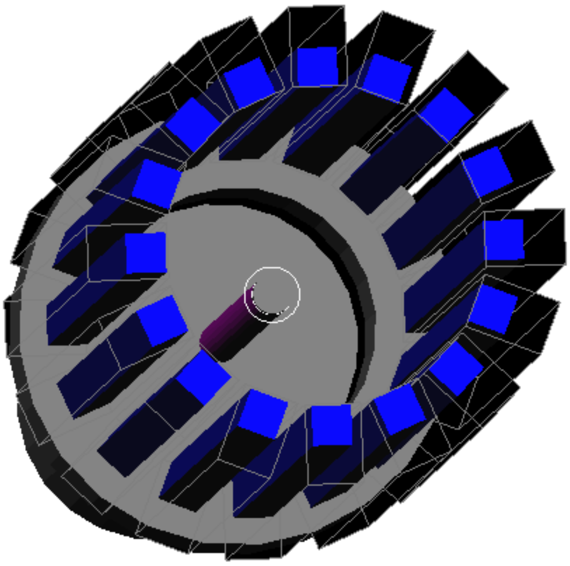

Figure 3.14: Planned Compton polarimeter configuration. The photons scattered by the central plastic scatterer (10 cm long with 5 mm diameter) are collected by a cylindrical array of 16 CsI(Tl) scintillators (each 15 cm long and 5 mm × 5 mm cross-section). In Chapter 2, we showed simulation for the Compton polarimeter geometry assuming 32 absorbers; however in the current experimental configuration, 16 CsI(Tl) scintillators have been used

the CsI(Tl) crystal is 15 cm long and 5 mm × 5 mm cross-section (see Fig. 3.15), procured from Saint-Gobain. The CsI(Tl) crystals are known to have high light yield, however, for our initial experiment these crystals are selected primarily because of their less hygroscopic nature compared to other well known inorganic scintillators such as NaI(Tl) or $LaBr_3$(Ce), which makes them easier to handle in the laboratory. One important drawback of CsI(Tl) scintillator is the long scintillation decay time, which is particularly severe in the context of readout by SiPM. Thus our results with CsI(Tl) readout by SiPM are expected to be worst case scenario and could be significantly improved with faster scintillators.

Each of the CsI(Tl) crystals are kept inside an aluminium case which encloses the crystal from all sides except the side facing the scatterer and the lower end for readout. The aluminium case is 5 mm thick on the back and 1 mm thick on the both sides. Each of the scintillators is read by a single Si photomultiplier (SiPM) at one end of the CsI(Tl). SiPM is a multi-pixel semiconductor photodiode system

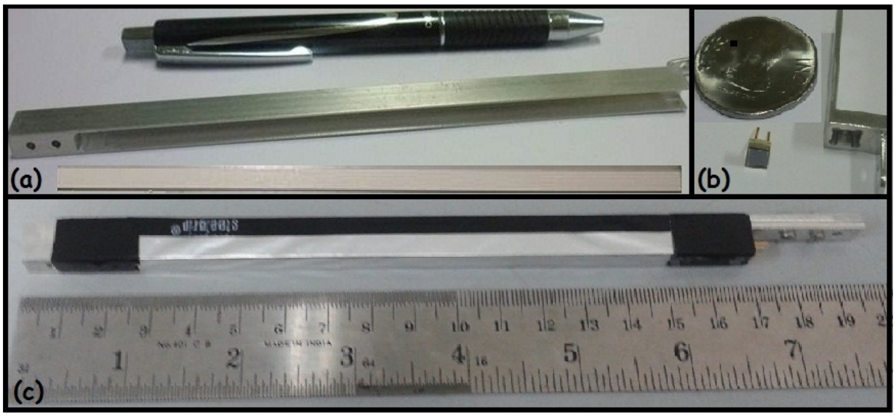

Figure 3.15: (a) A CsI(Tl) scintillator (5 mm × 5 mm × 150 mm) and its aluminium holder. (b) A Si photomultiplier (3 mm × 3 mm) with its aluminium case. (c) The complete CsI(Tl)-SiPM package. The CsI(Tl) is coupled to the SiPM using optical glue and wrapped by a thin aluminium foil for light tightness. 16 such CsI(Tl)-SiPM systems have been used in the final Compton polarimeter configuration

with pixels on a common Si substrate. SiPM work in Geiger mode (bias voltage > breakdown voltage), which provides high gain ($\sim 10^6$) making it sensitive even for single photon detection. The details of working principle of SiPM and other properties can be found in [107–109].

We used SiPM procured from KETEK, Germany (SiPM PM3350), with active area of 3 mm × 3 mm (see Fig. 3.15). The device is small, light, and robust with low operation voltage (~31 V) and therefore easier to handle and provides the compactness necessary for focal plane detectors. The wide spectral range from 300 nm to 800 nm (peak wavelength 420 nm) nicely matches with the CsI(Tl) emission spectra. There are 3600 micro-pixels (each of 50 μm × 50 μm) in a single device. An incident photon on any micro-pixel triggers an avalanche. In low light conditions, the number of fired micro-pixels is directly proportional to the number of photons incident on entire active surface. Hence in such conditions the SiPM can be used to measure the intensity of incident light by adding the signals from all the fired micro-pixels, though individual micro-pixels are operating in Geiger mode. One major problem with SiPM is the constant leakage current resulting from the random firing of micro-pixles due to thermal and field excitations inside Si, which makes it difficult for lower energy applications. At energies beyond

100 keV, SiPM device has been proved to be a much better readout option for scintillators than conventional vacuum PMTs [110, 111]. Here we plan to use SiPM to read out CsI(Tl) crystals at energies below 100 keV, which essentially depends on many factors like background level in the SiPM (typically ≤ 500 kHz/mm^2), good coupling between the crystal and SiPM, lower electronic noise, and on the scintillator properties (good light collection efficiency and small decay constant). An aluminum holder is used to keep the SiPM and couple it at the end of the CsI(Tl). For better coupling, optical glue with suitable refractive index is used between CsI(Tl) and SiPM. The whole system is then wrapped by thin aluminium foil from all sides to make it light tight (see Fig. 3.15).

The front end electronics for a single CsI(Tl)$-$SiPM system readout is shown in Fig. 3.16. The output of the SiPM is read by a charge sensitive pre-amplifier (RC type CSPA) utilizing ac coupling between CSPA and SiPM. The signal, in this way, is always detected at the top of the constant background leakage current. The output of the CSPA is given to a pulse shaping amplifier (CR$-$RC$-$RC), with 3 μs peaking time. The shaped pulse output is accepted by a multi channel

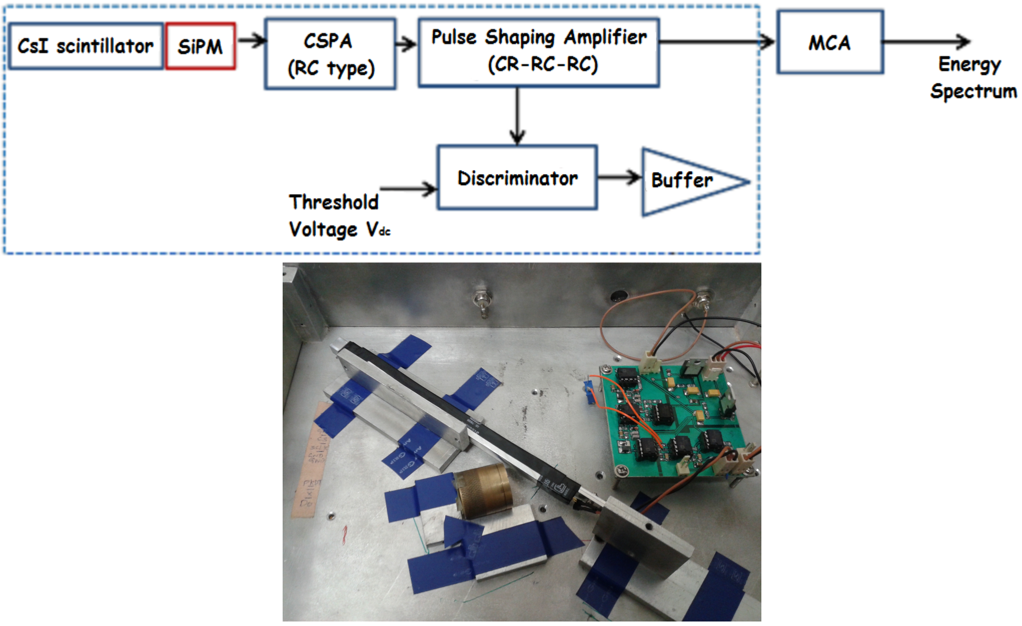

Figure 3.16: Top: Schematic of the SiPM electronic readout consisting of CSPA, pulse shaper and MCA. Bottom: Experiment setup to characterize CsI(Tl)-SiPM system

Analyser (MCA) to record spectra from CsI(Tl). 16 similar electronic chains are developed for read out of 16 CsI(Tl) bars. All 16 scintillators as well as electronic chains are not expected to have absolutely identical characteristics because of factors like unequal coupling between scintillators and SiPM and variation in gain across the electronics chains. Therefore, we characterized each of the 16 CsI(Tl)-SiPM detectors with multiple radio active sources (^{241}Am, ^{109}Cd, ^{57}Co) in the energy range of 20−130 keV, which is also the polarimetric energy range of the instrument. The experiment setup is shown in Fig. 3.16.

Fig. 3.17 shows the spectra for ∼26 keV and 59.54 keV lines (^{241}Am) in black, 22 keV and 88 keV lines (^{109}Cd) in red and 122 keV line (^{57}Co) in blue obtained from one of the CsI(Tl) scintillators. The presence of 22 keV line clearly shows that lower energy threshold of CsI(Tl)-SiPM is ∼20 keV which is essential as we plan a lower energy cut off of ∼20 keV for the Compton polarimeter. However, it is to be noted that spectra shown in Fig. 3.17 is obtained when the sources are kept close to SiPM. For interactions far away from SiPM, we expect less light to reach SiPM device and because of reflections inside the scintillator, light signal is expected to be diffused as it reaches the SiPM plane. Therefore,

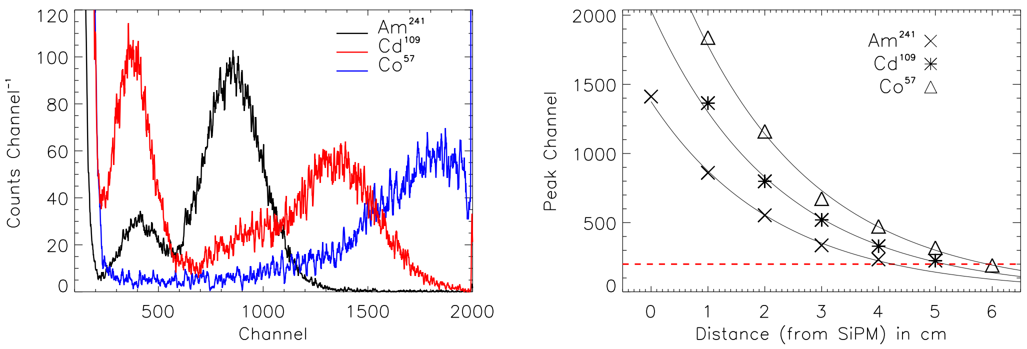

Figure 3.17: Left: Spectrum obtained from a CsI(Tl)-SiPM system for 26 and 59.5 keV photons from ^{241}Am (black), 22 and 88 keV photons from ^{109}Cd (red), and 122 keV photons from ^{57}Co (blue). Right: Detection probability of CsI(Tl) as a function of distance from the SiPM for 59.5 keV (cross), 88 keV (asterisk) and 122 keV photons (triangle). The solid lines are the exponential fit to the experimental data. The red dashed line denotes the typical background level in the spectrum in ADC channel unit

we investigate the response of CsI(Tl) as a function of distance from SiPM by changing the source position with a step of 1 cm. The sources are kept very close to the CsI(Tl) to make sure that interaction takes place in a very small region in CsI(Tl). For each source position, we acquire the spectra and fit the individual lines with Gaussian profile to estimate the peak channel of the lines. The fitted peak channels are plotted as a function of distance as shown in Fig. 3.17. We find that the peak channel (ADC) of detection falls off exponentially with distance from SiPM. The dashed red line at 200^{th} ADC channel indicates the background level in the spectra. We see that for 59.5 keV photons from ^{241}Am, the sensitivity degrades significantly beyond 4 cm. Similarly for 88 keV and 122 keV photons, the effective length of CsI(Tl) is ∼5 cm and 6 cm respectively. The steep fall in detection probability is mainly because of diffusion of light signal each time the photons undergo reflections inside CsI(Tl). Though, better response is expected with better optical coupling between CsI(Tl) and SiPM, these results indicate that CsI(Tl) scintillators as long as 15 cm are not suitable as absorbers in Compton polarimeter particularly when viewed by a single SiPM at one end. However, we expect better performance in case of faster scintillators like $LaBr_3$(Ce), $CeBr_3$ etc. with light output similar to that of CsI(Tl) as even for distant interactions, number of photons reaching SiPM at an instant is higher compared to that of slower scintillators like CsI(Tl). As discussed earlier, such a steep fall in detection probability with distance is expected for slow scintillators like CsI(Tl) particularly with SiPM readout. In spite of that, we selected CsI(Tl) scintillators for this proof of concept experiment mainly due to the fact that these are less hygroscopic compared to the other inorganic scintillators and therefore comparatively easier to handle in the laboratory. In the later versions of the polarimeter, we plan to use faster scintillators with SiPM readout as absorbers. We also verify for the linearity of the detectors in this energy range for different source positions to estimate gain and offsets. Scintillator to scintillator variation in gain for a fixed position is found out to be insignificant, which is important for polarimetry applications.

3.6 Polarization Experiment with CXPOL

After characterizing each of the 16 CsI(Tl) scintillators, all of them are integrated on the Compton polarimeter housing in the form of cylindrical array to test the performance of the polarimeter with polarized radiation beam. The supporting structure to hold the absorbers surrounding the central plastic is made of aluminium. It should be noted that the simulations results, reported in Chapter 2, were carried out with total 32 absorbers having slightly larger diameter (5.3 cm) of the cylindrical array, whereas the current polarimeter configuration has diameter of 4 cm. The modulation pattern is not expected to change significantly with 16 absorbers because the azimuthal bin sizes are all equal. Position of the plastic can be altered within the polarimeter structure. In the original polarimeter configuration, the plastic scatterer was planned to be kept at the base of the polarimeter, making full length of the scatterer available for the coincident detection. However, since the CsI(Tl) scintillators were found to be sensitive only at the lower $\sim$5$-$6 cm at energies $\sim$50 keV, the plastic scatterer was pushed out by 5 cm to ensure that scattered photons from the top portion of the scatterer interact within the active length of CsI(Tl).

The coincidence between the plastic and the CsI(Tl) absorbers is established utilizing the gated mode operation using FPGA. The schematic of the coincidence unit is shown in Fig. 3.18. The output of the first stage amplifier in the SiPM readout chain is given to a discriminator, which compares the output with a fixed threshold voltage and gives signal for the presence of a photon. The fixed voltage is optimized to reject a major fraction of noisy signals. All 16 discriminator outputs and the discriminator output of the central plastic scintillator are given to the FPGA based counting system. All the 17 signals are counted on the rising edge of the clock of FPGA. When there is a signal from the plastic scintillator, FPGA records the presence of all other 16 Compton scattered signals for $\sim$6 μs coincidence time window. Based upon the coincident detection (within 6 μs window) of signal from the plastic scatterer and XORed signal of the 16 CsI(Tl) signals (to avoid multiple scattering due to fluorescence photons from CsI(Tl)), the detected signals are sent to a LabVIEW data acquisition software which takes

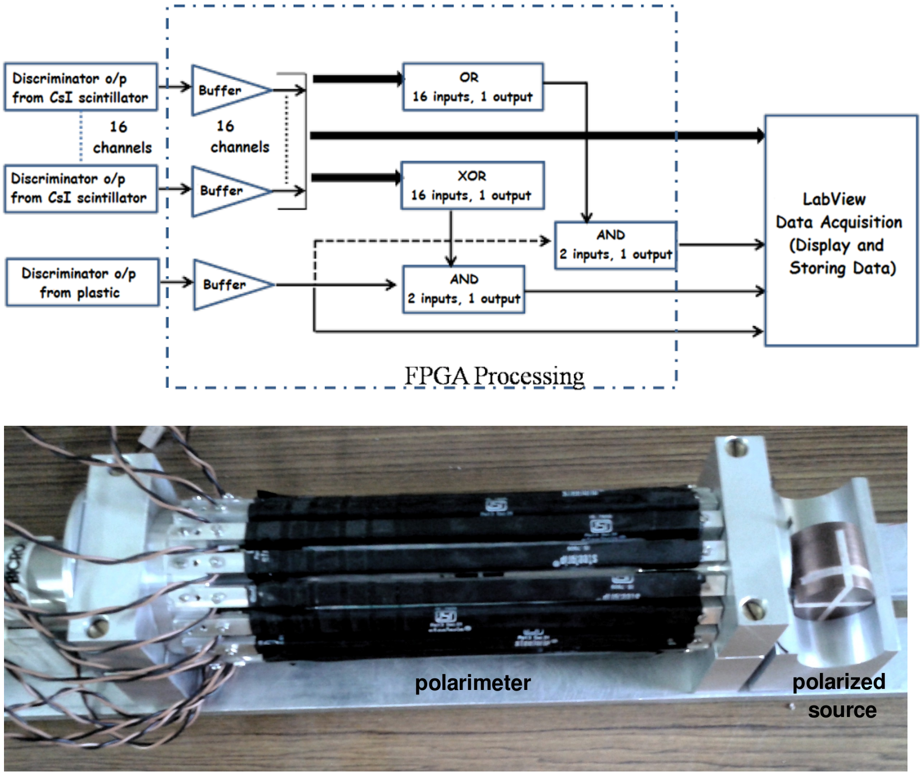

Figure 3.18: Top: Schematic of the coincidence unit between the plastic scatterer and the CsI(Tl) absorbers. Bottom: Polarization experiment setup with the fully integrated configuration of the Compton polarimeter. The polarized source of radiation (shown in the figure) employs 90° Compton scattering of the unpolarized photons from radioactive sources (see text for details)

the packet data from the FPGA and store in an output file for further analysis.

Fig. 3.18 shows the polarimetric configuration and experiment setup to investigate the response of CXPOL to unpolarized and polarized beam of radiation. The source is kept outside the polarimeter case. In order to make sure that the photons do not diverge and impinge directly on the CsI(Tl) scintillators, we used a long lead-aluminium collimator at that end. The azimuthal distribution for an unpolarized beam is shown in Fig. 3.19. The plastic scatterer is exposed to 59.5 keV photons from ^{241}Am. We see that there is no significant modulation in the azimuthal angle distribution. The distribution is fitted with a $\cos^2\phi$ function (shown by black line) –

$$C(\phi) = A\cos^2(\phi - \phi_0) + B, \tag{3.28}$$

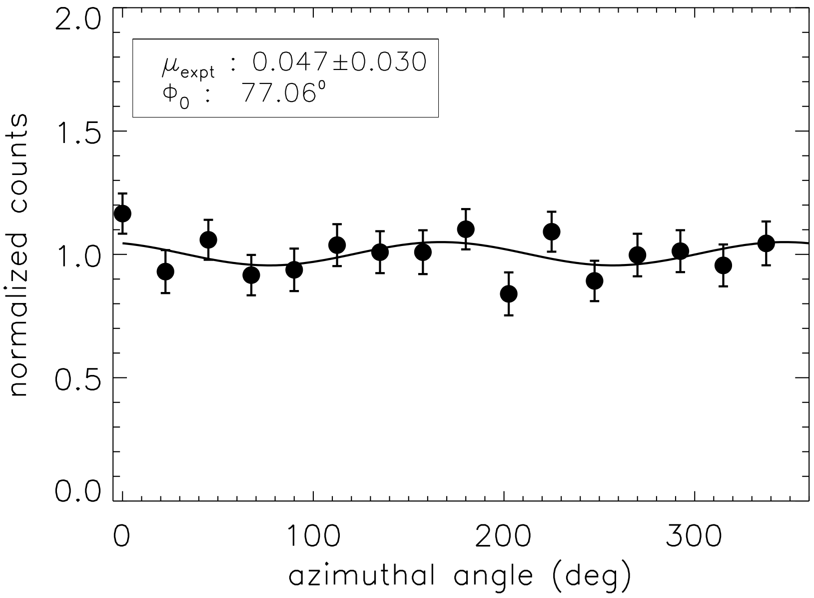

Figure 3.19: Azimuthal angle distribution for unpolarized 59.5 keV photons. The distribution is fitted by a $\cos^2\phi$ function (see Eq. 3.28) shown by black line

where A, B, and ϕ_0 (angle of polarization) are the fitting parameters. Amplitude of modulation in the azimuthal angle distribution is given by modulation factor

$$\mu = \frac{A}{A+2B}. \tag{3.29}$$

Modulation factor is directly proportional to the polarization fraction of the beam. The small nonzero modulation in this case is because of slight difference in gains between the scintillators.

We tested the response of CXPOL to a partially polarized beam of 54 keV, obtained by 90° scattering of 59.5 keV photons from ^{241}Am. An aluminium rod was used as scattering element. Both the scatterer and the source were kept inside a thick lead cylinder with a 2 mm diameter hole perpendicular to the incident beam direction. Spectrum of the polarized beam as taken by a separate CdTe (Amptek X123CdTe) detector is shown at the top of the left column in Fig. 3.20. The broad peak centered around 54 keV is the scattered polarized beam. The narrow beam at ~59.5 keV is the Rayleigh scattered photons of the original 59.5 keV photons from ^{241}Am. We estimated the polarization fraction of the beam numerically. The overall polarization will depend on the energy of the incident

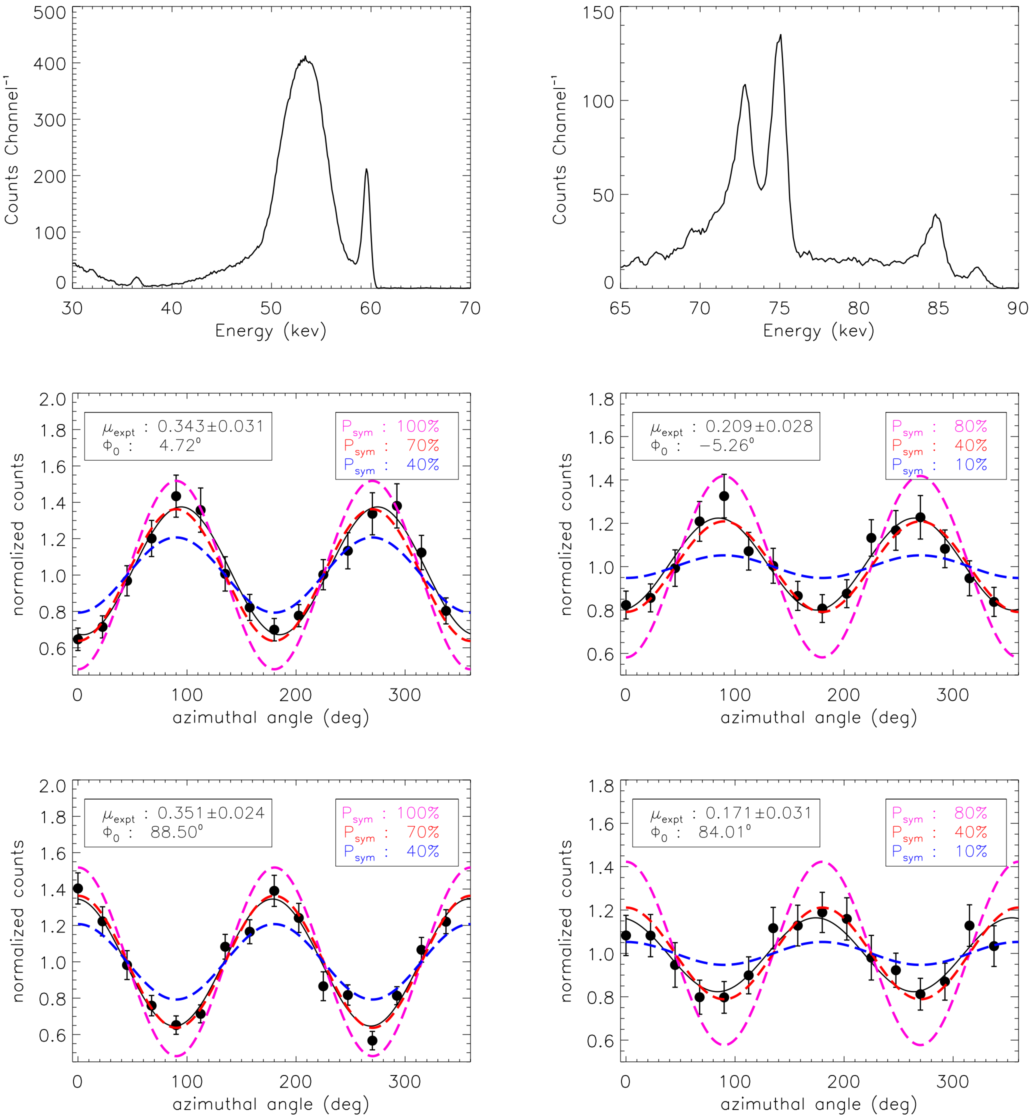

Figure 3.20: Left column: Top - Spectrum (taken from CdTe detector) of polarized 54 keV beam obtained by 90° scattering of 59.5 keV photons from ^{241}Am. Middle and Bottom - Azimuthal angle distribution for the partially polarized 54 keV beam for polarization angles of 0° and 90° respectively. The solid black line is the fit to the experimental data, whereas the dashed lines are obtained from simulation for the setup for polarization fractions of 100% (pink), 70% (red) and 40% (blue). Right Column: similar to the left column, obtained from ^{109}Cd. In this case, the amplitude of modulation is less due to the presence of unpolarized lead fluorescence photons (72 and 84 keV) as shown in the spectrum (see text for details)

photons and the geometry of scattering of the source. The fraction of polarization turns out to be ~75%. When this partially polarized beam is incident on the CXPOL, we see a clear enhanced modulation for the polarized beam compared to the unpolarized case at 0° and 90° polarization angles (see left column of Fig. 3.20). Different polarization planes are achieved by rotating the lead cylinder with respect to the plastic axis. First we take background data for long exposure which is then subtracted from source data. The modulation patterns are fitted with $\cos^2\phi$ function (see Eq. 3.28) shown by solid black line. Modulation factors for both the polarization angles are found to be ~0.35. To compare the fitted modulation factors with simulation results, we performed Geant−4 simulation for the current configuration of the polarimeter. Modulation factor for 100% polarized 54 keV beam (μ_{100}) is found to be ~0.50. The conventional way to obtain the degree of polarization of any partially polarized beam is to take ratio of the experimentally obtained modulation factor μ_{expt} to the simulated μ_{100} i.e.

$$P = \frac{\mu_{expt}}{\mu_{100}}. \tag{3.30}$$

This results in a polarization fraction of ~70 ± 8%, which is in good agreement with the numerically estimated value for the 54 keV polarized beam. This is also demonstrated in Fig. 3.20, where the modulation curves obtained from simulation are shown in dashed lines, where pink, red, and blue denote 100%, 70%, and 40% polarization respectively. The experimental data agree well with the 70% polarized signal, as expected.

We repeated the same experiment with partially polarized beam from ^{109}Cd source. The plot at the top of the right column of Fig. 3.20 shows the spectrum of this beam centered around 75 keV (90° scattering of 88 keV photons from ^{109}Cd). These 88 keV photons induce fluorescence emission (72 keV and 84 keV) from the surrounding lead enclosure as seen in the spectrum. These unpolarized photons are expected to decrease the polarization fraction of the beam. Eventual polarization degree is expected to be ~38% in this case, estimated taking into account the area under the 72, 84 and 75 keV peaks. The modulation curves for 0° and 90° polarization angles are shown in the right column of Fig. 3.20, along with the modulation patterns obtained from simulation for different polarization fractions. Modulation factors are found to be low (∼0.20) indicating the beam is ∼40% polarized.

To further test the polarimetric performance of CXPOL at lower energies, we used an X-ray gun (Amptek Mini-X X-Ray Tube with Gold target) to obtain a continuum polarized beam. The X-ray gun emits in $10 - 50$ keV range. The lower energy photons (≤ 20 keV) are blocked using a thin aluminium filter. We employed a similar method to polarize the continuum emission from the X-ray gun. An aluminium scatterer inside a lead cylinder was kept at the end of the gun tube (see Fig. 3.21). A small opening of 2 mm diameter ensures that the photons scattered at 90° can only reach the plastic scatterer. Spectrum of the polarized beam as taken from CdTe detector is shown in Fig. 3.21. We see the beam is continuum in 20−50 keV range. Because of the constrained geometry, we expect a higher degree of polarization in this case. Modulation curves at 0°, 90° and 45° polarization angles are shown in Fig. 3.22. In simulation, we employed a broad Gaussian beam centered around 35 keV as the source of polarized radiation. Azimuthal angle distributions for all the polarization planes are found to be highly modulated consistent with $\geq 90\%$ polarization. All the experiments were repeated few times to have confidence in the obtained results. The coincidence time window in the experiments was set to ∼6 μs, it can be altered to a smaller window of ∼3 μs in order to further improve the signal to noise ratio.

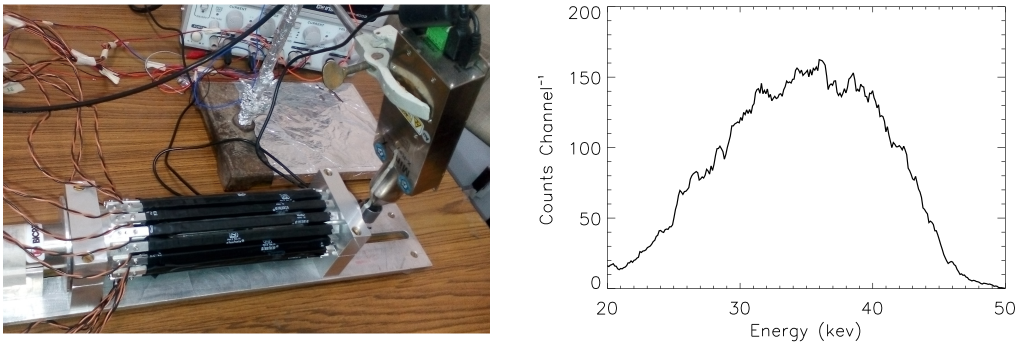

Figure 3.21: Left: polarization experiment with CXPOL using continuum radiation from X-ray gun. Right : Spectrum of the polarized 90° scattered radiation of the gun as taken from CdTe detector

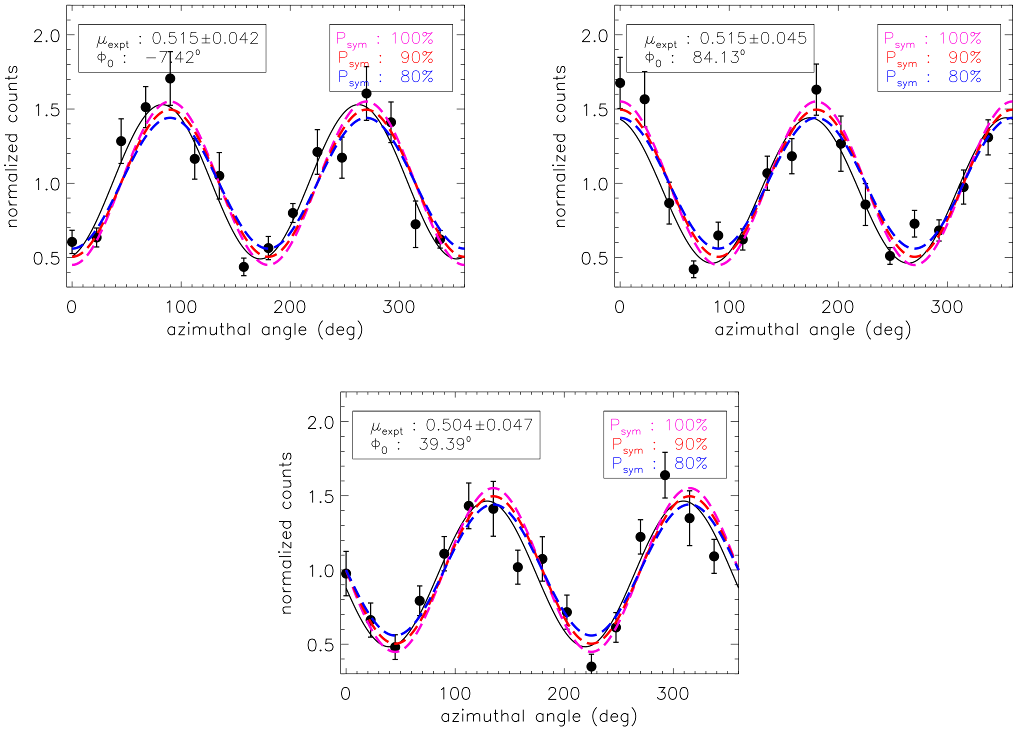

Figure 3.22: Azimuthal angle distribution for partially polarized 20−50 keV continuum radiation for 0° (top left), 90° (top right), and 45° (bottom) polarization angles. The black solid line is the fit to the experimental data. The pink, red and blue dashed lines represent the modulation curves obtained from simulation for this setup for 100, 90 and 80% polarized beams respectively

3.7 Discussions and Future Plans

The main highlights and importance of the experimental results are discussed below.

- SiPMs have been successfully implemented to read out CsI(Tl) absorbers for the Compton polarimeter, which helps in designing a compact and optimized polarimeter geometry.

- Proper choice of scintillator is extremely important in case of SiPM readout to have better polarimetric sensitivity. We showed that for CsI(Tl) scintillators viewed by a single SiPM, detection probability degrades significantly at a distance of 5−6 cm from SiPM at energies ∼50 keV. This is mainly due to longer scintillation time constant of CsI(Tl) scintillator as a result of which photons reaching SiPM simultaneously are less in number and therefore pulse amplitude is low. However, with $CeBr_3$, $LaBr_3$(Ce), NaI(Tl), or other new generation scintillators, which has comparatively smaller decay time constant and at the same time similar or even higher light output, much better performance is expected.

- Choice of appropriate SiPM is also crucial to achieve better sensitivity at low energies. For lower threshold of the scintillators, SiPMs with less background (with similar active area) will be useful. Here we used SiPMs procured from KETEK, which has typical background level of ≤ 500 kHz/mm^2. The new generation SiPMs are supposed to have comparatively much lower background. Recovery time of the micro-pixels after avalanche is also much smaller. These are the key factors to obtain a lower energy threshold of 20 keV or less for the Compton polarimeter. We plan to investigate the sensitivity of $CeBr_3$ and NaI(Tl) scintillators coupled to these new generation SiPMs in near future for the next version of the polarimeter. Coupling between the scintillator and SiPM is also a key factor for better performance of the scintillators. We plan for an optimized enclosure for the SiPM and scintillator which may lead to a better coupling between them and hence an improved threshold.

- With proper choice of scintillators and optimized scintillator-SiPM coupling, new generation SiPMs can be successfully used for lower energy detections ∼20 keV. This is encouraging as one can now think of new polarimetric configurations with SiPM in order to have simultaneous polarimetric and spectroscopic information.

  Use of two SiPMs at two ends of a scintillator will not only optimize the system for better energy threshold but will also give position of interaction from ratio of pulse heights. In that case, use of a Si detector in place of the central plastic scatterer will make the instrument sensitive for Compton spectroscopy in $20 - 80$ keV apart from the high resolution spectroscopy up to ∼40 keV from Si alone. However, the polarimetric performance of the instrument will be compromised because of lower scattering efficiency of Si. On the other hand, with the use of a 5 mm thick plastic (viewed by SiPM array) below the SDD, it is possible to greatly improve the polarimetric performance of the system [100].

Another possible configuration is to use a central scatterer made of segmented plastics with each segment viewed by a SiPM and an array of scintillators with two sided SiPM readout. Such a configuration will optimize the instrument for polarimetry and Compton spectroscopy in $20 - 80$ keV. The overall energy resolution of the system would be limited by resolution of the absorbers and uncertainties in constraining the positions of interactions. However, compared to the Si scatterer configuration, the disadvantage of this configuration is the infeasibility of photoelectric spectroscopy at lower energies.

3.8 Summary

We are developing a proof of concept laboratory model of a hard X-ray focal plane Compton polarimeter, as a foundation for a future proposal of a dedicated hard X-ray polarimetry mission. The main objective here is to demonstrate a mature readiness level of a robust polarimeter configuration and to obtain firm estimates of the resources requirements (in terms of size, weight, power etc) for the future space experiment. In this chapter, we demonstrated the characteristics of the plastic scatterer, specifically at the lower energy depositions. We find that detection efficiency of the plastic is 100% for energy depositions greater than ~7 keV, and gradually decreases for lower energy deposition. In the final experimental configuration of the Compton polarimeter, 16 CsI(Tl)-SiPM systems have been used to record the azimuthal angle distribution. We characterized each of the CsI(Tl)-SiPM systems and finally successfully assembled full polarimeter configuration and test it with both unpolarized as well as partially polarized X-rays. The results presented here are expected to be very useful for designing of future Compton polarimetry experiments with SiPM scintillator read out systems.

While this is only a first version of the proposed polarimeter configuration, we could identify few issues with the initial design, which we plan to rectify in the subsequent versions.

Chapter 4

Prospects of Hard X-ray Polarimetry with Astrosat-CZTI

In last two chapters, we described the development of an optimized hard X-ray Compton polarimeter at the focal plane of a hard X-ray telescope. Whereas such an approach is expected to magnify the polarimetric sensitivity of the instruments by a significant margin in hard X-rays, there is another approach to extract polarization information from instruments, not optimized for polarimetry applications, but could be sensitive to it. In this chapter, we describe the prospects of hard X-ray polarimetry for one such instruments, Cadmium-Zinc-Telluride Imager (CZTI) on board Astrosat [88,89], Indian multi-wavelength astronomy mission, launched on September 28, 2015. Exploring the possibility of polarization measurements from CZTI or other similar instruments is particularly important in the context that there is not a single approved dedicated polarimetry mission in coming years.

In the last decade or so, there have been many proposed missions as well as balloon borne experiments [64,65,68,95,112–114], with some of them being considered at an advanced stage of selection [115]. With the growing realization that a dedicated polarimetry mission would provide quite fresh results, a dedicated X-ray polarimetry mission GEMS [66] was selected for development as part of the NASA Small Explorer program in 2009, but was discontinued in 2012 due to programmatic reasons. It has been proposed again at the 2014 SMEX NASA call, which has also attracted two more proposals dedicated to X-ray polarimetry, indicating enhanced interest of community in having firm X-ray polarization measurements. Still, in the absence of any approved dedicated polarimetry mission, it is very important to explore any possibility of obtaining meaningful X-ray polarization measurements from instruments designed for other related purposes (like X-ray timing and spectroscopy) and to have a robust ground based calibration.

There have been many attempts to retrieve polarimetric information from the existing X-ray instruments having notional polarimetric sensitivity, the noted results being measurement of highly polarized emission from a GRB with the RHESSI mission and from two Galactic X-ray sources (Cygnus X-1, a black hole binary and Crab, a pulsar wind nebula) with the IBIS and the SPI instruments onboard the INTEGRAL mission [15–17, 80]. These measurements, however, faced some criticism because these instruments are not fully optimized for polarimetry and particularly because their polarimetric capabilities were not calibrated before launch [28, 86]. Despite limited polarimetric sensitivity of these instruments, the polarization measurements still provide significant insights into the hard X-ray emission processes in those sources. Therefore, besides attempting for optimized polarization experiments, it is equally important to explore the feasibility of X-ray polarization measurements from non-optimized spectroscopic instruments whenever possible.

CZTI on board Astrosat (see Fig. 4.1), which is primarily designed for hard X-ray imaging and spectroscopy, is one such instrument expected to be sensitive to polarization of the incident X-rays due to its large pixelated detector plane. CZTI is a coded aperture mask telescope with a total active area of 1024 cm^2. The detector plane consists of 64 detector modules arranged in four identical quadrants, each having 16 modules arranged in a square geometry. Each module is an independent CZT (Cadmium-Zinc-Telluride) detector with a 16×16 array of pixels, each of size 2.5 mm×2.5 mm. The 5 mm detector thickness provides detection efficiency at energies higher than the primary spectroscopic energy range of $10 - 100$ keV, where significant fraction of photon interaction is by means of Compton scattering. In such events, the Compton scattered photon could

Figure 4.1: The assembled CZTI payload onboard Astrosat

be detected in an adjacent pixel. Since the direction of the scattered photon depends on the polarization direction of the incident photon, such pixelated detectors can in general, and Astrosat-CZTI in particular, be used as a Compton X-ray polarimeter. In this chapter, with experimental and simulation studies, we show that the Cadmium-Zinc-Telluride Imager (CZTI) on board the forthcoming Indian astronomy mission Astrosat will be capable of measuring polarization of the incident X-rays in the energy range $100 - 300$ keV. In the next section, we discuss basic principle of X-ray polarimetry with CZTI. Following this, we discuss the overall polarimetric sensitivity of CZTI with polarimetric background in Sec. 4.4. Sec. 4.5 discusses the polarization experiment with CZTI and the results demonstrating the polarimetric capability of CZTI. Finally, the astrophysical significance of the polarimetric capability of CZTI is described in Sec. 4.6 before concluding in Sec. 4.7.

4.1 Compton Polarimetry with Pixelated Detectors

When a polarized beam of X-ray photons is Compton scattered, it is preferentially scattered perpendicular to the direction of polarization, giving rise to a modulation in the azimuthal angle with a $\cos^2 \phi$ variation with the modulation amplitude directly proportional to polarization fraction of the incident beam. Compton polarimetry with pixelated detectors works on the same principle. Here the double pixel events arising from the Compton scattering of a photon in one pixel and absorption of the scattered photon in another pixel constitute the basic polarization event. The azimuthal angle of the Compton scattering is determined from the direction of center of the scattering pixel to the center of the absorbing pixel with reference to a pre-defined instrument reference plane. The histogram of the azimuthal angle distribution can then be used to determine the modulation factor and polarization angle as usual. It is to be noted that in case of pixelated detectors, the azimuthal angle bins are unequal which leads to an inherent modulation pattern in the azimuthal angle distribution. Thus the observed modulation pattern has to be normalized using the similar modulation pattern for unpolarized beam as discussed later.

Astrosat-CZTI consists of an array of pixelated CZT detectors with pixel size of 2.5 mm (see Fig. 4.2). Timing resolution of CZTI being 20 μs, simultaneous events can be determined with minimum of 20 μs time window. As the CZT detectors with 5 mm thickness has significant Compton scattering efficiency at energies > 100 keV, it is expected that Astrosat-CZTI can provide useful polarization measurement at energies even beyond its primary energy range. Though this configuration of CZTI in principle should be capable of polarization mea-

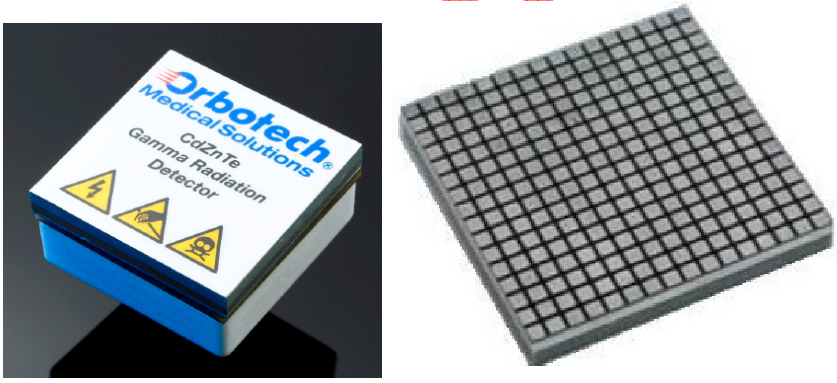

Figure 4.2: Left: A single CZTI module procured from Orbotech Medical Solutions. Dimension of the module is 40 mm × 40 mm. Thickness is 5 mm. Right: CZTI module is pixelated into an array of 16 × 16 pixels, therefore pixel size of 2.5 mm

surement, feasibility of Compton polarimetry with CZTI depends on many other factors, namely,

- whether the Orbotech CZTI modules have multi-pixel detection capability or not,
- if the modules do have multi-pixel detection capability then whether CZTI will have any meaningful polarimetric sensitivity,
- finally, whether the polarimetric information is preserved by the onboard data processing.

We experimentally verified the multi-pixel detection capability of the CZTI modules and carried out detailed Geant−4 simulation for such pixelated CZT detectors to estimate the polarimetric sensitivity of Astrosat-CZTI. We also carried out polarization experiments to verify the capability of the CZTI processing electronics to preserve the polarimetric information, which are discussed in the following sections.

4.2 Multi-pixel Detection Capability of CZTI Detector Modules

4.2.1 Experiment setup

In order to verify multi-pixel capability of CZTI modules, we conducted an experiment in which 1 CZTI module was illuminated with a partially polarized beam of energy ∼100 keV.

The experiment setup is shown in Fig. 4.3. Polarized beam of 100 keV photons was produced by Compton scattering of 122 keV line of ^{57}Co from a plastic scatterer constraining the angle of scattering at 90°. Scatterer, placed in front of ^{57}Co is 6 cm in length. Both the plastic scatterer and source are kept inside a thick lead (thickness 2 cm) cylinder with a narrow slit of dimension 5 cm × 5 mm. CZTI module was kept at angle 90° with respect to the axis of cylinder

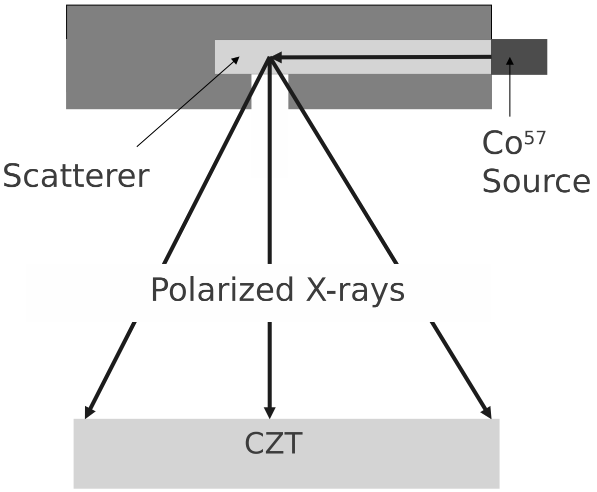

Figure 4.3: Schematic diagram of the experiment setup. 122 keV photons from ^{57}Co are scattered at 90° by a plastic scatterer and interact with CZTI module

as shown in Fig. 4.3. Alignment of the slit and the CZTI module was carefully done from the pixel image of the module.

Since, radioactivity is a random phenomenon, time interval between two successive independent events recorded in CZTI module can be modelled by Poisson's statistics. However, Compton scattering of an incident photon results in multiple interactions due to the deposited energies in Compton scattering and subsequent absorption of the scattered photon, either in the same pixel or separate pixels. These events, being correlated to each other, should deviate from the modelled Poisson's distributed time intervals.

4.2.2 Data analysis and results

Fig. 4.4 shows the histogram of time intervals between two successive events. There is clearly an excess of events with time interval below 40 μs beyond which the ΔT distribution agrees nicely with the Poisson's distribution. Each event has an individual time stamp with a resolution of 20 μs. Any two events recorded within duration of 20 μs will have the same time stamp. Therefore the genuine multi-pixel events i.e. those resulting from the Compton scattering or escape events in the photoelectric interaction should occur in the same time bin of 20 μs. We observe significant excess in the second time bin (events occurring between

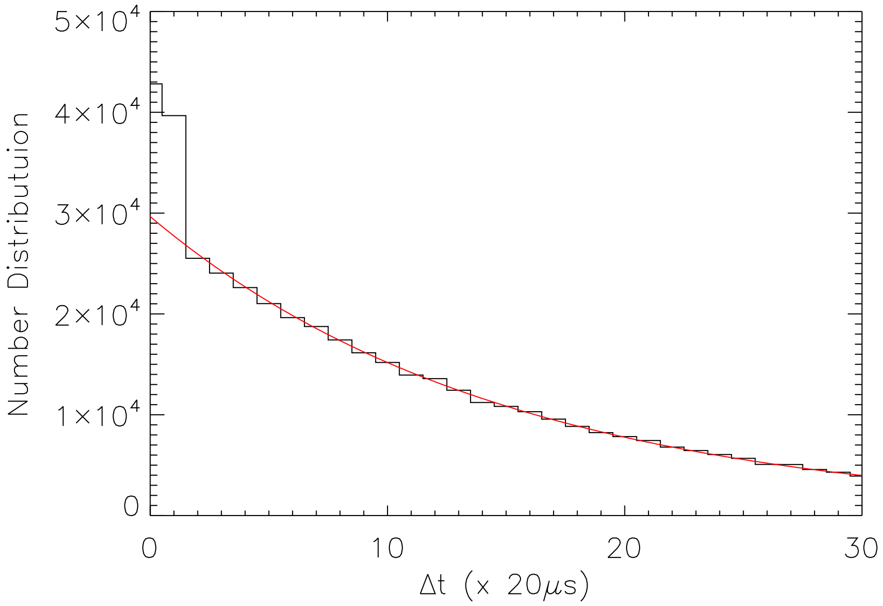

Figure 4.4: Distribution of time intervals of all successive events recorded in CZTI module in ^{57}Co experiment. There is an excess of events for time interval below 40 μs. The events beyond 40 μs time interval have been fit with a Poisson's function shown by solid red line

20 μs to 40 μs), however, this is due to the specific read-out logic implemented in the CZTI and is well understood. The detector modules can detect multi-pixel events and store them internally. The time stamp to each event is assigned after being read-out. Since the read-out logic is configured to read event from one module at a time, it is quite possible that two simultaneous events in different pixel of a given module may get two consecutive time stamps, which results in excess events in the second bin of the ΔT distribution. Thus, we believe that a large fraction of the excess events recorded within 40 μs are true simultaneous events. We have repeated the same experiment with other modules and found similar results. This clearly shows that the CZTI modules do have capability to detect and record multiple simultaneous events.

It should be noted that 40 μs is significantly large duration for being considered as simultaneous and thus could result in many chance coincidence events. In fact, we do observe successive events in the same pixel with two consecutive time stamps which are clearly chance events. In order to properly identify such chance

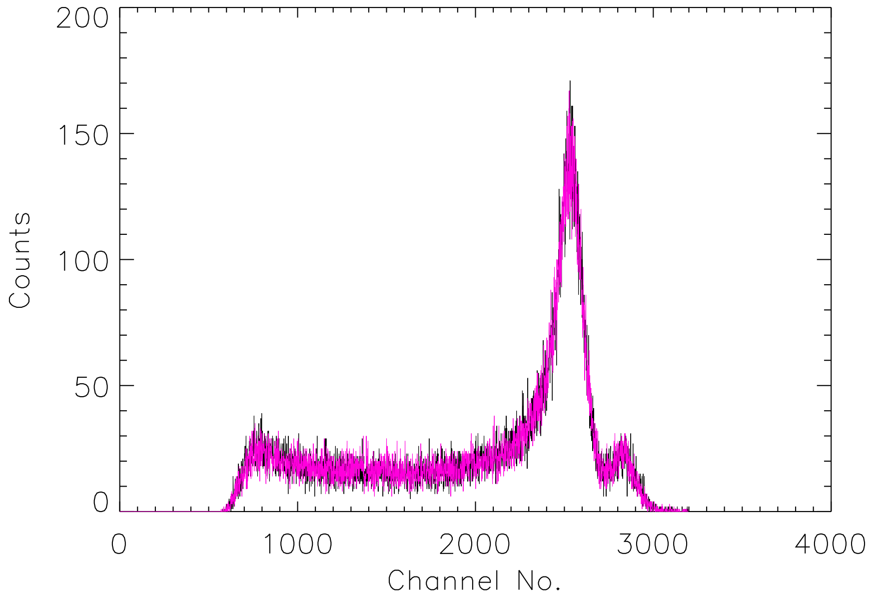

Figure 4.5: Spectra obtained for all double pixel events from ^{57}Co experiment. Black and red refer to two pool of pixels. For details, refer to text

events and ignore them, we check time stamps of up to five events at a time (we start with one event and compared the time stamp, t_i, of that event with time stamps of next subsequent events, t_{i+1}, t_{i+2}.., until the difference in time arrival is > 40 μs) and list all double, triple or more pixel events. We do find a small fraction of three (or even four) pixel events occurring within 40 μs, however all such events are ignored and only double pixel events are considered for further analysis. Fig. 4.5 shows the spectra for the valid double pixel events. Each valid event involves two pixels; in case of Compton scattering, the pixel with less deposited energy is the primary pixel and the other one is the secondary pixel. However, since the module is illuminated uniformly, it is not possible to identify primary and secondary pixels apriori. Hence, channel histogram for both the pixels, denoted by black and red, is shown in Fig. 4.5.

This spectra appears similar to the spectra obtained by the direct exposure of X-rays from ^{57}Co, with both the peaks corresponding to the 122 keV and 136 keV lines clearly visible. This is because of the fact that all double pixel events are dominated by the chance coincidence events, occurring due to relatively large

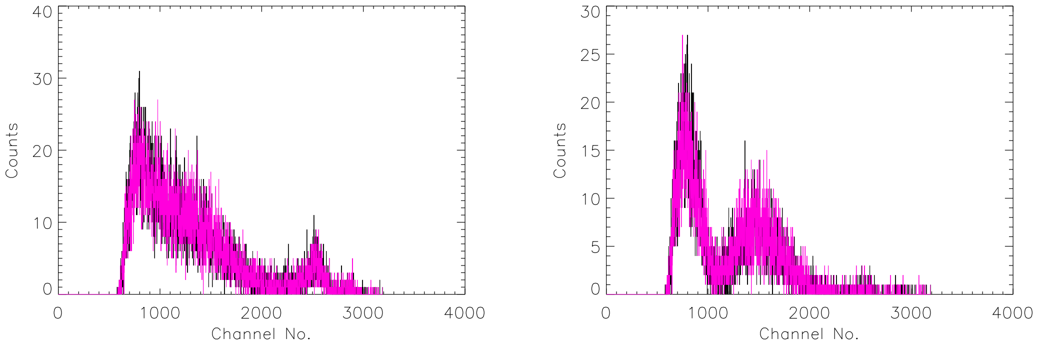

Figure 4.6: Left: Spectra for the neighboring double pixel events. Right: spectra obtained after applying ratio condition (ratio of deposited energies ≥ 2) on the neighboring double pixel events

coincidence window of 40 μs, of widely separated and independent single pixel events. Since the Compton scattered photon is not expected to travel far from the scattering pixel before getting absorbed, we consider double pixel events occurring only within the adjacent pixels to avoid the chance coincidence events. Left plot of Fig. 4.6 shows the spectra of the two pixels for all adjacent double pixel events. It can be seen that majority of chance coincidence events, manifested by the 122 keV and 136 keV peaks, are now absent. However, a small fraction of such events are still present. To prevent even this small fraction of the chance coincidence events, we impose another condition on the ratio of the energy deposited in the two pixels of the adjacent double pixel events. For a true Compton scattering event, energy of the scattered photon is always greater than the recoil electron energy for incident photon energies < 280 keV, even for maximum scattering angles. For lower energy of the incident photons and scattering angles around 90°, the ratio of the energy of the scattered photon and the recoil electron is ≥ 2. Therefore, we consider only those adjacent double pixel events which satisfy this condition. Right plot of Fig. 4.6 shows spectra of both pixels after applying the ratio condition. This is the graphical representation of the multi-pixel detection capability of the CZTI modules. It can be seen that the ratio condition is also helpful in rejecting other chance events arising from the electronic noise. The first peak in the spectra corresponds to the primary Compton scattering pixels and the second peak corresponds to the absorption of the scattered photons.

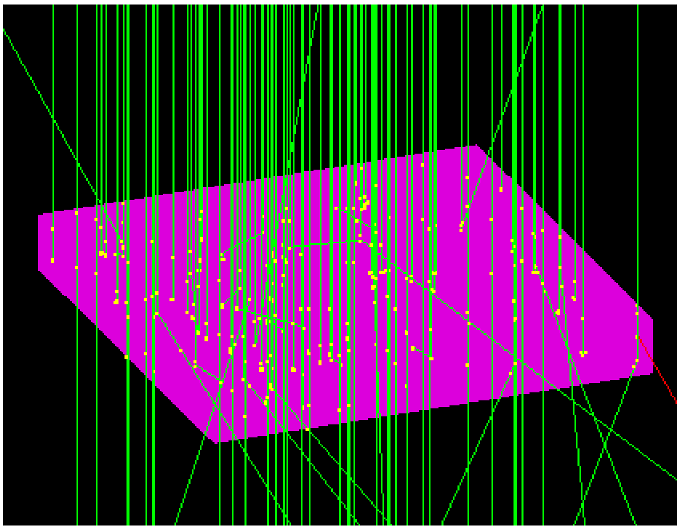

Figure 4.7: Simulated diagram for a CZT module (40 mm × 40 mm × 5mm). The module is made to shine uniformly by X-ray photons shown in green

It should be noted, however, that these events may not be pure Compton scattering events as the escape photons from CZT can also mimic the Compton scattering and hence the same distribution is also possible for the double pixel events arising from the detection of the escape photons. In order to estimate the fraction of such events and estimate polarimetric sensitivity of CZTI, we carried out detailed Geant−4 simulation as described in the following section.

4.3 Geant−4 Simulation

We used Geant−4 toolkit [96] to estimate modulation factor and efficiency of a single CZTI module for 100% polarized beam. CZTI module's electronics ULD is around 250 keV. For a 5 mm thick CZT, probability of Compton scattering becomes significant beyond 100 keV. So, simulation was done for mono-energetic 100% polarized and unpolarized beams in the energy range of 100 keV to 300 keV, employing low energy electromagnetic processes e.g. *G4LowEnPolarizedPhotoElectric*, *G4LowEnPolarizedRayleigh*, *G4LowEnPolarizedCompton*, *G4LowEnBremss* and *G4LowEnIonization*. The incident beam of photons was generated using General Particle Source (GPS) which was perpendicularly incident on a single CZT block (40 mm × 40 mm × 5mm) as shown in Fig. 4.7. For each energy, we carried out simulation for 10 million photons incident on CZT uniformly across its surface and for each energy, the polarization angle was varied from 0° to 90° at a step of 11.25°. For each photon, maximum of 7 secondary photon interaction positions and corresponding deposited energies were recorded. Deposited energy for each of such interactions is calculated by summing up the individual energies of all the secondary electrons generated in that interaction. We ignore the electron track lengths and assume that total energy of the secondary electron is deposited at the location of the photon interaction. Output is kept in the form of an event list with different types of interactions, positions of interactions (maximum 7), energy deposited in each interaction etc.

4.3.1 Estimation of polarimetric efficiency

Further data analysis was done using IDL (Interactive Data Language). Since pixel size of Astrosat-CZTI modules is 2.5 mm, the interaction positions in the event list are pixelated with 2.5 mm spacing. For multiple photon interactions occurring within the boundary of a single pixel, energies deposited in these interactions are added together to get the total energy deposition in the given pixel. In this way, we divide all events in single pixel, double pixel, three pixel up to maximum 7 pixel events. Fig. 4.8 shows the probabilities of the single, double and multiple pixel (≥ 3) events as a function of incident photon energies. As only the double pixel events are useful for the polarization measurement, further analysis is carried out only for the double pixel events. Fig. 4.9 shows the probability of different types of interactions giving rise to the double pixel events. We see that apart from the valid Compton scattering events (1 Compton and 1 photoelectric) providing the polarimetric information, there are many other types of double pixel events which may contaminate the azimuthal distribution of the real Compton scattering events and blur the polarization signature embedded in the incident beam. Pure photoelectric events (shown in blue) are because of detection of an incident photon in one pixel due to photoelectric absorption and detection of the consequent escape photon (∼30 keV) in another pixel. Probability of these events is quite significant (∼1%). On the other hand, a photoelectric absorption

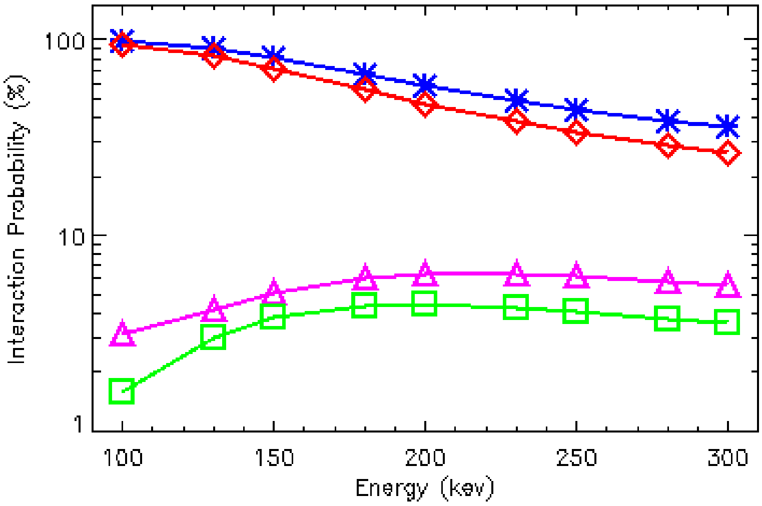

Figure 4.8: Probability of single pixel (red, diamond), double pixel (pink, triangle) and more than double pixel events (green, square) as a function of photon energies for 2.5 mm pixel size. Total interaction probability for 5 mm thick CZT is shown in blue (asterisks)

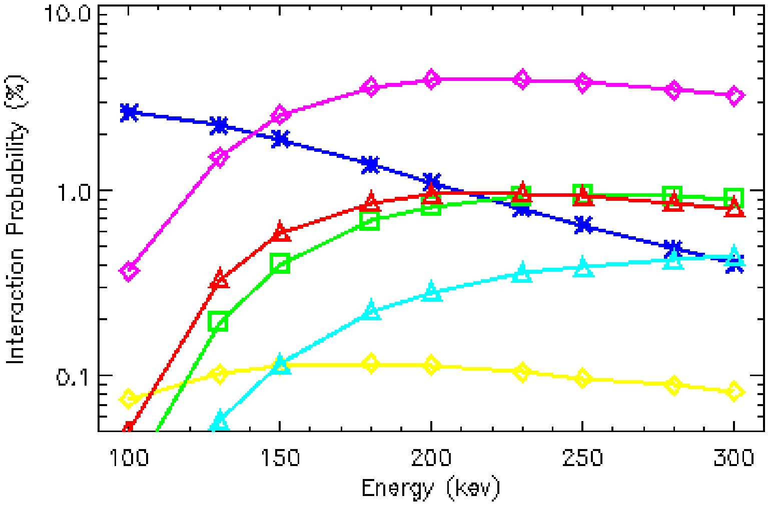

Figure 4.9: Different processes generating double pixel events: photo-photo (blue, asterisks), 1compt-photo (pink, diamond), 1compt-1photo (red, triangle), photo-multi compt (green, square), photo-brem (yellow, diamond), photo-brem-compt (light blue, triangle)

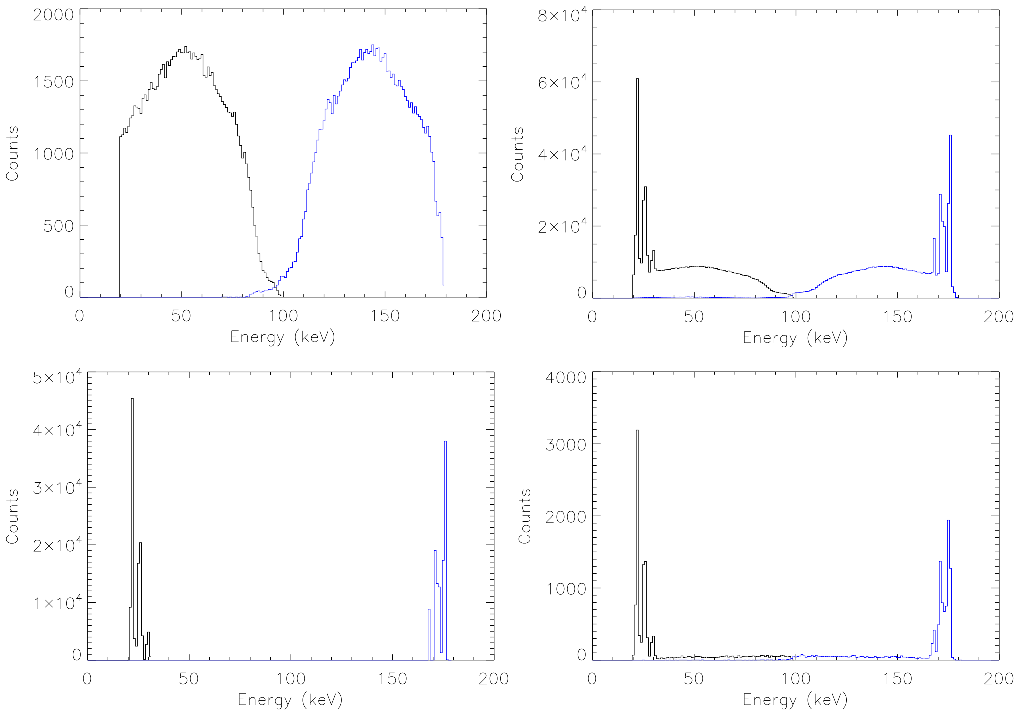

Figure 4.10: Spectra obtained from simulation of 200 keV beam. Black and blue refer to primary and secondary pixels respectively. Top-left: ideal Compton events; Top-right: all double pixel events; Bottom-left: photoelectric escape events; Bottom-right: photoelectric-bremsstrahlung events

may lead to bremsstrahlung photons from the ejected electron, detection of which may trigger double pixel events (shown in yellow and light blue). All these events may mimic the true Compton scattering events and jeopardise the polarization signature in the beam.

To obtain spectra for these double pixel events, we assumed the pixel with lower energy deposition to be the primary pixel i.e. where the Compton scattering takes place and the pixel with higher energy deposition to be the secondary pixel in which the scattered photon is absorbed. This assumption holds good for incident photons with energies up to 280 keV. Representative spectra of true Compton events and other double pixel events for the incident photons of 200 keV are shown in Fig. 4.10. Spectra shown in black and blue are for primary and secondary pixels respectively. Spectra for pure photoelectric events shows two peaks at lower and higher energies due to escape photons. The upper left panel shows spectra of double pixel events of ideal Compton events and the upper right

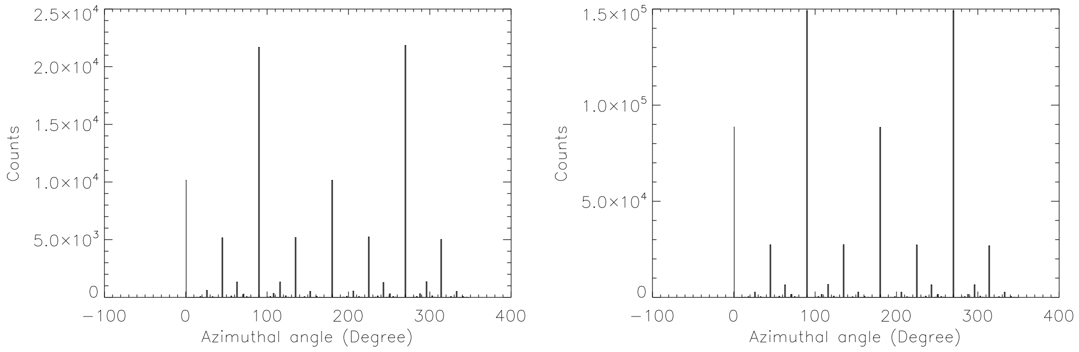

Figure 4.11: Azimuthal angle distribution for 200 keV beam with polarization angle of 0°. Left: ideal Compton events. Right: all double pixel events with 20 keV threshold

panel shows spectra of all double pixels events with minimum energy deposition above the detection threshold (20 keV) i.e. without any selection on interaction type. The bottom panels show spectra for only photoelectric escape events (left) and photoelectric+bremsstrahlung events (right). It should be noted that these are the spectra of only deposited energy in the pixels and are not convolved for the CZT detector response.

4.3.2 Estimation of modulation factor

Using pixel map for the double pixel events, we obtained the azimuthal angle for each of the events. Representative azimuthal distribution corresponding to the incident photon energy of 200 keV and polarization angle of 0° are shown in Fig. 4.11, where the top panel shows the azimuthal angle distribution for ideal Compton events (1 Compton and 1 photoelectric) and the bottom panel shows the same for all double pixel events with 20 keV threshold in the CZTI module. It is to be noted that azimuthal angle distribution has an inherent modulation pattern due to the unequal bin size with respect to the primary pixel i.e. the azimuthal angle covered by the edge pixels is much larger than that for corner pixels and hence more number of photons are detected in edge pixels. Since the polarization direction is parallel to the direction of edge pixels, the counts in the edge pixels are modulated whereas for corner pixels have the same average

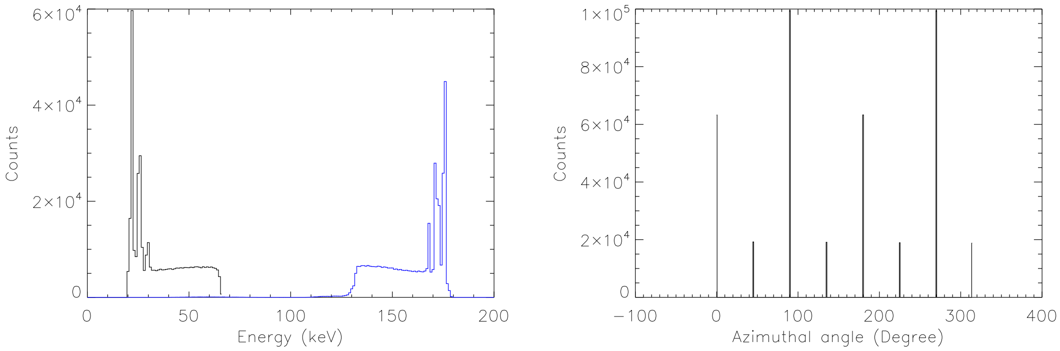

Figure 4.12: Spectra (left) and azimuthal angle distribution (right) obtained from simulation of 200 keV beam (polarization angle of 0°) considering the adjacent double pixel events including the criteria of ratio of deposited energies greater than 2

number of counts. Modulation factor in this case (0° polarization angle) can be estimated from the events corresponding to 0° and 90° bins or 180° and 270° bins. Estimated modulation factor for the ideal Compton events is, $\mu = 0.36$, whereas for all the double pixel events it is, $\mu = 0.25$. The modulation factor for all events is clearly degraded compared to the true Compton events due to the false events arising because of photoelectric and bremsstrahlung interactions.

In the previous section, we discussed two conditions derived from the experimental data i.e. considering only adjacent pixel events and ratio of scattered to deposited energy ≥ 2. In order to get realistic estimate of the modulation factor from the simulated data, we apply the same conditions to the simulated double pixel events without using the knowledge of the underlaying interactions. Fig. 4.12 shows the spectra and azimuthal angle distribution for the double pixel events on the basis of these conditions.

It can be seen that the modulation factor after applying these two conditions, $\mu = 0.23$, has slightly degraded from the original modulation factor obtained by including all events into calculation. This is because of the second condition of ratio of energy deposited in two pixels to be $\geq$2, which actually rejects some valid Compton events where the scattering angle is greater than ∼120° as shown in Fig. 4.13.

This in turn introduces asymmetry in the range of scattering angle around 90° and thus the effective modulation degrades. Another negative effect of these

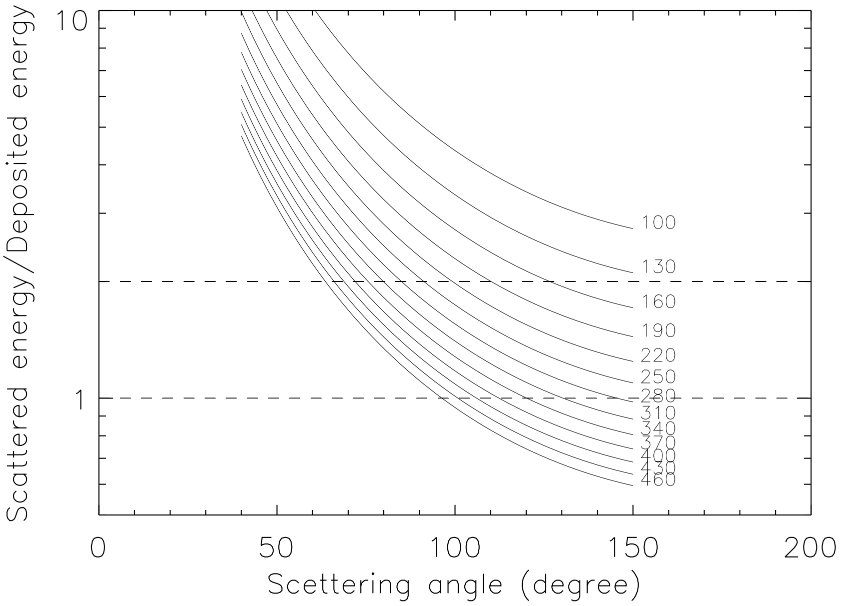

Figure 4.13: Ratio of Compton scattered photon energy to electron recoil energy as a function of scattering angle and incident photon energies. The photon energies mentioned in the plot are in keV unit

conditions is to reduce the detection efficiency of the Compton events. However, both these conditions are essential in order to reduce other noisy events, as shown by the experimental data and hence the expected sensitivity is estimated using all these conditions.

It is to be noted that the overall degradation in modulation factor is mainly because of the escape photons which may be avoided by applying energy threshold of 35 keV in both primary and secondary pixels. With this condition the modulation factor increases from 23% to 41% at 200 keV for polarization angle of 0°. However, this condition restricts the lower energy detection limit of polarization to be around 150 keV (see Fig. 4.14), thereby reducing the overall polarimetric sensitivity of the instrument.

As mentioned earlier, the azimuthal bins are asymmetric for the pixelated detectors and hence the azimuthal distribution has inherent modulation pattern. This inherent modulation pattern can be corrected by normalizing the azimuthal distribution with respect to the azimuthal distribution for unpolarized beam at the same energy (or energy range) [19, 21]. If $N_{i,pol}$ is the number of counts

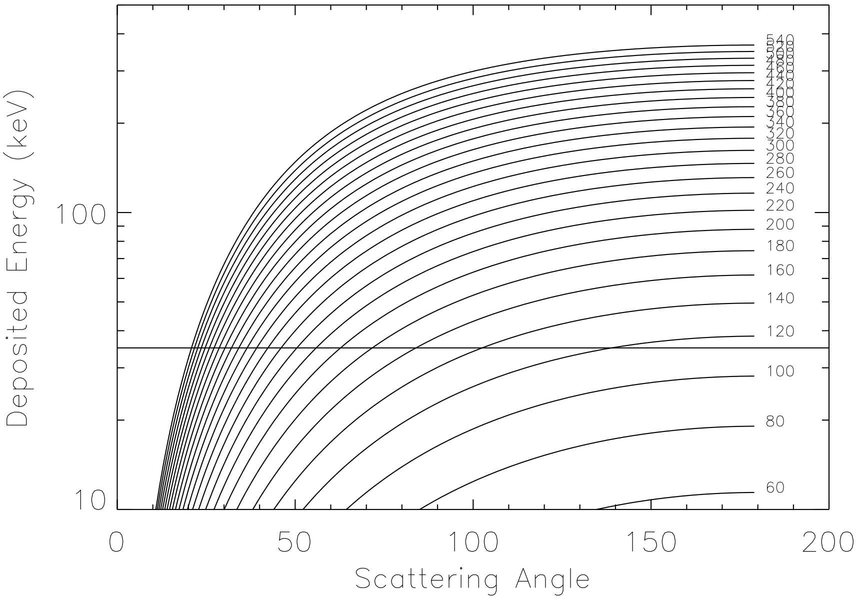

Figure 4.14: Deposited energy in Compton scattering as a function of scattering angle and incident photon energies. The incident photon energies for each line mentioned in the plot are in keV unit. For incident energies greater than 140 keV, deposited energy is greater than 35 keV

in i^{th} bin for 100% polarized beam and $M_{i,unpol}$ is the counts in that bin for 100% unpolarized beam with average number of counts in each bin $\overline{M}_{unpol}$, then normalized counts in i^{th} bin will be

$$N_{i,corrected} = \frac{N_{i,pol}}{M_{i,unpol}} \overline{M}_{unpol}. \tag{4.1}$$

Fig. 4.15 shows the modulation curves at 200 keV for different polarization angles after correcting for the geometry using Eq. 4.1. The modulation curve is fitted by $cos^2\phi$ function and the fitting parameters are used to estimate the modulation factor. There are few points to be noted - 1) Modulation factor does not depend on geometric correction. 2) Modulation factor is higher for 45° polarization angle because, photons are restricted to be scattered close to 90° because of the geometry. 3) Modulation factor is polarization angle dependent which implies that the sensitivity of the instrument too will depend on the angle of polarization of the beam with respect to the instrument reference plane. It is obvious that in real life situation, the plane of polarization of the incident X-rays will

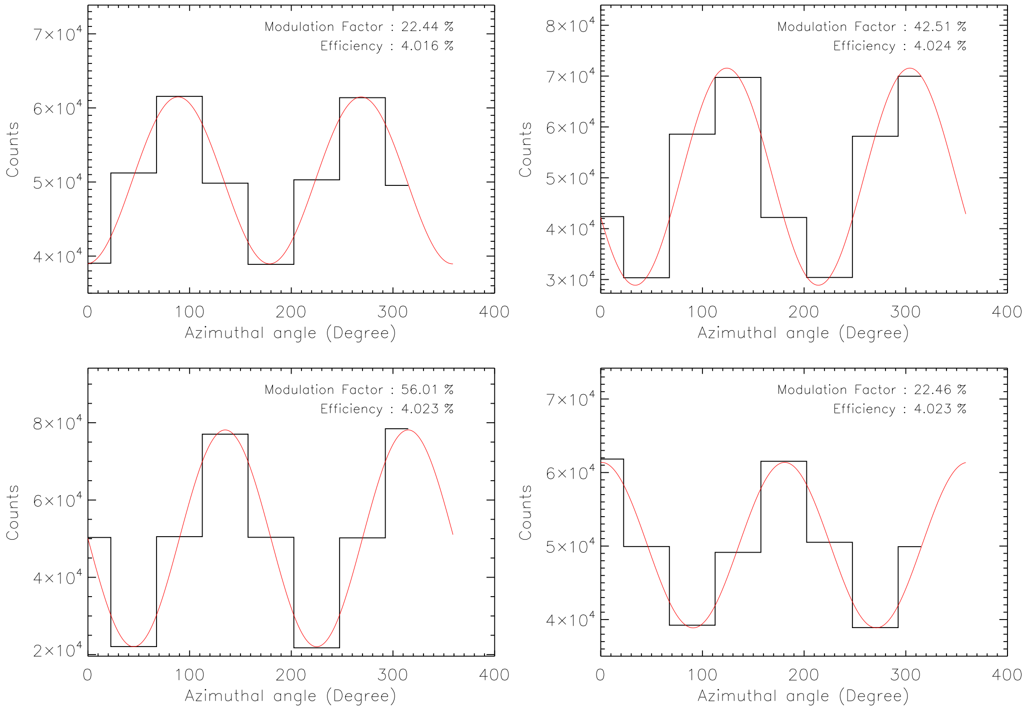

Figure 4.15: Modulation curves at 200 keV for polarization angles (from upper left to lower right) of 0°, 22.5°, 45° and 90°. The modulation curves are fitted by the red solid lines. Modulation factors and efficiencies for different polarization angles have been mentioned in the respective plots

not be known. Therefore, the dependence of polarization measurement on the incident polarization angle means that X-ray polarization for any celestial source measured by Astrosat-CZTI must be verified at different instrument angles with reference to the measured polarization angle. This can be achieved either by the rotation of the spacecraft with respect to the source direction or by observing the same source at different time which may have different spacecraft position with respect to the source. Another important point to note is that the geometric correction in the raw azimuthal angle distribution introduces an additional statistical uncertainty in the modulation factor. As the azimuthal angle distribution of the unpolarized photons can be estimated very accurately, the uncertainty in the corrected modulation factor is determined mainly from the statistical uncertainty of the observed azimuthal angle distribution. For sufficiently large number of unpolarized photons ($\sim10^9$), we find that the uncertainty introduced by the correction is less than 0.3%. However, this additional uncertainty in modulation factor should be carefully taken into account because it sets the lower limit for the overall uncertainty in the measured polarization for any unknown beam.

Fig. 4.16 shows the angle dependent modulation factors and detection efficiency as a function of incident photon energy. It can be seen that the modulation

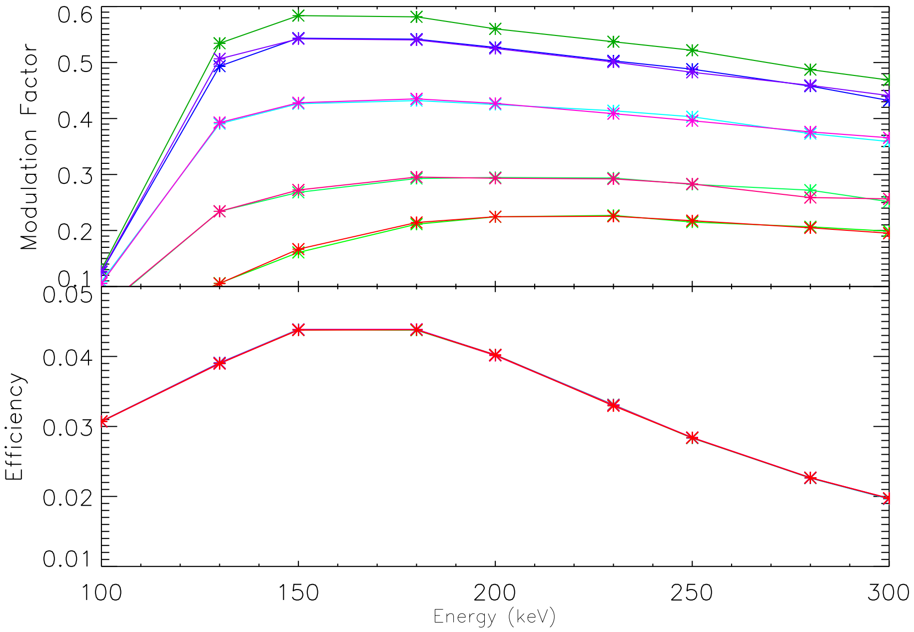

Figure 4.16: Modulation factor and efficiency (for 100% polarized beam) as a function of photon energy and polarization angle. Different polarization angles are denoted by different colors. In the modulation factor vs. energy plot, the curve at the top corresponds to 45° polarization angle. It is followed by 33.75° and 56.25°, 22.5° and 67.5°, 11.25° and 78.75° and 0° and 90° polarization angles respectively. Polarimetric efficiency is independent of polarization angle

factor is maximum for 45° and minimum for 0° and 90°. Since scattering geometry is symmetric with respect to the polarization angles 0° and 90°, 11.25° and 78.75° so on, modulation factor is same at these polarization angles. Probability of photoelectric interaction being higher at lower energies, modulation factor is lower at those energies due to the dominance of the escape photons, compared to that at higher energies. Overall detection efficiency in the energy range of 100 to 300 keV is of the order of 3% and does not depend on the polarization angle as expected.

4.4 Polarimetric Sensitivity of CZTI

Estimation of MDP for Astrosat-CZTI require accurate knowledge of μ_{100} - the modulation factor for 100% polarized X-rays, R$_{bkg}$ - background count rate and R$_{src}$ - source count rate, which in turn requires the knowledge of polarimetric detector efficiency in the energy range of interest. The modulation factor and the polarimetric detector efficiency are already determined from the Geant$-$4 simulations (Fig. 4.16) in the energy range of 100 keV to 300 keV. The other quantities can be estimated as described in the following subsections.

4.4.1 Source count rate

Source count rate (R$_{src}$) can be estimated directly by integrating the source spectrum, which we assume to be Crab like for the present estimation over the effective collecting area of CZTI. As mentioned earlier, the polarimetric energy range of CZTI is beyond the primary spectroscopic energy range. Therefore the coded mask and other support structure of CZTI has significant transparency at those energies. Thus for an on-axis source, we estimate the total source count rate for the two cases - one for the open area of 512 cm^2 (50% unobscured area of the coded mask) by integrating the source spectrum convolved with the polarimetric efficiency, and second for the area of 512 cm^2 shadowed by the partly transparent coded mask by integrating the source spectrum convolved with both the polarimetric efficiency and the transmission probability of the mask (made of 0.5 mm thick Tantalum). Following this method, the total count rate for the Crab is found to be 1.0006 $cnt\ s^{-1}$ in the energy range of 100 keV to 300 keV over the entire detector plane of the CZTI.

4.4.2 Background estimation

Estimation of background (R$_{bkg}$) for Astrosat-CZTI is more involved process. It should be noted that the polarimetric background of interest here is only the spurious double pixel events satisfying the filtering conditions mentioned in the previous section. Such spurious double pixel events can arise either from the chance coincidence of the usual spectroscopic background i.e. the instrumental background and the cosmic X-ray background (CXB) or these can also arise from the actual Compton scattering of the CXB photons. In either case, it is necessary to first estimate the spectroscopic background rate due to the cosmic X-ray background.

Cosmic X-ray background

Since Astrosat-CZTI has relatively wide field of view (FOV) of $6^\circ \times 6^\circ$, the cosmic X-ray background (CXB) within the FOV has significant contribution in the total event rate in the detector. However, the most important contribution is from the CXB leaking through the collimators and support structure, because these are designed only up to 150 keV which is the primary spectroscopic energy range of CZTI. We use the hard X-ray spectra of the CXB reported by Turler et al. [98] to calculate both these contributions. The contribution of the CXB within the FOV is calculated using the same method as for the source with detection efficiency of 5 mm CZT and is found to be ∼0.0012 $cnt\ cm^{-2}s^{-1}$ in 100 keV to 300 keV. The contribution of CXB outside the FOV is calculated for two sides of CZTI as the other two sides are shielded by other instruments. Further, this contribution is also expected to be different in different CZTI modules because all modules are collimated by 0.2 mm thick Tantalum wall and hence the inner modules has increased shielding of the collimators of the outer modules. This contribution is calculated using Eq. 4.2.

$$N^{OFF}_{CXB} = \int_{\phi}\int_{\theta>\,6^\circ}\int_{E>\,100keV} I(E)\, A_{eff}\, T(E,\theta,\phi)\, \epsilon(E,\theta)\, d\Omega, \qquad (4.2)$$

where, $I(E)$ is hard CXB spectra [98] in $cm^{-2}s^{-1}sr^{-1}$. $d\Omega = \sin\theta\, d\theta\, d\phi$ is the solid angle. $A_{eff} = A\cos\theta$ is the effective area of the CZTI module. $T(E,\theta,\phi)$ is the transmission probability of Ta collimator(s). Total thickness of Ta, a photon (energy, E) has to pass through to reach a particular module depends on the module position, angle θ and ϕ. $\epsilon(\mathrm{E},\theta)$ is the detection efficiency of CZT at energy E; effective thickness of CZT and thus efficiency of CZT depends on the angle θ. Other support structure made of Aluminum (total thickness of ∼5 mm) is assumed to be fully transparent for this calculation. We estimated the CXB events for all the modules with average value of ∼0.0189 $cnt\ cm^{-2}s^{-1}$ in 100 keV to 300 keV. Thus, the total count rate due to both the CXB within FOV and outside FOV is found to be 0.0201 $cnt\ cm^{-2}s^{-1}$.

Background due to chance coincidence

The chance coincidence can be either between two background events or a background event and source photon or even between two independent source photons. The rate of such spurious chance coincidence events can be estimated from the Poisson's distribution for the total event rate, $N\,cm^{-2}s^{-1}$, in the detector which includes the source count rate, instrumental background rate and the cosmic X-ray background count rate. We estimate total count rate for an on axis source as mentioned earlier, however now using total interaction efficiency of the detector instead of the polarimetric efficiency. Source photons being detected in CZTI will depend on source strength and is found to be ∼0.0322 $cnt\ cm^{-2}s^{-1}$ in 100 keV to 300 keV for 1 Crab source intensity.

The instrumental background generally arises due to the secondary particles generated from the interaction of the high energy cosmic rays with the overall instrument as well as spacecraft material. During normal operation, most of the experimental background is expected to be flagged by anti-coincidence unit and hence rejected. However, for the purpose of calculating chance coincidence, we consider the actual counts detected in the CZT detectors. Accurate estimation of instrumental background typically requires simulation with full mass model of the spacecraft. Here we use an indicative value based on our earlier HEX experiment onboard Chandrayaan-1 mission. This experiment used similar CZT modules and the observed background rate was $2-3$ $cnt\ cm^{-2}s^{-1}$ [116]. Based on this, but considering different space craft structure and orbit for Astrosat, here we assume a very conservative value of ∼10 $cnt\ cm^{-2}s^{-1}$ for the instrumental background.

Based on these considerations, the total event rate, N, in the CZT detector is expected to be ∼10.0523 $cnt\ cm^{-2}s^{-1}$ in 100 keV to 300 keV for 1 Crab source strength (0.0322 $cm^{-2}s^{-1}$ from source, 10.0 $cm^{-2}s^{-1}$ from instrumental background and 0.0201 $cm^{-2}s^{-1}$ from CXB). For this event rate, the total chance coincidence rate i.e. two events occuring within the conicidence time widow, $\Delta T = 40\ \mu s$ in two adjacent pixels can be estimated using Eq. 4.3,

$$R_{bkg}^{chance} = \frac{(N\,a\,\Delta T)^2}{2!} \mathrm{e}^{-N a\,\Delta T} N\,a\ \times\ N_{dbl-pix}\ \times\ 64. \tag{4.3}$$

where 'a' is twice the single pixel area (A_{pix}) and $N_{dbl-pix}$ is the total number of unique combinations of two adjecent pixels for one CZTI module. From the simple geometric considerations $N_{dbl-pix}$ is found to be 926 (i.e. 15 combinations for a single raw and total 16 raws, 15 combinations for single column and total 16 columns similarly for the two diagonal directions). To get chance events for whole detector plane, the factor 64 is multiplied. The estimated chance events is $\sim$9.4055 $\times$ 10^{-5} $cnt\ s^{-1}$. This value is still overestimated as we have not applied the ratio condition in the chance coincidence events. It can be seen that the chance coincidence rate is totally dominated by the instrumental background and despite assuming a very conservative value for the instrumental background, the total chance coincidence rate is extremely small as expected for a Compton polarimeter.

Compton scattering of CXB photons

As mentioned earlier, Compton scattering of the CXB photons constitutes a very important component of the overall polarimetric background. Again here it is necessary to consider both the CXB within the FOV of CZTI and the CXB out of the FOV. The contribution of the CXB photons in the FOV can be calculated with the same method used to estimate the source count rate, R_{src} - i.e. CXB spectra [98] multiplied with polarimetric efficiency and transparency of coded mask for 50% obscured area and CXB spectra multiplied with only polarimetric efficiency for other 50% unobscured area. Total rate of this component is found to be $\sim$0.0347 $cnt\ s^{-1}$ in 100 keV to 300 keV over the entire detector plane. Contribution to the background due to Compton scattering of out of FOV CXB photons can also be estimated Eq. 4.2, however $\epsilon(E, \theta)$ has to be replaced by appropriate polarimetric efficiency for off-axis photons. We extended our Geant$-$4 simulations for off-axis photons with incident angles ranging from 10° to 85° to estimate the efficiency of getting double pixel events satisfying all experimental conditions mentioned in previous sections.

Further, this background will vary from module to module due to varying degree of shielding from the collimators of adjacent modules. The average background is found to be to be ∼1.0053 $cnt\ s^{-1}$. Thus the total background due to Compton scattering of CXB is $R_{bkg}^{CXB} = 1.0400\ cnt\ s^{-1}$ and total background, R_{bkg} $(= R_{bkg}^{chance} + R_{bkg}^{CXB})$, affecting the overall polarimetric sensitivity, is found to be 1.0401 $cnt\ s^{-1}$ in 100 keV to 300 keV over the entire detector plane. Therefore, the total polarimetric background (i.e. total double pixel events passing all the filtering criteria) is almost the same as the total polarimetric count rate from Crab.

Earth's albedo background

So far, in our background calculations, we did not include effect of Earth's X-ray albedo which will have significant contribution to the total polarimetric background due to low earth orbit of the satellite. We assume that the albedo background is not polarized which is a fair assumption because of the low earth orbit of Astrosat and resultant azimuthal symmetry in scattering of albedo from the Earth's atmosphere. We have modelled the albedo background and included effective shielding at individual detector module level. This enables us to calculate module wise polarimetric background as shown in Fig. 4.17 and thus provides reliable estimate of effective background. The estimated average background is now ∼1.5 Crab.

One important repercussion of our module-wise background calculation is the realization that different subsets of CZTI detector plane will have different sensitivities according to the net background for the given subset. This provides a very powerful handle to cross-verify the actual polarization measurement between different subsets and thus to have enhanced confidence in the polarization measurement. It should be noted here that due to the availability of event wise data, all such sub sampling, either in selection of module subset or the energy range can be carried out at the analysis level and thus does not impose any special restriction on the actual observation.

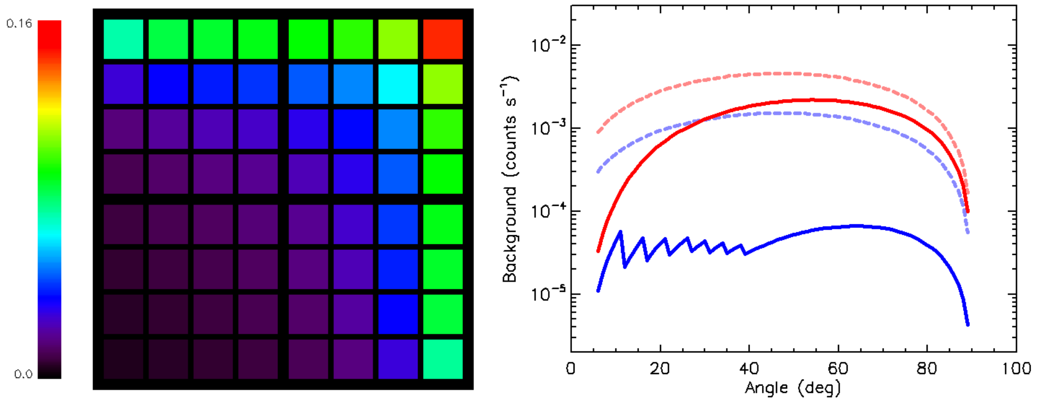

Figure 4.17: Left: Polarimetric background in the energy range of 100 – 300 keV expected for individual detector modules of CZTI. Right: Angle dependent contribution of diffuse X-ray background to the total background for the innermost (blue) and outer most module (red) to demonstrate the effect of collimators and module location. The dashed curves show background without considering module wise collimators.

4.4.3 Results

Since there is no way to distinguish between the double pixel events due to Compton scattering of genuine source photons and due to CXB and albedo photons, the large background from CXB and albedo degrades the modulation pattern. To incorporate this effect, we degrade the simulated azimuthal distribution for 100% polarized beam, i.e. flatten it in the proportion to the total polarimetric background expected in each azimuthal bin, assuming that the azimuthal distributions of the CXB and albedo photons do not have any intrinsic modulation. Effective modulation factor is then calculated from this degraded azimuthal distribution.

Sensitivity of CZTI in terms of the Minimum Detectable Polarization (MDP) for Crab like sources is estimated using spurious event rate and degraded modulation factors for exposure time of 1 Ms. Fig. 4.18 shows the polarimetric sensitivity of CZTI in terms of MDP as a function of source intensity. Different colors represent MDP for different modular subsets of CZTI plane. Sensitivity for inner subsets is higher compared to outer subsets as expected because of higher background in the outer modules. Since, the modulation factor depends on the

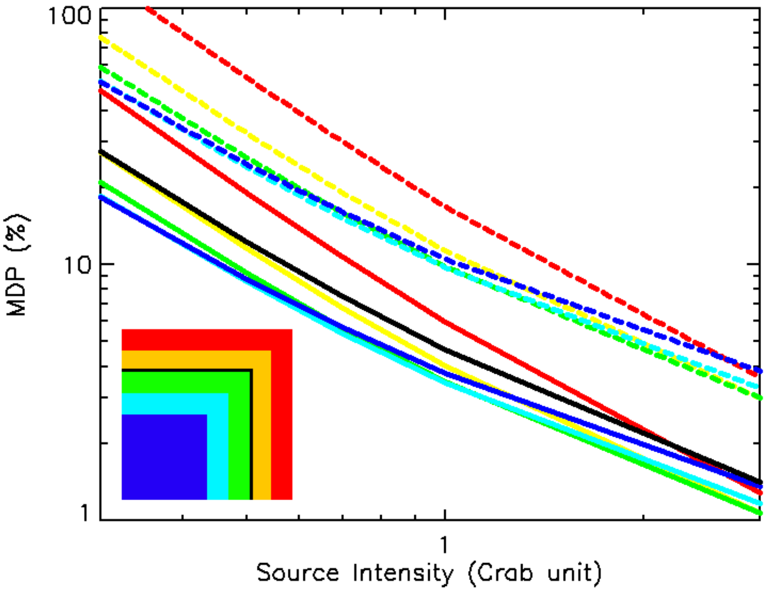

Figure 4.18: Polarimetric sensitivity of CZTI in terms of MDP as a function of source intensity for exposure time of 1 Ms. The dashed and solid lines represent the polarization angle aligned with the pixel edges and at 45° respectively with the latter being more sensitive due to higher modulation factor as expected. Different colors represent sub-samples of CZTI detector plane as shown in the inset. The black line represent the overall MDP as mentioned in the text corresponding to average 22.5° polarization and third (green) sub-array

angle of polarization, sensitivity of the instrument is also polarization angle dependent. For a Crab like source, expected MDP is 4% to 10% for 1 Ms exposure when the polarization angle with respect to the instrument reference is 45° or 135° and 0° or 90° respectively. MDP values for different source intensities (Crab unit) and different time exposures (1 Ms and 500 ks) are shown in Table 4.1 for inner 6 × 6 modules. The Soft Gamma Ray Detector (SGD), which is a narrow field Compton telescope onboard forthcoming Japanese mission Astro-H [117] to be launched next year, will also have polarization measurement capability based on Compton scattering principle in 80 − 300 keV [118]. Polarimetric sensitivity of SGD is significantly better than that of CZTI primarily due to lower background and lower energy threshold of the instrument [1].

---

[1] Astro-H was launched on February 17, 2016. However, according to the Japan Aerospace Exploration Agency (JAXA), communication with the satellite unfortunately failed on March

Table 4.1: Polarimetric Sensitivity of CZTI

Source intensity (Crab)	Time exposure	MDP (%)
0.3	1 Ms	20.0 - 59.0
	500 ks	29.0 - 83.0
0.5	1 Ms	9.0 - 26.0
	500 ks	13.0 - 37.0
0.7	1 Ms	5.5 - 16.0
	500 ks	8.0 - 22.5
1.0	1 Ms	3.5 - 10.0
	500 ks	5.0 - 14.0

It can be seen that the polarimetric sensitivity of the Astrosat-CZTI is mainly limited due to the off-axis background because the collimators and other support structures are designed for the primary spectroscopic range upto 150 keV only. The transparent support structure, however, can be used for advantage by attempting polarimetry of off-axis bright X-ray sources or transient events such as gamma-ray bursts. Particularly in the case of GRBs, it might be more helpful to keep the lower energy threshold of 35 keV, so as to get higher modulation factor. The increased polarimetric threshold of ∼150 keV will not result in significant degradation of the sensitivity due to the intrinsically hard spectrum of GRBs, whereas the rejection of the escape events will enhance the modulation due to the intrinsic polarization in the GRB photons available within the short duration. This can be readily done during the data analysis and does not require any change in observation mode. We plan to carry out detailed Geant$-$4 simulations for the off axis and out of the field of view sources to estimate their impact on the polarimetric sensitivity as well as to investigate the prospects of GRB polarimetry with Astrosat-CZTI.

26, 2016.

4.5 Experimental Confirmation

In order to confirm the polarimetric capability of CZTI, we carried out an X-ray polarization measurement experiment using the actual flight model of CZTI module ensuring that all properties of flight electronics are also included in the experiment. We produced a partially polarized beam of X-rays by scattering 356 keV X-rays from the radio-active source ^{133}Ba at ~90 degrees (see Fig. 4.19). A 6 cm long Aluminium cylinder was used as a scatterer. The source and the scatterer were placed inside a 4 cm thick Lead cylinder with a slit of 5 cm length and 2 mm width. The CZTI module is kept below the slit such that only the photons from ^{133}Ba scattered at 90° by the Aluminium scatterer can reach the CZTI detector. With this setup, the angle of scattering is constrained to $90^\circ \pm 15^\circ$ implying a partially polarized beam of energy between 190 keV and 240 keV.

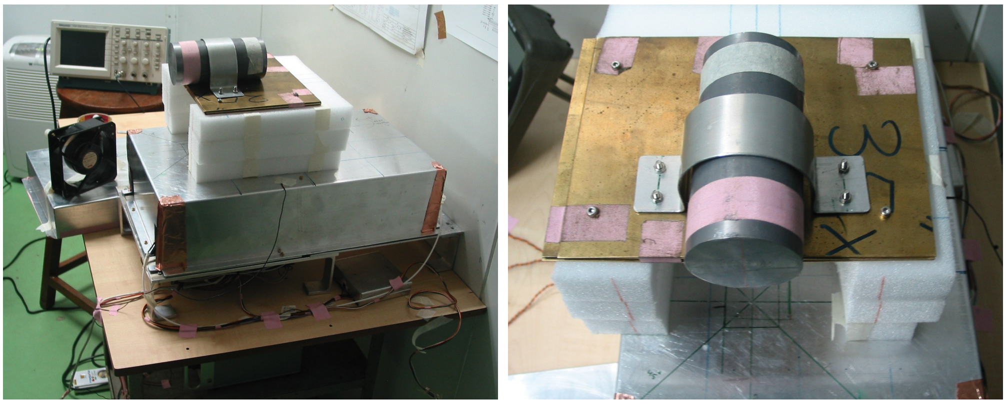

Figure 4.19: Left: Polarization experiment setup with CZTI. Right: zoomed view of the setup

The basic data filtering and analysis were carried out as discussed in Sec. 4.2. This involved selection of appropriate adjacent double pixel events, generating 8 bin azimuthal distribution with reference to lower energy pixel and correcting azimuthal distribution for the unequal angle bins. Fig. 4.20 shows the corrected modulation curves for partially polarized beam at two different polarization angles, 0° and 45°, with reference to one of the edges of the CZT detector module as well as for an unpolarized beam (direct exposure to 356 keV X-rays). It can be seen that the modulation curves for the measurements at these polarization angles show clear signature of the polarization of the incident beam and the modulation curves corresponding to different polarization angles also change as expected. The errors in the observed modulations are nominal 1σ errors and the simulation results too have errors of similar magnitudes. In the case of the unpolarized beam, the residual modulation, which could be due to the instrumental artifacts, is almost negligible (1%) and thus will not have any significant effect on the polarization measurement aimed at largely polarized source. It should be noted here that one major criticism of the recent X-ray polarization measurements by INTEGRAL IBIS and SPI instruments is that these instruments were never tested with an unpolarized beam. These results clearly demonstrate that

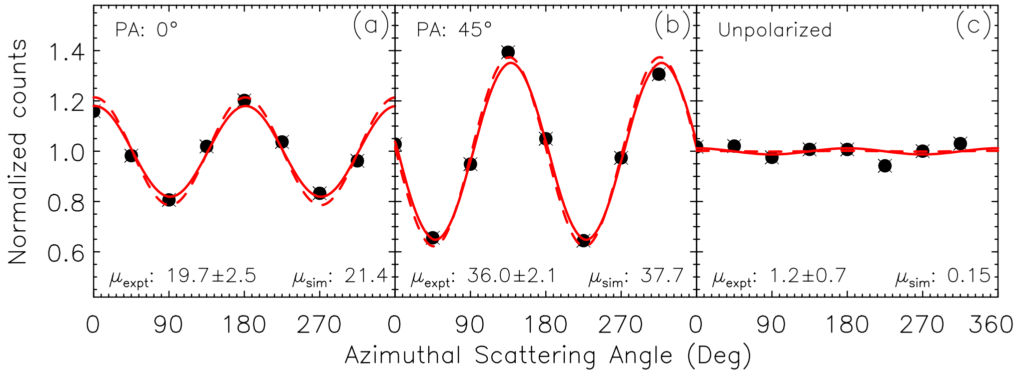

Figure 4.20: (a) and (b) Experimentally measured modulation curves for partially polarized X-rays from ^{133}Ba source at two polarization angles 0°, and 45° respectively. (c) The same curve measured for unpolarized X-rays from ^{133}Ba. The dashed line shows the modulation curves obtained from the Geant−4 simulations of the experimental setup

CZTI is capable of detecting polarization of the incident X-rays. However, the observed modulation amplitude cannot be directly used to validate the simulation because of the partially polarized beam. In order to have a quantitative comparison with the simulations, we repeated the simulations for the exact geometry of the experiment including the generation of the polarized beam and considered the experimentally measured background to calculate the modulation factor. The modulation factors obtained from these simulations typically agree within $\sim$1% of the experimentally measured modulation factors, in all the cases. This implies that the value of μ_{100} obtained from simulations do represent realistic modulation factor.

4.6 Astrophysical significance of CZTI Polarimetry

It can be seen from Fig. 4.18 that for a Crab like source, MDP of 5% can be achieved in exposure time of ~1 Ms. Though such long exposure times are routinely quoted in the context of X-ray polarimetry, these may not be realistic for the observatory class mission such as Astrosat. On the other hand, in the energy range of interest ($100 - 300$ keV) the emission from almost all X-ray sources is expected to be of non-thermal origin and thus can be highly polarized. This is corroborated by the recent reports of more then 50% polarized soft gamma emission by INTEGRAL from two bright X-ray sources Crab and Cygnus X-1 [15–17]. In this context, a more appropriate question is - given highly polarized X-ray emission, how well its polarization can be constrained by CZTI with a typical exposure time of few tens of kilo-seconds.

For an unknown source, the polarization degree P is given by -

$$P = \frac{\mu}{\mu_{d,100}}, \tag{4.4}$$

where, μ and $\mu_{d,100}$ are the measured modulation amplitude for that source and the degraded modulation factor respectively. It should be noted that the degraded modulation factor $\mu_{d,100}$ takes into account the effect of Compton scattering of the background photons (both cosmic X-ray background as well as albedo background) as discussed earlier and hence it is smaller then μ_{100} obtained from Geant$-$4 simulations. Error in the measurement is given by

$$\frac{\sigma_P}{P} = \sqrt{\frac{\sigma_\mu^2}{\mu^2} + \frac{\sigma_{\mu_{d,100}}^2}{{\mu_{d,100}}^2}}, \tag{4.5}$$

where, σ_μ is the statistical error associated with the measurement of modulation factor μ which depends on both the degree of polarization in the source and the source intensity. $\sigma_{\mu_{d,100}}$ is the error in $\mu_{d,100}$. It should be noted that

$\sigma_{\mu_{d,100}}$ depends on the relative angle between the polarization direction of the incident X-rays and a reference direction of the instrument. In general, the polarization angle can not be constrained to better than $28.5^\circ/(P/\sigma_P)$ simply by fitting the modulation curves [119]. Thus in most cases, the uncertainty in polarization angle can be assumed to be $15^\circ - 20^\circ$. Fig. 4.21 shows the detection significance for different source intensities as a function of exposure time, with $\mu_{d,100}$ and $\sigma_{\mu_{d,100}}$ corresponding to the average polarization angle of 22.5° and uncertainty in polarization angle of ±10°. It can be seen that for large exposure

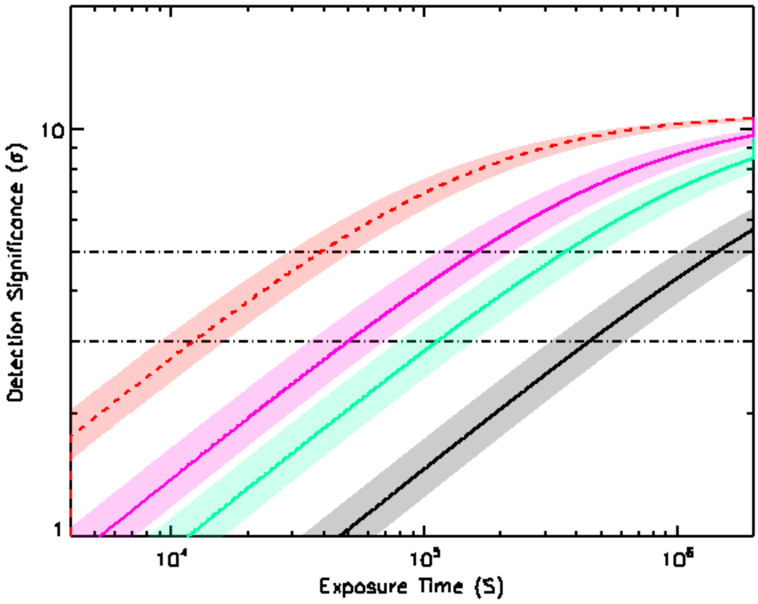

Figure 4.21: Detection Significance of polarization measurement for highly polarized bright sources. The bottom three lines correspond to 500 mCrab sources with polarization fraction of 20% (black), 40% (green), 60% (pink) respectively. The top line (red, dashed) corresponds to 1 Crab source having polarization fraction of 50%

times, the significance of polarization measurement saturates due to the uncertainty in $\mu_{d,100}$. However, for smaller exposure times (100 ks), the uncertainty in polarization measurement is dominated by the counting statistics. Since the large exposure times are expected to be resulting from multiple smaller exposure times with different position angle of the spacecraft, it is more appropriate to consider the average polarization angle of 22.5° (this is the angle with reference to the instrument reference direction and not the absolute polarization angle in the sky frame). However, in many such cases, it might be possible to have better constrains on absolute polarization angle based on multiple smaller subset of the same data, which may result in higher significance of the polarization measurement. Another factor affecting detection significance of polarization is the uncertainty in polarimetric background. The shaded regions around lines in Fig. 4.21 represent the variation of significance for probable variation of the polarimetric background by ±20% for the same statistical and systematic errors. It can be seen that, even after considering all these uncertainties, for a 500 mCrab source with 40% intrinsic polarized fraction, the polarization can be measured with 3σ confidence with an exposure time of $100 - 150$ ks.

Since polarization measurements with CZTI are possible only for bright ($>$ 500 mCrab) X-ray sources, the obvious candidates are the two eminent sources Cygnus X-1, a black hole binary and Crab, a pulsar wind nebula. The fact that the initial indication of highly polarized emission from both these sources are available from INTEGRAL observations, makes the astrophysical significance of CZTI polarimetric capability more relevant.

In the case of Cygnus X-1, measurements by both IBIS and SPI instruments on INTEGRAL show very high polarization fraction (~65%) at energies greater than ~250 keV, which is interpreted in terms of the emission from the base of a jet [15]. While a significant contribution from the jet to hard X-ray / soft gamma emission has been speculated for some other black hole binaries in literature [25–27], recent SED modelling of Cygnus X-1 spectral energy distribution by Zdziarski *et al.* [28], spanning from radio to MeV range, suggests that significant jet contribution to hard X-ray emission can be achieved only with rather unrealistic parameters. On the other hand, there are other models which predict state independent high polarization [24, 29] as well as moderate polarization only in hard state. Thus the present scenario of polarized nature of hard X-ray emission from Cygnus X-1, both fro observations as well as theoretically, is rather confusing and it is thus important to independently constrain it. In this context, we considered various available predictions of X-ray polarization for Cygnus X-1 to investigate whether these can be delineated with CZTI , particularly in the presence of some of the systematic effects such as uncertainty in background, uncertainty in the knowledge of polarization angle etc. (see Fig. 4.22).

The possible scenarios considered here (denoted by red, green, black and blue respectively in Fig. 4.22) are – strong polarization signature (∼ 50%) in LHS (low hard state) due to relatively high jet contribution; comparatively lower polarization fraction of 25% because of relatively lower jet contribution in LHS; ∼15% polarization in LHS originated in corona due to inverse Compton scattering and high polarization (around 55% in high soft state) because of synchrotron radiation from the corona itself. We found that most of the scenarios can be constrained rather accurately within an exposure of time of ∼200 ks.

In the case of the Crab nebula, based on the polarization measurements at other wavelengths (including soft X-rays which is the only historic positive X-ray polarization measurement from an astrophysical source [2]), it is well known that the nebular emission arises from synchrotron radiation. However, the mechanism as well as the geometry of the emission from the pulsar itself are still not fully understood with various models such as polar cap, outer gap, slot gap, stripped wind [120, 121], being compatible with all other observational characteristics. One distinguishing feature of these models is their phase-dependent polarization signature. The INTEGRAL measurements, folded with the Crab pulse period, suggests that the polarization is varying at different phases, and thus goes against the polar cap model. But in order to constrain other models it is necessary to get truly phase resolved polarization measurements, which typically need an order of magnitude larger exposure time. Since the Crab is likely to be observed for a long duration as a standard candle, it is possible that a total exposure of a few million seconds can be obtained. In such a case, we find that full phase resolved polarization measurement is certainly possible with the lowest polarization also constrained better then 3 sigma. As an example, Fig. 4.22 shows the Crab polarization detection significance, estimated in 16 uniform phase bins. The phase resolved polarization values used in our calculation are obtained by interpolating the recent Crab polarization estimates by IBIS [81]. Thus, we see that CZTI can

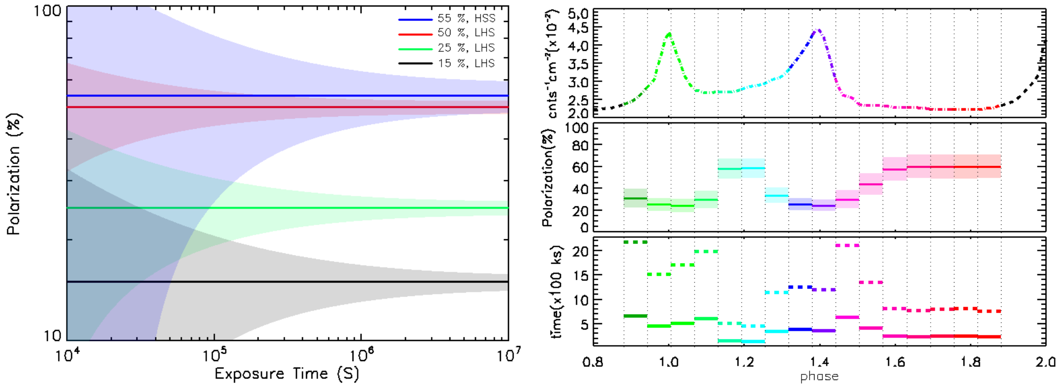

Figure 4.22: Left: Possible constrains on hard X-ray polarization fraction of Cygnus X-1 for some of the model predictions proposed in literature (see text for details), predicting about 15%, 25% and 50% polarization in low hard state (total flux sin300 mCrab) and about 55% polarization in high soft state (total flux ~1 crab). Expected errors are shown as shaded regions. Right: Feasibility of phase resolved polarimetry with CZTI for Crab. The top panel shows Crab pulse profile in 100 300 keV. The middle panel shows polarization in 16 phases as expected from an interpolation of the polarization measured by INTEGRAL in four regions of Crab pulse profile. The shaded region represents possible constraints on phase wise polarization measurement with CZTI for a total exposure time of 1 Ms. The bottom panel shows the required exposure time to determine polarization for all phases with a minimum 3 sigma (solid lines) and 5 sigma (dashed lines) confidence levels. It can be seen that with a total exposure time of ~2 Ms, polarization in most of the phases can be constrained with better then 5 sigma confidence

provide much better insights into the Crab pulsar emission mechanism.

However, polarimetric studies with CZTI will not be limited to only these two sources. There are many transient X-ray binaries, which undergo outbursts lasting from a few weeks to months and have intensities more then 500 mCrab. Since such transient sources are of general interest, it is likely that at least the long outbursts will be observed extensively by Astrosat and thus will result in a total exposure time sufficient for the polarimetric studies with CZTI. Based on the analysis of long term monitoring data from sky monitors such as RXTE-ASM, SWIFT-BAT, we find that typically 2 to 3 outbursts which are brighter then 500 mCrab and longer than one week are expected during the period of one year (see

Table 4.2).

Table 4.2: List of potential sources for CZTI polarimetry obtained from BAT 70 month catalog [122]

Source Name	Source Type	ON Time (>300 mCrab)	ON Time (>500 mCrab)
Crab	Pulsar/PWN	100 %	100 %
CygX1	Black Hole HMXB	95.03 %	92.57 %
GX339-4	Black Hole LMXB	3.03 %	− − −
XTEJ1752-223	Black Hole LMXB	4.45 %	− − −
SWIFTJ1753.5-0130	Black Hole LMXB	1.94 %	− − −
SGR1806-20	Magnetar	2.69 %	− − −

Thus, given an operational life of 5 years, CZTI is likely to investigate the presence of highly polarized emission from at least 10 transient sources which are typically black hole and neutron star binaries.

4.7 Summary

To summarize this chapter, Astrosat-CZTI will have significant polarimetric capabilities. The polarization capabilities are verified on ground, both with partially polarized beam, and more importantly, with unpolarized beam. This will provide additional confidence to consider the actual polarization measurements as intrinsic to the source and constrain various theoretical models based on them. The GAP (Gamma-ray Burst Polarimeter) instrument, which is a small Compton scattering based polarimeter onboard a Japanese Small Solar Power Sail Demonstrator mission IKAROS [123], has demonstrated the importance of robust ground calibration of polarimeters based on which it is successfully measuring polarization of GRBs. As mentioned earlier the Soft Gamma Ray Detector (SGD) onboard Astro-H to be launched next year [2], provides significant polarization

---

[2] According to recent news, after one month of its launch, communication with Astro-H failed on March 26, 2016.

measurement capability in hard X-rays [118]. Astrosat-CZTI with much larger area compared to GAP and much larger field of view compared to SGD, will prove to be an unique instrument capable of probing the X-ray polarization of bright celestial sources. Further, Astrosat being an observatory class satellite with X-ray timing as one of its primary objectives, it is likely to devote a large fraction of its observing time to bright X-ray binaries, thus facilitating, as an additional bonus, measurement of X-ray polarization in the $100 - 300$ keV region. Since at energies beyond 100 keV, the coded mask and supporting structures of CZTI become more and more transparent, CZTI offers opportunity to attempt polarization measurements of GRBs which are expected to be highly polarized. Thus it is likely that the field of hard X-ray polarimetry will witness significant advances in the near future.

Chapter 5

Generation of Multi-Pixel Response Matrix for Astrosat-CZTI

In Chapter 4, we described the prospects of hard X-ray polarimetry with Cadmium Zinc Telluride Imager (CZTI) onboard Astrosat. However, it is to be noted that polarization measurements with CZTI is just an additional bonus, as CZTI is primarily a coded mask spectroscopic instrument sensitive in $20 - 100$ keV energy range. With proper characterization of the CZT detectors, it is possible to carry out fine spectroscopic analysis for celestial X-ray sources with CZTI. Better spectroscopic study of sources and proper interpretation on the emission mechanisms prevalent at those sources out of the spectroscopic data critically depends on the response matrix of instrument. So, apart from polarization study with CZTI, we also worked on the characterization of CZTI detector modules to generate accurate response matrix of the instrument.

CZT detectors provide high photopeak efficiency in a broad energy band of few keV to few hundreds of keV, fine energy and spectral resolution at near room temperature and can be operated in a wide temperature range. It also provides the sufficient radiation hardness required for any space based experiments. CZT detectors, for all these reasons, have been boosting hard X-ray astronomy for more than a decade now, having been used in many X-ray astronomy experiments and missions – SWIFT [124], INTEGRAL [125], NuSTAR [93], EXIST [126], RT-2 experiment onboard CORONAS-PHOTON [92] and planned for future astronomical missions like Astro-H [1] [75], X-Caliber [76] etc. As mentioned earlier, CZTI onboard Astrosat [89] also uses an array of CZT detector modules. However unlike other semiconductor detectors (Si, Ge detectors), the X-ray lines due to mono-energetic X-ray photon interactions in CZT do not feature Gaussian shape due to incomplete charge collection on the electrodes due to low mobility and lifetime of the charge carriers (electrons and holes). In particular, low mobility of the holes coupled with very low lifetime causes a significant fraction of charge being trapped by impurities. Since charge collection depends on the depth of interaction which is a statistical phenomena, there is a long tail at the lower energy side of an otherwise Gaussian line shape. Since at higher energies, depth of interaction increases, the tailing effect is also found to be more prominent for high energy photons. In order to fully utilize the capability of CZT detectors by performing fine spectroscopic studies out of it, it is important to generate accurate response matrix. For that, it is necessary to model the CZT line shapes precisely by taking care of the mobility and lifetime of the charge carriers. Method to predict CZT line profiles by modelling charge trapping (hereafter, $\mu\tau$ model) has been discussed in [100, 127]. However, the line profiles become further complicated when the CZT detectors are pixelated as in case of NuSTAR or Astrosat-CZTI as charge sharing, Compton scattering between the pixels may also contribute to the tail of the line.

In this chapter, we demonstrate our modelling results to the line shapes for 5 mm thick CZT crystals with 16 × 16 pixels (2.45 mm pixel pitch) procured from Orbotech Medical Solutions, similar to the detectors used in CZTI onboard Astrosat, so that the same method can be implemented for CZTI for response matrix generation. We found that though $\mu\tau$ model fit the CZT line profile quite well at higher energies, at lower energies (~60 keV), proper fitting requires an additional component in the model – charge sharing between the pixels. It

---

[1] According to recent news, after one month of its launch, communication with Astro-H failed on March 26, 2016.

is interesting as provided the small photo-electron range for any X-ray photon interaction (charge cloud radius) and pixel pitch of 2.45 mm, charge sharing is not expected to be significant. However, we did extensive experiments to validate our model and in particular justify the requirement of the charge sharing component in the model. The numerical models are described in Sec. 5.1 and can be used for any pixel size of the CZT detector and detector thickness, therefore may be helpful in characterizing CZT detectors in future astronomy missions as well besides CZTI. Again one of the key features of the model is that it uses charge sharing fractions as a fitting parameter and does not consider the complicated electric field geometry to evaluate the wighting potentials. Therefore, it is possible to understand the charge sharing process for a given CZT pixel geometry using these models with the help of optimized experiment setup. In Sec. 5.2, we describe the procedure to experimentally estimate the $\mu\tau$ products and charge sharing parameters followed by an experiment to validate the model in Sec. 5.3. Finally, we summarize our results and future plans in Sec. 5.4.

5.1 CZT Line Model

As discussed earlier, the model consists of two physical components which are descibed in the following.

Charge trapping: The shape of mono-energetic X-ray line from CZT detectors depends on $\mu\tau$ product of charge carrier. For a uniform electric field (E) in CZT crystal, the fraction of charge collected from specific interaction depth is given by Hecht equation [128],

$$\eta = \frac{\lambda_e}{D}\left[1 - \mathrm{e}^{-\frac{D-x}{\lambda_e}}\right] + \frac{\lambda_h}{D}\left[1 - \mathrm{e}^{-\frac{x}{\lambda_h}}\right], \tag{5.1}$$

where, η is the ratio of induced charge to the initial charge generated after interaction, D is the thickness of the crystal, x is the distance of interaction site from cathode and λ_e (=$(\mu\tau)_e E$) and λ_h (=$(\mu\tau)_h E$) are the mean free paths for electrons and holes respectively.

We have developed a numerical model to predict line shape from CZT detectors based on Eq. 5.1, where we divide the CZT crystal in N number of layers along

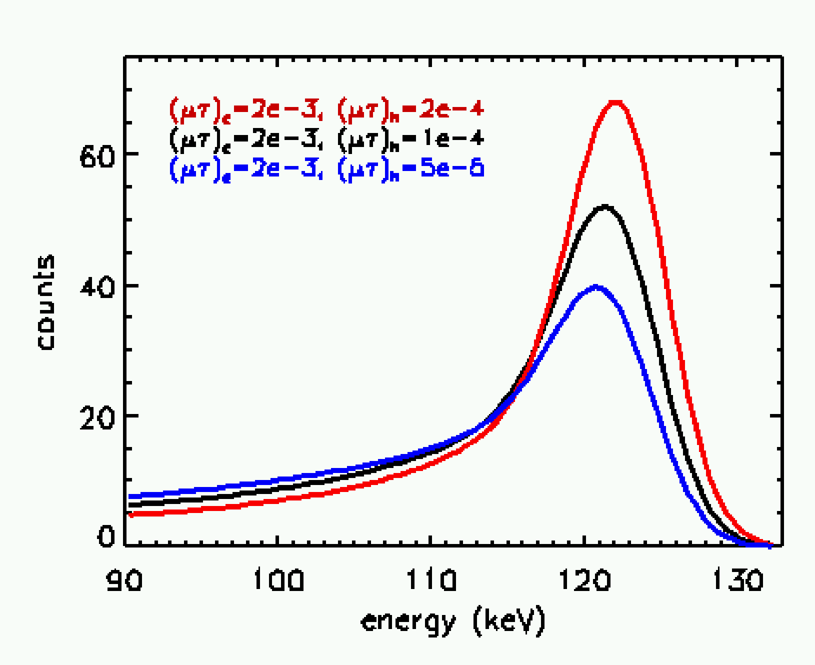

Figure 5.1: Demonstration of tailing effect in CZT line shape due to charge trapping ($\mu\tau$ model) for 122 keV photon energies. Different colors denote different $\mu\tau$ products

its depth where each layer will give rise to a Gaussian with peak energy depending on the induced charge for that layer. The amplitude of the Gaussian will depend on the probability of interaction at that layer for the given energy (E_0) of the X-ray photons. All the Gaussian lines are finally added together to obtain the final line shape, F,

$$F = \sum_{i=1}^{N} N_0 P_i \mathrm{e}^{-\frac{(E-\eta_i E_0)^2}{2\sigma_i^2}}, \tag{5.2}$$

where, i runs from 1 to N number of slices which we consider to be 100 for our calculations. N_0 is the number of incident photons and P_i is the probability of interaction at the i^{th} layer for photons of energy E_0, given by

$$P_i = \mathrm{e}^{-\mu\rho x}(1 - \mathrm{e}^{-\mu\rho(D/N)}). \tag{5.3}$$

σ_i is the width of the Gaussian which is assumed to be same for all the layers. If λ_e and λ_h are high i.e. values of $\mu\tau$ products are large, η tends to unity (see Eq. 5.1), resulting in a Gaussian shape for the X-ray line. Alternatively, for $x \sim 0$, i.e. interactions occurring close to the cathode η again tends to unity. Therefore, for low energy photons, we do not expect significant tail compared to higher energy photons. Fig. 5.1 shows the CZT line shapes predicted by the $\mu\tau$ model for 122 keV energy photons for various $\mu\tau$ products. The bias voltage considered here is 600 V. The line shapes are found to have more prominent tail with lower $\mu\tau$ product of holes.

Charge sharing: Charge sharing is required for pixelated detectors as the charge cloud formed after an X-ray photon interaction inside a CZT pixel, will diffuse due to random thermal motion of electrons and Coulomb repulsion. While traversing towards the electrode, a fraction of charge cloud may end up to the neighboring pixels giving rise to an incomplete charge collection. This will contribute to the tail of the line profiles making it further complicated.

We have developed a simple charge sharing model based on the cloud expansion due to random thermal motion of electrons. [129,130] also followed a similar treatment to account for cloud expansion. Since expansion of the cloud size due to Coulomb repulsion is insignificant compared to that due to thermal motion of charge carriers, specially for energies < 200 keV, we ignored the Coulomb forces in the electron charge cloud. Radius of charge cloud as it drifts across the detector can be estimated assuming Gaussian distribution of charge concentration as a function of drift distance (from solution of Fick's equation),

$$r = r_0 + 1.15\sqrt{\frac{2kTdD}{qV}}, \tag{5.4}$$

where, r_0 is the initial cloud radius and r is the cloud radius at the end of the drift d. q is electronic charge and V is the bias voltage. T is the detector temperature and k is Boltzmann's constant. r_0 is expected to be of the same order of the photo-electron range in CZT material for incident photon energy of E_0. One can estimate the amount of charge left inside the pixel assuming spherical charge cloud using Eq. 5.4,

$$f = 1 - \frac{\pi(r-y)^2}{3}(3r - (r-y))/\frac{4}{3}\pi r^3, \tag{5.5}$$

where, y is the position of interaction from the edge of the pixel. The model essentially implies that for interactions closer to the edge of the pixel, there will be significant charge loss. As we move towards the center of the pixel, at some distance from the edge equal to the radius of the final charge cloud, charge loss will stop. This will give rise to a tailing effect as amount of charge loss will depend on the interaction site from the edge and on the depth of interaction.

We couple the charge sharing model with the charge trapping by dividing the CZT detector plane into M number of slices and compute the charge loss for each slice due to both charge sharing and charge trapping for vertical N slices as explained earlier. The final model looks like,

$$F = \sum_{j=1}^{M} \sum_{i=1}^{100} N_{0j} P_i \mathrm{e}^{-\frac{(E-\eta_i f_{j,i} E_0)^2}{2\sigma_i^2}}, \qquad (5.6)$$

where, j runs from 1 to M number of slices along the plane of CZT, which we consider to be 2000 for calculations and i runs for 100 slices in vertical direction along the depth of CZT for a given j. N_{0j} is the number of incident photons in j^{th} slice and can be considered same for the slices in case of uniform illumination ($N_{0j} = N_0/M$) or of some other suitable functional form in case of nonuniform illumination. Fig. 5.2 shows the model predicted CZT line shapes for various r_0 (initial cloud radius) values for 60 keV and 122 keV photon energies. Effect of increase in charge cloud radius on the line shape is quite evident for both 60 keV and 122 keV photons. In case of 60 keV photons, the effect of charge trapping on the tail is insignificant as most of the photons will interact within ~1 mm from the cathode. Therefore, the tailing effect is only due to charge sharing. On the

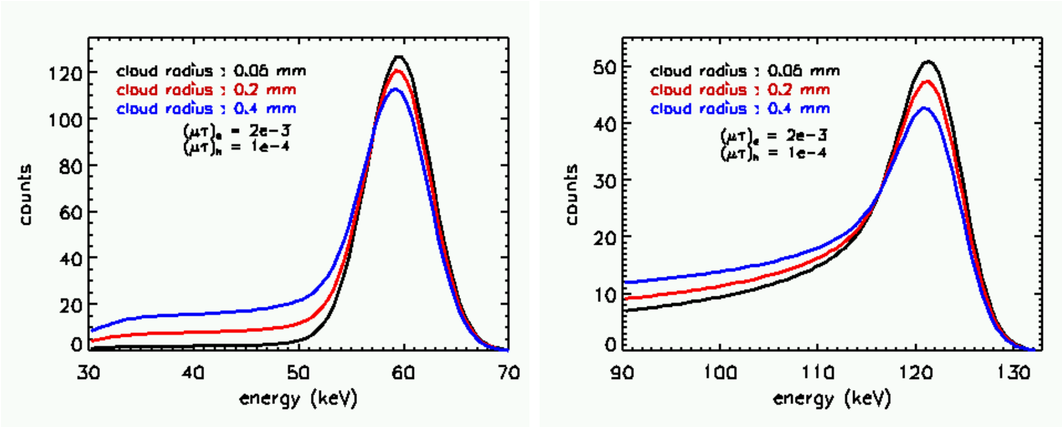

Figure 5.2: Model predicted CZT line profiles for 60 keV (left) and 122 keV (right) photon energies for various r_0 values. Assumed values of $\mu\tau$ product here are 0.002 and 0.0001 for electrons and holes respectively. The bias voltage is considered here to be 600 V

other hand, for 122 keV photons, the contributions of both charge trapping and charge sharing to the tail of the line are quite significant.

It is to be noted that here we only estimate the amount of charge going out of a given pixel; we do not bother about the amount of charge shared between two adjacent pixels which will further depend on the anode and interpixel geometry. Charge sharing from adjacent pixels and interpixel junction may also contribute to the tail of CZT line shape. The other factors which may have contribution to CZT line tails are

- Compton scattering from neighboring pixels to the pixel under consideration as the scattered photons will have energies close to the photopeak energy depending on the angle of scattering,

- escape of Bremsstrahlung photons (mostly generated from high energy photo-electrons) and electrons from the pixel will also lead to an incomplete charge collection and thus may affect the tail of line shapes.

However, effect of Bremsstrahlung photon escape and electron escape from the pixel is not very significant. Compton scattering from the adjacent eight pixels is also insignificant. This is demonstrated in Fig. 5.3, which is obtained from Geant$-$4 simulation of a 2.45 mm × 2.45 mm CZT crystal with thickness of 5 mm. The detector plane is uniformly illuminated by 59.54 keV (left) and 122 keV (right) photons. We see that the number of photons undergoing Bremsstrahlung escape and electron escape in the energy range $40 - 58$ keV (in case of 59.54 keV photons) is less than 0.3% of the total number of photons incident. The events below 15 keV are due to Compton scattering. We expect a similar number of events (actually less as these events are for scattering in all direction) in total from the neighboring eight pixels surrounding the central pixel. Fraction of these events is also found to be less than 0.4%. In case of 122 keV incident photons also, these numbers are found to be insignificant $\sim$0.2% and $<$4% respectively. These events are therefore not significant to contribute to the tail of the lines. Thus we only model the charge sharing fractions along with the charge trapping to predict the CZT line shape as function of incident photon energy.

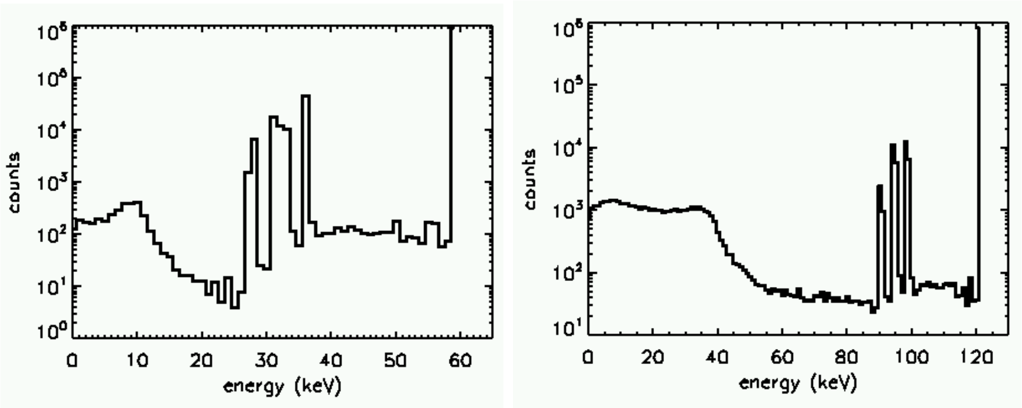

Figure 5.3: Energy distribution for 59.54 keV (left) and 122 keV (right) photons obtained from simulation for a 2.45 mm × 2.45 mm CZT crystal with 1 million incident photons. The main peaks in the distribution are the photopeaks and other smaller peaks correspond to escape photons. The events closer to the photopeak are because of escape of bremsstrahlung photons and escape of electrons. Events at the lower energies are the Compton scattered events

5.2 Measurements of $\mu\tau$ Products and Charge Sharing Fractions

The model (Eq. 5.6) is written in S-LANG and incorporated in spectroscopic data analysis package, ISIS (Interactive Spectral Interpretation System) as a local model. There are total six parameters in the model – $(\mu\tau)_e$, $(\mu\tau)_h$, photopeak energy E_0, N_{0j}, spread of the line σ, and initial radius of the electron cloud r_0. In order to constrain $\mu\tau$ product precisely, we fit three spectra at different energies (59.54 keV line from ^{241}Am, 88 keV line from ^{109}Cd, and 122 keV line from ^{57}Co) simultaneously tieing up the $\mu\tau$ product across the spectra as $\mu\tau$ product is expected to be constant for a crystal at a given temperature. It is to be noted that since the model components are energy dependent, fitting the model simultaneously for three different energies put tighter constraints on the model parameters rather than fitting the model for a single energy but at three different bias voltages.

We use CZT detectors procured from Orbotech Medical Solutions. The detectors are available as integrated detector module having both CZT crystal and the front end readout ASIC. Spectra is acquired by the data collection unit OMS36G256-SDK provided along with the OMS Detectors Array Unit (see Fig. 5.4). The gain-offset corrected spectra are first binned with a binsize of 0.5 keV

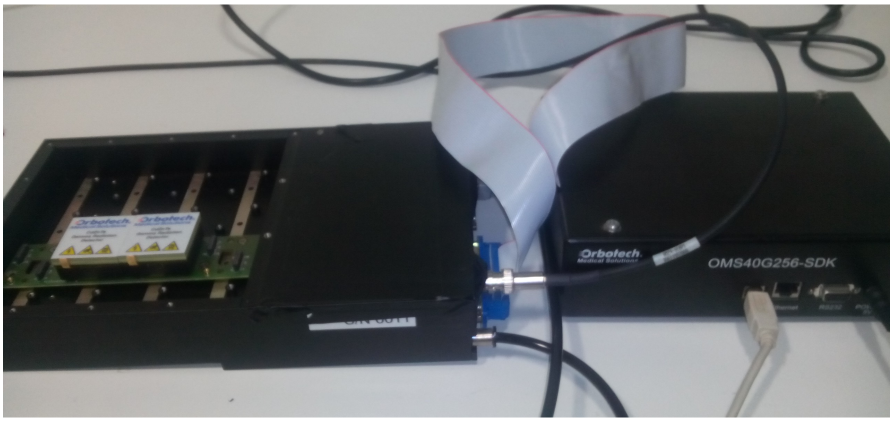

Figure 5.4: OMS Detectors Array Unit and the data collection unit OMS36G256-SDK

in energy space which are then fitted simultaneously by the CZT line model. σ, N_{0j}, E_0 are kept free while fitting. r_0 should depend on the energy of the incident photons as the charge cloud initial radius can be approximated as the ejected photo-electron range in CZT material which depends on the energy of the incident photons. However, the change in radius is not very significant for increase in photon energy from 60 keV to 122 keV. Again, as discussed earlier and we will see later, r_0 also takes care of other physical factors such as charge coming in from the adjacent pixels and interpixel junction to the pixel under consideration, which is expected to contribute to the tail of CZT line shape and therefore may modify the actual r_0 value. Consequently, we may not obtain any functional form of r_0 as a function of photon energy which is necessary to finally compute the response matrix elements of the detector as a function response energies. Therefore, we consider r_0 to be same for all three energies for a given pixel while fitting. r_0 obtained in this way, is basically the cloud radius averaged over energy range from 60 to 122 keV.

Another important factor to be noted here that closer to the anode, the electric field lines will be too dense due to fringing effect to allow further expansion of the charge cloud. We take care of this by assuming an optimized quenching distance of 3.5 mm from the cathode such that there will not be any further expansion in cloud size beyond this distance. This has a significant effect at higher energies as there is a significant probability of high energy photons to interact beyond this layer and therefore charge loss will be effectively smaller compared to that at lower energies (< 60 keV). This argument can be further seconded from the fact that in polarization experiments with OMS CZT detectors in Astrosat-CZTI, the experimental modulation factors were found to be very close to the simulation results in the energy range $190 - 240$ keV as discussed in Chapter 4, which implies that there is no significant charge sharing at higher energies.

Fig. 5.5 shows the obtained fitting for two separate pixels (120^{th} pixel (left column) and 200^{th} pixel (right column)) at three energies. We see that the model predicts the line shapes very accurately. We fitted spectra for all 256 pixels of a module and constrain $(\mu\tau)_e$, $(\mu\tau)_h$, and r_0 parameters. In Fig. 5.6, we show the

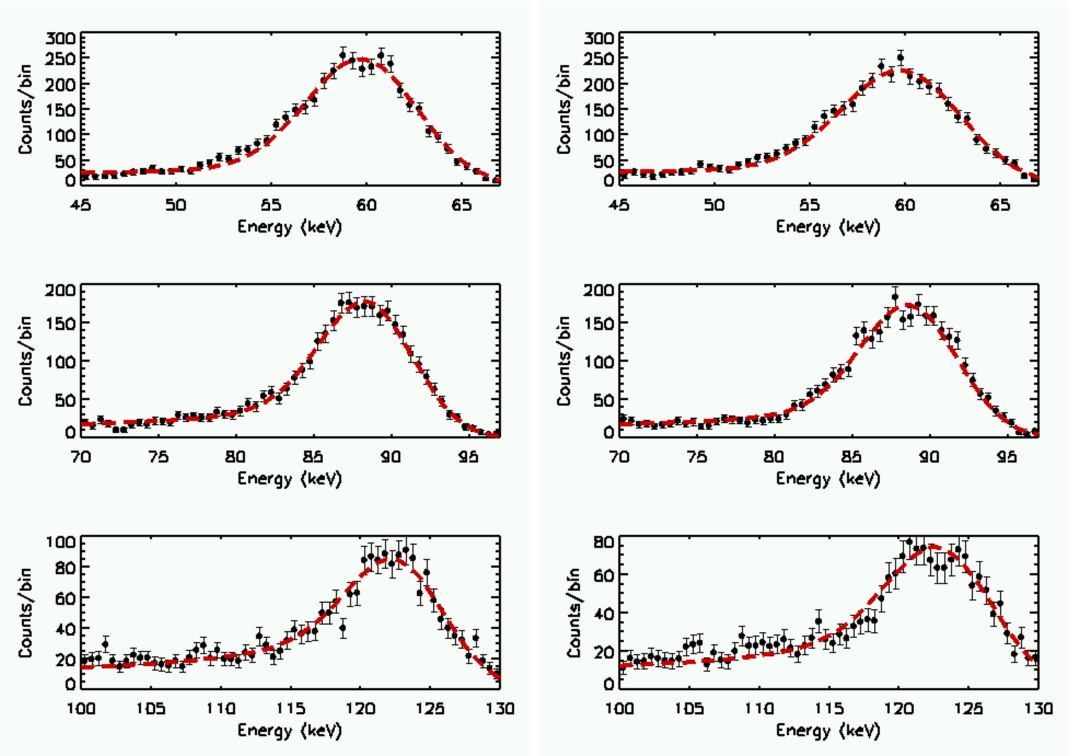

Figure 5.5: Simultaneous fitting of three spectra for two separate pixels – 120^{th} pixel (left column) and 200^{th} pixel (right column). The top, middle and the bottom panel show spectra for 59.54 keV line from ^{241}Am, 88 keV line from ^{109}Cd, and 122 keV line from ^{57}Co respectively

distribution of $(\mu\tau)_e$, $(\mu\tau)_h$ for the whole module. Typical $(\mu\tau)_e$, $(\mu\tau)_h$ values

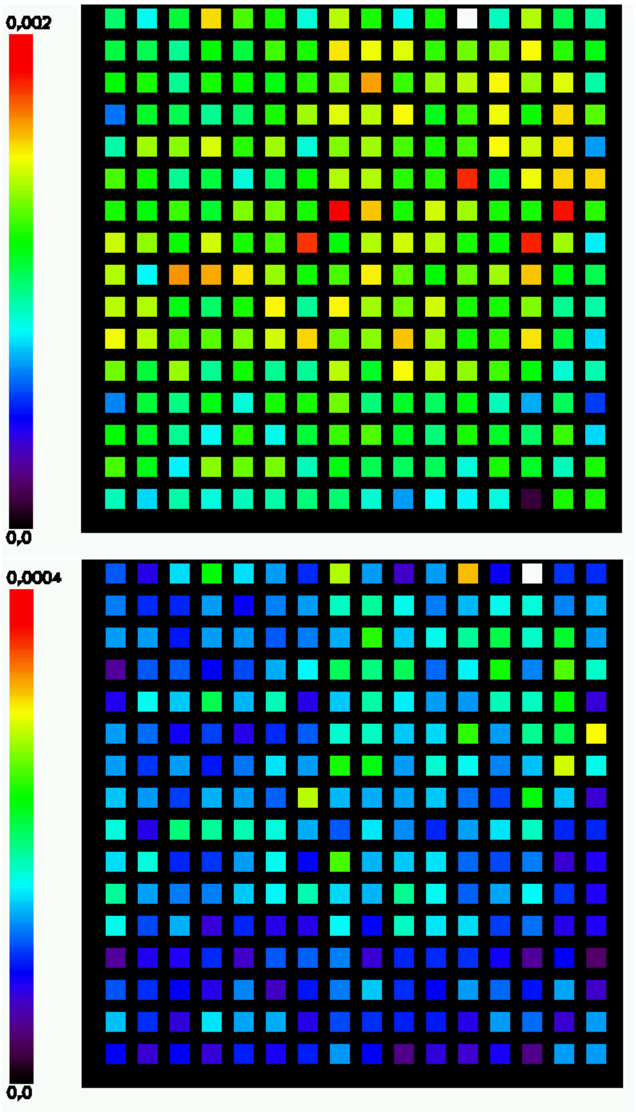

Figure 5.6: Distribution of $(\mu\tau)_e$ (top) and $(\mu\tau)_h$ (bottom) with pixels for CZT detector module. Mean values of $(\mu\tau)_e$, $(\mu\tau)_h$ are found to be around 10^{-3} and 10^{-4} respectively

are around 10^{-3} and 10^{-4} respectively. Fig. 5.7 shows the distribution of r_0 with pixels for the CZT detector module. Values of r_0 range from 0.2 mm to 0.5 mm, with mean found to be around 0.3 mm. Values of r_0 are bit higher compared to the photo-electron range averaged over $60 - 122$ keV. This is expected as in our model, we do not consider the charge coming in from the neighboring pixels and interpixel junction which will have significant effect in CZT line tail. Since flux of incident photons varies from pixel to pixel, relative contribution of these effects

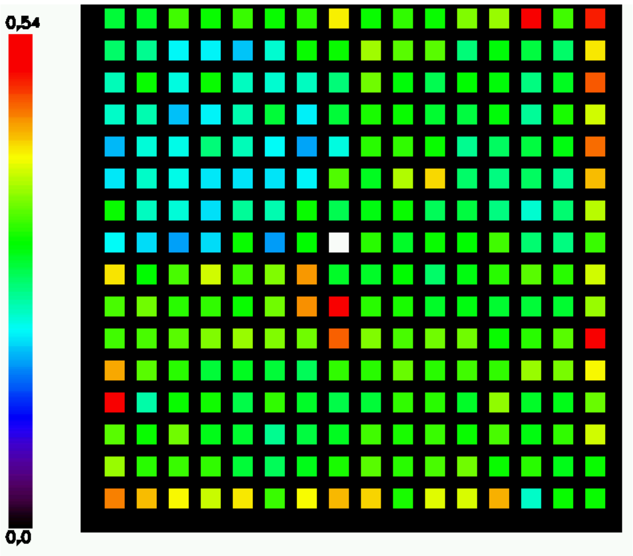

Figure 5.7: Distribution of initial charge cloud radius (r_0) with pixels for CZT detector module. Mean value of r_0 is found to be 0.3 mm

will change leading to a slight variation in obtained r_0 values with pixels.

5.3 Verification of CZT Line Model: Crosstalk Experiment

According to the CZT line model, charge sharing is expected to be significant at the edges of a pixel, whereas there should not be any charge sharing at the pixel center. On the other hand, charge trapping should not depend on the position of photon interaction on the pixel plane. In order to verify the model and importance of the charge sharing component, we carried out an experiment with CZT detector module, where instead of uniform illumination, at a time only a fraction of pixel area was illuminated starting from the left edge of a pixel to its right edge. The experiment setup is shown in Fig. 5.8. To illuminate the pixels at different positions with an accuracy of few μm, a micrometer system was used which can move both horizontally and vertically to adjust the position of illumination by radioactive sources. The pixels were made to shine by X-ray sources through a narrow slit of 0.2 mm in one direction and 20 mm in the perpendicular direction on a lead plate of dimension 60 mm × 60 mm with

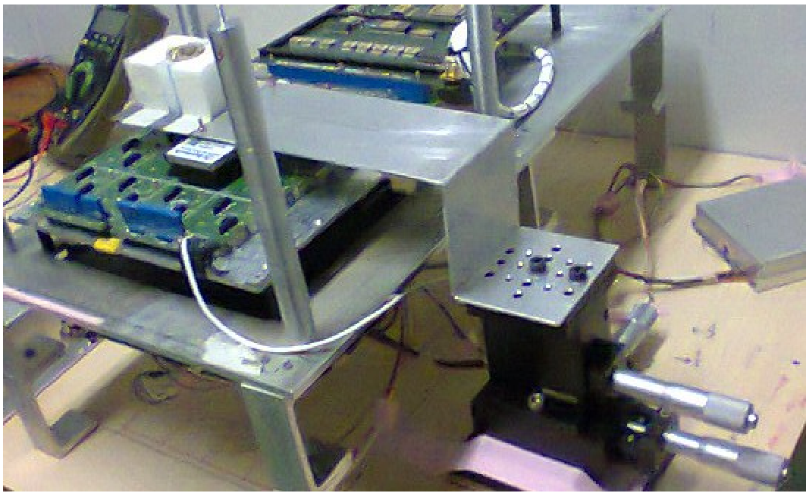

Figure 5.8: Experiment setup for Crosstalk experiment. The pixels were illuminated by source through a narrow slit to localize the pixel position.

thickness 1 mm which was kept on the movable arm of the micrometer system. Special care was taken so that the slit is aligned parallel to the pixel edges. The distance between the detector surface and the slit is kept very small (3 mm) so that the beam does not diverge across the boundaries of the pixels. In this way, for a particular position of the source-slit system, a narrow strip (∼0.2 mm) of eight pixels (along the slit length) was illuminated simultaneously. By moving the micrometer system in horizontal direction (perpendicular to the slit length) at small steps, different parts of a pixel starting from its left edge to its right edge can be illuminated.

We used two X-ray sources, ^{241}Am and ^{57}Co having line energies of 59.5 keV and 122 keV respectively. First, the position was set by looking at the pixel image in the software. For a particular position, the narrow strip of pixels was illuminated first by ^{241}Am and then by ^{57}Co. The same procedure was repeated for other positions by moving the micrometer system in the horizontal direction. For ^{241}Am, the experiment was repeated for two different thresholds − 33 keV and 40 keV. For ^{57}Co data were taken at three different thresholds − 33 keV, 40 keV and 60 keV.

Fig. 5.9 shows the count rate for ^{241}Am as a function of source-slit position for 133^{rd} (black) and 117^{th} (red) pixel. The slit was moved from the left edge of 133^{rd} pixel to the right edge of 117^{th} pixel. The total count rate is shown in blue.

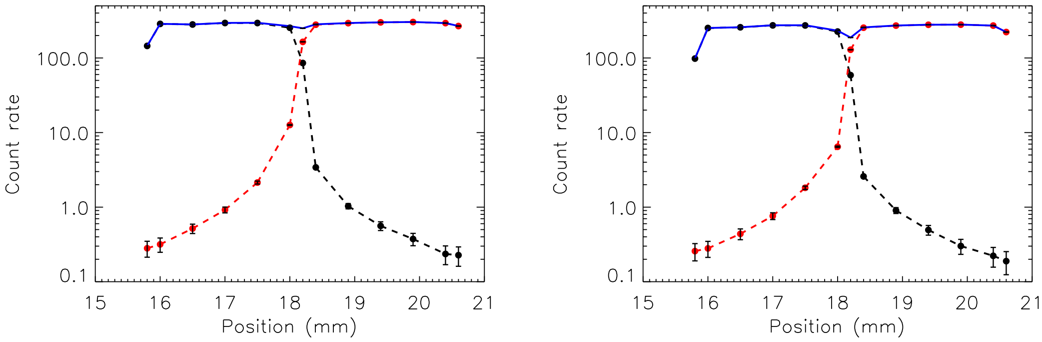

Figure 5.9: Count rate for 133^{rd} (black) and 117^{th} (red) pixel as a function of source-slit position for ^{241}Am. Total count rate is shown in blue. Left and right plot refer to 33 keV and 40 keV energy thresholds respectively in the CZT detector

We see a nonzero count rate in 117^{th} pixel even when the slit is on the 133^{rd} pixel, indicating a certain width in the X-ray beam due to divergence through the slit opening. The crossover in count rate for the two pixels indicate the interpixel junction and it is to be noted that at the interpixel junction, there is a significant dip in the total count rate (∼15% with respect to total count rate at the middle of a pixel) because of loss of events in both 33 and 40 keV thresholds. It can be due to interpixel dead area which depends on the electric field geometry. However, in that case, the decrease in count rate should not depend on the threshold (for 43 keV threshold, dip is ∼30%) and energy of incident photons (for ^{57}Co, there is an ∼6% excess in total count rate at interpixel junction (see Fig. 5.10)). Compton scattering events between these pixels are also unlikely to explain the dip as probability of Compton scattering is negligible at ∼60 keV for a 5 mm thick CZT crystal. Again, though in case of Compton scattering, the deposited energy is less than the threshold (33 keV or 40 keV), for the dip to occur, threshold has to be more than the scattered photon energy, which is not the case here for ∼60 keV photons. On the other hand, in case of charge sharing, we expect a maximum of 50% of charge to be shared to the neighboring pixel for interactions closer to the pixel edge. In that case, if the threshold is greater than the 50% of charge, we expect loss of events in both the pixels giving rise to a dip in the total count rate. With increase in threshold, the loss of events is expected to increase, which is also found to be true for 40 keV threshold (see Fig. 5.9).

Escape of fluorescence photons to the neighboring pixel may also lead to a loss of events in both pixels. However, such fluorescence escape events can not have any contribution to the tail in X-ray line shape. On the other hand, we find more and more prominent tail when moving from pixel center to pixel edge with a decrease in total cout rate (see Fig. 5.11), indicating that these two observed effects should be of same origin.

For ^{57}Co, we see an excess of events at the interpixel junction for 33 keV threshold, possibly due to double pixel events either because of Compton scattering or charge sharing (see top left plot in Fig. 5.10). In case of Compton

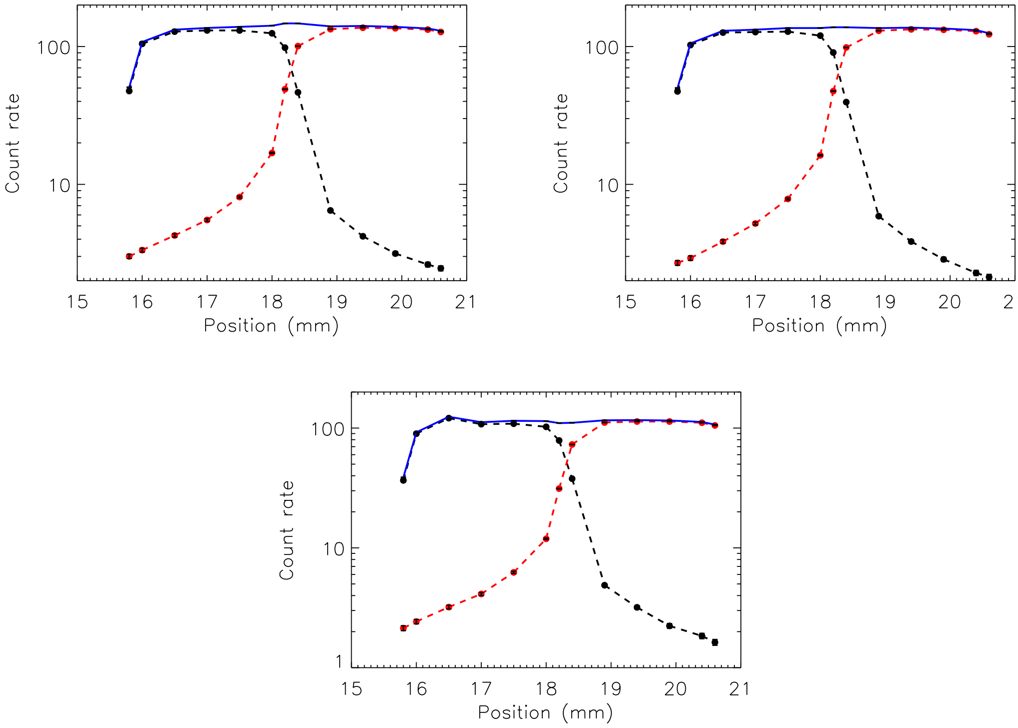

Figure 5.10: Count rate for 133^{rd} (black) and 117^{th} (red) pixel as a function of source-slit position for ^{57}Co. Total count rate is shown in blue. Top left, top right and bottom plot refer to 33 keV, 40 keV and 60 keV energy thresholds respectively in the CZT detector

scattering, energy of scattered photons is always greater than the threshold in the secondary pixel (33 keV). However, deposited energy in the primary pixel being less than threshold, Compton events can not give rise to any double pixel events. On the other hand, charge sharing may lead to such an excess of events, since threshold in this case is less than 50% of total charge (i.e. 61 keV for 122 keV photons). With the same argument, the decrease in the excess events for higher thresholds (40 keV and 60 keV) can be explained with the help of charge sharing. These results, therefore, clearly indicate a significant charge sharing for CZT pixels.

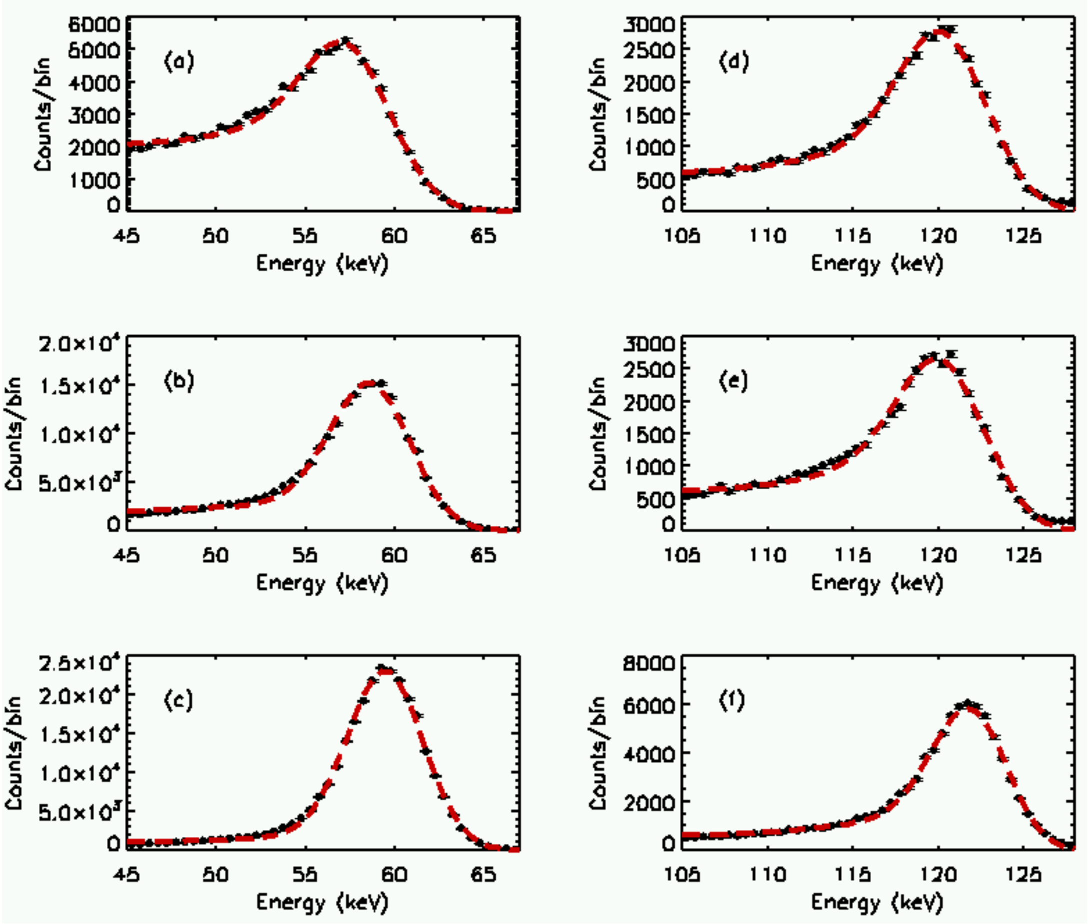

Figure 5.11: Simultaneous fitting of six spectra obtained by illuminating different parts of pixel with a narrow slit. (a)-(c): spectra for ^{241}Am at the left edge (at 0.05 mm from left edge), right edge (at 2.25 mm) and central part (at 1.2 mm) of the pixel respectively. (d)-(f): similar plot for ^{57}Co with slit positions at 0.1 mm from pixel edge, at 2.3 mm and at 1.2 mm respectively. The red dashed line is the fit to the spectra

Since the charge sharing events are contributing to the tail of the CZT lines and tails are expected to be more prominent for interactions closer to the edge of the pixel, to validate our model, we fitted six spectra for three different positions and for two energies simultaneously. Fig. 5.11 shows the simultaneous spectral fitting of six spectra − spectrum of ^{241}Am and ^{57}Co at the left edge, at the right edge and at the center for 133^{rd} pixel. The beam pattern is approximated by Gaussian shape with width tied up across all the six positions while fitting. The Gaussian beam will peak at the slit positions which are kept fixed in the fitting. $\mu\tau$ product depends on the crystal properties and therefore should not change with energy and pixel positions. Therefore, $(\mu\tau)_e$ and $(\mu\tau)_h$ were tied up across all pixel positions and all energies while fitting. Charge sharing fractions are expected to be different, higher at the pixel edges compared to the center, because of contribution from outside the pixel, therefore r_0 values were kept free with positions. The model predicts the line shapes precisely with distance from the pixel edge with acceptable parameter values. This proves that the models are correct and can be used to generate the multipixel response of the CZT detectors. We found the obtained values of r_0 to be higher at the edges of the pixel due to contribution from interpixel area and neighboring pixels as explained earlier and for the same reason, r_0 at central part of the pixel is less compared to that at edges.

5.4 Discussions and Future Plans

In this chapter, we described our CZT line shape model based on charge trapping and charge sharing for 5 mm thick CZT detectors with 2.45 mm × 2.45 mm pixel size. We showed that charge sharing component is absolutely necessary to properly predict the X-ray line shapes. The models have also been verified with extensive experiments. Apart from Astrosat-CZTI, even for future hard X-ray missions with CZT detectors, it is extremely important to generate accurate response matrix for better spectroscopic studies. Our work on the CZT line shape modelling will be extremely helpful in properly characterizing such hard X-ray instruments. This work also demonstrates an alternate way of investigating interpixel charge sharing with optimized experiment setup.

Though the line model properly predicts the line shapes as a function of photon energies quite well, we found that values of r_0 are quite high compared to that expected, which we assume to be because of the charge that is coming from the neighboring pixels and interpixel junction to the pixel under consideration. Since, we do not model the charge coming in from outside a given pixel, overall effect is reflected in the increase in r_0. To demonstrate this, we plan for an experiment where initially only the central part of a pixel is illuminated using a lead plate with a small hole on it. The lead plate has to be kept very close to the detector plane to make sure that only a small part centered at the pixel is illuminated. The center of the pixel can be focussed with the lead plate using a micrometer screw. Use of different lead plates with various hole size ranging from 0.3 mm to 10 mm, will make sure that gradually starting from a small central part of the pixel, the full pixel, and then finally the neighboring pixels are illuminated with the increase in hole size. Spectra from ^{241}Am can be fitted for three different bias voltages to obtain the value of r_0 as a function of hole size. Variation in r_0 with increase in beam radius will help in better understanding of the charge sharing phenomena, specially to quantify the fraction of charge that is coming in from the interpixel area and neighboring pixels.

Finally, we plan to generate pixelwise response matrix from the pixelwise fitted parameters and therefrom a single Redistribution Matrix File (RMF) for the CZT module. The response matrix can be verified by fitting known continuum spectra by illuminating the CZT crystal uniformly using an X-ray gun, which emits bremsstrahlung X-ray photons. At lower energies charge sharing is found to be more significant compared to charge trapping. On the other hand, charge trapping is significant at higher energies. Therefore, it is important to test the response matrix for continuum spectra at both lower energies in $20 - 50$ keV and higher energies $50 - 130$ keV from X-ray gun. It is to be noted that so far, we have not included the effect of escape photons (due to escape of $23 - 31$ keV fluorescence photons from CZT) in the response. We plan to include that in the CZT line model which will make the estimation of response matrix elements more accurate.

Chapter 6

Summary and Scope for Future Work

The thesis summarizes the results on the study of various aspects of X-ray polarimetry in hard X-rays. The dissertation can be broadly divided into two parts where the first part discusses the development of a dedicated Compton polarimeter at the focal plane of a hard X-ray telescope. Followed by a discussion on the scientific potential of hard X-ray polarimetry for celestial X-ray sources and basics of polarization measurements in Chapter 1, Chapter 2 describes the proposed geometric configuration of the polarimeter and estimation of sensitivity of the instrument for NuSTAR kind of hard X-ray optics using Geant$-$4 simulation. It was shown that polarimetric sensitivity critically depends on the lower energy threshold of the active scatterer. Chapter 3 describes the characterization of the plastic scatterer specially for lower energy depositions, and CsI(Tl) absorbers along with the performance of the complete integrated polarimeter for polarized and unpolarized beam of radiation. The CsI(Tl) absorbers are read by Si photomultipliers and we could achieve a threshold $\sim$20 keV for interactions closer to the SiPM. In the polarization experiment, the obtained modulation amplitudes were found to agree quite well with the expected results from simulation. It was found that the lower energy threshold of the polarimeter and overall polarimetric sensitivity critically depends on the choice of inorganic scintillator and SiPM and the coupling between them.

The other part of the thesis discusses the prospects of the hard X-ray polarimetry with Cadmium Zinc Telluride Imager (CZTI) onboard Astrosat, India's first astronomical satellite launched on September 28, 2015. In Chapter 4, we describe the details of Compton polarimetry with CZTI using Geant$-$4 simulation followed by experimental verification of CZTI polarization measurement capability. CZTI will be sensitive to polarimetry measurements at energies beyond 100 keV. Since it is primarily a spectroscopic instrument, CZTI will be capable of measuring polarization only for few bright galactic X-ray sources, e.g. Cygnus X-1, Crab along with any transient events and GRBs.

In Chapter 5, we study the line shapes for monoenergetic X-ray interactions in CZT detectors in CZTI. It was shown that the line shapes from CZT detectors cannot be predicted precisely by charge trapping alone which depends on the mobility μ and lifetime τ of the charge carriers. Charge sharing between the pixels is also significant specially at energies less than $\sim$70 keV. We developed a numerical model based on charge trapping and charge sharing, which predicts the CZT line shapes precisely. The model can be used to generate multipixel response matrix for CZTI onboard Astrosat.

6.1 Scope for Future Work

The dissertation work presented here opens scope for few interesting scientific and technical studies which can be followed up in future.

6.1.1 Solar X-ray polarimeter for future solar missions

Since we have already demonstrated the proof of concept experiment with CXPOL, we explore the possibility of a solar flare polarimeter for future Indian solar missions, e.g. Aditya-1, India's first dedicated solar mission to be launched in 2017-2020. Though the basic configuration is same as the CXPOL, since it is a collimated detector, a plastic scintillator of larger diameter (3 cm) and 5 cm length will be used as scatterer to collect sufficient amount of solar flux for polarimetry observations. The plastic and the surrounding scintillators can be read by multiple SiPMs at both ends which will make the instrument sensitive for Compton spectroscopy as well. The overall sensitivity will depend on the background which is expected to be small, thanks to the active coincidence between scatterer and absorbers. Again, for solar missions the spacecraft will possibly be located at L1 point as in case of Aditya-1. Earth's albedo background, in that case, will be less which makes such an instrument far more optimized for solar flare polarimetry compared to earlier instruments like RHESSI. Preliminary analysis indicates that time resolved polarimetry can be attempted with the instrument for X-class flares with $10 - 120$ sec time binning. It also provides the possibility to measure polarization as a function of observed energy for X-class flares with a binsize of 20 keV.

6.1.2 Simultaneous spectroscopy, timing, imaging and polarimetry

With the advent of high energy focussing telescopes (e.g. NuSTAR, ASTRO-H), it is now possible to design a focal plane Compton polarimeter which can be sensitive upto 80 keV. However, X-ray polarization measurement is extremely photon hungry. Therefore, a dedicated X-ray polarimeter always has lower sensitivity when compared to any other type of X-ray detector for equal collecting area and time exposure. In this context, a new design alternative to CXPOL configuration can be explored for hard X-ray focal plane detector which can provide simultaneous measurements of X-ray polarization along with high resolution X-ray spectroscopy as well as timing and imaging. This design employs a sandwich of a 0.5 mm thick Si detector (SDD) and 10 mm thick plastic or 2 mm thick CZT detector (similar to those used in NuSTAR) which is surrounded by a cylindrical array of scintillator detectors. The plastic can be read by SiPM array making it position sensitive, with spatial resolution depending on the pixel size.

Polarimetric sensitivity of the instrument is expected to be less than that for CXPOL kind of configuration, as scattering efficiency of Si is less. Though polarimetry can be done in various modes e.g. Si-scintillator, Si-plastic/CZT, plastic/CZT-scintillator, overall sensitivity of the instrument derives primarily from the plastic-scintillator mode [100], due to higher Compton scattering efficiency of plastic. Use of CZT will degrade the sensitivity due to interactions of CZT fluorescence photons with scintillator giving rise to false coincidence events.

Being a focal plane detector, the instrument offers high spectroscopic sensitivity due to low background because of narrow FOV of hard X-ray optics. Again, simultaneous events in any of the two detectors can be flagged as background events which will increase the spectroscopic sensitivity further. SDD will provide high resolution spectroscopy in $1 - 30$ keV energy range. Because of low photoelectric efficiency of plastic and poor energy resolution, CZT detector instead of plastic below the SDD will optimize the instrument for sensitive spectroscopic study at higher energies as well, however at the expense of polarimetric sensitivity.

The Compton polarimeter requires both the scatterer and surrounding detectors to operate in event detection mode. Thus timing capabilities are available by default. However, the timing capability will be governed by the number of photons i.e. on collecting area.

At higher energies, both plastic with SiPM array read out and CZT detectors with 0.6 mm pixel size will be capable of imaging the X-ray sources. At lower energies, imaging with the instrument will solely depend on the imaging capability of SDD detectors. True imaging with SDD detectors require development in both architecture of detector geometry and readout electronics. The Multi-Linear SDDs (ML-SDDs) are expected to have fine spatial resolution capability [131]. Further improvement in architecture and detailed simulation and experimental study will be important to optimize SDD detectors for X-ray imaging.

6.1.3 CZTI polarimetry for bright X-ray sources

Astrosat, India's first astronomical satellite has been launched on September 28, 2015. As discussed earlier, CZTI will be capable of doing phase resolved polarimetry of Crab which may help in understanding the X-ray emission mechanisms and emission geometry of the source. Crab will be observed by Astrosat along with NuSTAR, INTEGRAL and few ground based telescopes in optical and infrared wavelength simultaneously during its calibration phase. Since polarization information from CZTI can be obtained from the raw data itself, no change in hardware configuration is required, the polarization data for Crab will be readily available within next few months. CZTI is expected to perform phase resolved polarimetry of Crab in less than 600 ks for 4 phase intervals with 5σ detection significance. We also plan for a simultaneous polarimetry study of Crab by an imaging optical polarimeter from Mt. Abu observatory, India, which along with phase resolved X-ray polarimetry by CZTI may help in complete characterization of the source in the context of emission mechanism by the nebula and Crab pulsar.

Cygnus X-1 is another potential target for CZTI polarimetry. Polarization measurement of Cygnus X-1 by Astrosat-CZTI in $100 - 300$ keV may help in understanding the relative contribution of jet and corona in that energy range. Various existing models on the relative contribution of jet in hard X-rays for Cygnus X-1 can be distinguished with 5 σ significance in $\sim$200 ks time. Cygnus X-1 will be observed simultaneously by many X-ray observatories and ground based telescopes including in radio by GMRT, India, during calibration phase of CZTI. Multiwavelength data from all these instruments along with polarization study with CZTI will help in pinpointing the origin of hard X-ray radiation of Cygnus X-1 beyond 100 keV. As mentioned earlier SGD onboard Astro-H to be launched next year [1] has significant polarization measurement capability in hard X-rays [118]. Polarization measurement of Crab and Cygnus X-1 by SGD would be extremely useful to cross-verify the CZTI polarimetry results in $100 - 300$ keV.

Since CZTI support structure becomes increasingly transparent at energies >100 keV, it is possible to detect transient sources like Gamma Ray Bursts (GRBs) in such large field of view of the detector. So far, for few GRBs, polarization measurements have been done (by RHESSI, INTEGRAL etc.). All these measurements yielded very high polarization. Recently, GAP [69] estimated high polarization for few GRBs [123, 132]. CZTI working in $100 - 300$ keV is

---

[1] According to recent news, after one month of its launch, communication with Astro-H failed on March 26, 2016.

also expected to be sensitive for polarization measurements of GRBs. However, polarimetric sensitivity of CZTI for such off axis sources are expected to differ from that for on axis sources presented in Chapter 4. We plan to develop a complete Geant−4 code to include the full mass model of CZTI including its support structure to explore the prospect of GRB polarimetry with CZTI.

The calibration data of Crab will be used to verify the multipixel response matrix generated for CZTI based on the CZT line model described in Chapter 5. It is to be noted that the double pixel events at energies beyond 100 keV can be used to construct spectra for the bright X-ray sources and therefore providing the opportunity for spectroscopic study in a broad energy band from 20 keV to 300 keV from CZTI.

Bibliography

[1] M. C. Weisskopf, G. G. Cohen, H. L. Kestenbaum, K. S. Long, R. Novick, and R. S. Wolff, *Measurement of the X-ray polarization of the Crab Nebula,* Astrophysical Journal Letter **208**, L125–L128 (1976).

[2] M. C. Weisskopf, E. H. Silver, H. L. Kestenbaum, K. S. Long, and R. Novick, *A precision measurement of the X-ray polarization of the Crab Nebula without pulsar contamination,* Astrophysical Journal Letter **220**, L117–L121 (1978).

[3] J. R. Angel, R. Novick, P. vanden Bout, and R. Wolff, *Search for X-Ray Polarization in Sco X-1,* Physical Review Letters **22**, 861–865 (1969).

[4] R. S. Wolff, J. R. P. Angel, R. Novick, and P. vanden Bout, *Search for Polarization in the X-Ray Emission of the Crab Nebula,* Astrophysical Journal Letter **160**, L21 (1970).

[5] R. Novick, M. C. Weisskopf, R. Berthelsdorf, R. Linke, and R. S. Wolff, *Detection of X-Ray Polarization of the Crab Nebula,* Astrophysical Journal Letter **174**, L1 (1972).

[6] R. E. Griffiths, M. J. Ricketts, and B. A. Cooke, *Observations of the X-ray nova A0620-00 with the Ariel V crystal spectrometer/polarimeter,* MNRAS **177**, 429–440 (1976).

[7] R. A. Gowen, B. A. Cooke, R. E. Griffiths, and M. J. Ricketts, *An upper limit to the linear X-ray polarization of SCO X-1,* MNRAS **179**, 303–310 (1977).

[8] E. H. Silver, M. C. Weisskopf, H. L. Kestenbaum, K. S. Long, R. Novick, and R. S. Wolff, *The first search for X-ray polarization in the Centaurus X-3 and Hercules X-1 pulsars,* Astrophysical Journal **232**, 248–254 (1979).

[9] J. P. Hughes, K. S. Long, and R. Novick, *A search for X-ray polarization in cosmic X-ray sources,* Astrophysical Journal **280**, 255–258 (1984).

[10] J. R. P. Angel and M. C. Weisskopf, *Use of Highly Reflecting Crystals for Spectroscopy and Polarimetry in X-Ray Astronomy,* The Astronomical Journal **75**, 231 (1970).

[11] H. Tsunemi, K. Hayashida, K. Tamura, S. Nomoto, M. Wada, A. Hirano, and E. Miyata, *Detection of X-ray polarization with a charge coupled device,* Nuclear Instruments and Methods in Physics Research A **321**, 629–631 (1992).

[12] R. F. Elsner, B. D. Ramsey, S. L. O'dell, M. Sulkanen, A. F. Tennant, M. C. Weisskopf, S. Gunji, T. Minamitani, R. A. Austin, J. Kolodziejczak, D. Swartz, G. Garmire, P. Meszaros, and G. G. Pavlov, *The X-ray Polarimeter Experiment (XPE),* in "American Astronomical Society Meeting Abstracts #190," , vol. 29 of *Bulletin of the American Astronomical Society* (1997), vol. 29 of *Bulletin of the American Astronomical Society*, p. 790.

[13] H. L. Marshall, S. S. Murray, J. H. Chappell, H. W. Schnopper, E. H. Silver, and M. C. Weisskopf, *Realistic, inexpensive, soft x-ray polarimeter and the potential scientific return,* in "Polarimetry in Astronomy," , vol. 4843 of *Society of Photo-Optical Instrumentation Engineers (SPIE) Conference Series*, S. Fineschi, ed. (2003), vol. 4843 of *Society of Photo-Optical Instrumentation Engineers (SPIE) Conference Series*, pp. 360–371.

[14] P. E. Kaaret, J. Schwartz, P. Soffitta, J. Dwyer, P. S. Shaw, S. Hanany, R. Novick, R. Sunyaev, I. Y. Lapshov, E. H. Silver, K. P. Ziock, M. C. Weisskopf, R. F. Elsner, B. D. Ramsey, E. Costa, A. Rubini, M. Feroci, L. Piro, G. Manzo, S. Giarrusso, A. E. Santangelo, L. Scarsi, G. C. Perola, E. Massaro, and G. Matt, *Status of the stellar x-ray polarimeter for the*

Spectrum-X-Gamma mission, in “X-Ray and Ultraviolet Polarimetry,” , vol. 2010 of *Society of Photo-Optical Instrumentation Engineers (SPIE) Conference Series*, S. Fineschi, ed. (1994), vol. 2010 of *Society of Photo-Optical Instrumentation Engineers (SPIE) Conference Series*, pp. 22–27.

[15] P. Laurent, J. Rodriguez, J. Wilms, M. Cadolle Bel, K. Pottschmidt, and V. Grinberg, *Polarized Gamma-Ray Emission from the Galactic Black Hole Cygnus X-1,* Science **332**, 438– (2011).

[16] E. Jourdain, J. P. Roques, M. Chauvin, and D. J. Clark, *Separation of Two Contributions to the High Energy Emission of Cygnus X-1: Polarization Measurements with INTEGRAL SPI,* Astrophysical Journal **761**, 27 (2012).

[17] M. Forot, P. Laurent, I. A. Grenier, C. Gouiffès, and F. Lebrun, *Polarization of the Crab Pulsar and Nebula as Observed by the INTEGRAL/IBIS Telescope,* Astrophysical Journal Letter **688**, L29–L32 (2008).

[18] A. J. Dean, D. J. Clark, J. B. Stephen, V. A. McBride, L. Bassani, A. Bazzano, A. J. Bird, A. B. Hill, S. E. Shaw, and P. Ubertini, *Polarized Gamma-Ray Emission from the Crab,* Science **321**, 1183– (2008).

[19] F. Lei, A. J. Dean, and G. L. Hills, *Compton Polarimetry in Gamma-Ray Astronomy,* Space Science Reviews **82**, 309–388 (1997).

[20] P. Soffitta, *X-ray polarimetry an almost new frontier for X-ray astronomy,* in “Ital. Phys. Soc. Conf. Ser. 57: Frontier Objects in Astrophysics and Particle Physics,” , F. Giovannelli and G. Mannocchi, eds. (1997), p. 561.

[21] H. Krawczynski, A. Garson, Q. Guo, M. G. Baring, P. Ghosh, M. Beilicke, and K. Lee, *Scientific prospects for hard X-ray polarimetry,* Astroparticle Physics **34**, 550–567 (2011).

[22] M. Dovčiak, F. Muleri, R. W. Goosmann, V. Karas, and G. Matt, *Thermal disc emission from a rotating black hole: X-ray polarization signatures,* MNRAS **391**, 32–38 (2008).

[23] J. D. Schnittman and J. H. Krolik, *X-ray Polarization from Accreting Black Holes: The Thermal State,* **701**, 1175–1187 (2009).

[24] J. D. Schnittman and J. H. Krolik, *X-ray Polarization from Accreting Black Holes: Coronal Emission,* Astrophysical Journal **712**, 908–924 (2010).

[25] S. V. Vadawale, A. R. Rao, and S. K. Chakrabarti, *Spectral differences between the radio-loud and radio-quiet low-hard states of GRS 1915+105: Possible detection of synchrotron radiation in X-rays,* Astronomy & Astrophysics **372**, 793–802 (2001).

[26] S. V. Vadawale, A. R. Rao, S. Naik, J. S. Yadav, C. H. Ishwara-Chandra, A. Pramesh Rao, and G. G. Pooley, *On the Origin of the Various Types of Radio Emission in GRS 1915+105,* Astrophysical Journal **597**, 1023–1035 (2003).

[27] S. Markoff, H. Falcke, and R. Fender, *A jet model for the broadband spectrum of XTE J1118+480. Synchrotron emission from radio to X-rays in the Low/Hard spectral state,* Astronomy & Astrophysics **372**, L25–L28 (2001).

[28] A. A. Zdziarski, P. Pjanka, M. Sikora, and Ł. Stawarz, *Jet contributions to the broad-band spectrum of Cyg X-1 in the hard state,* MNRAS **442**, 3243–3255 (2014).

[29] G. E. Romero, F. L. Vieyro, and S. Chaty, *Coronal origin of the polarization of the high-energy emission of Cygnus X-1,* Astronomy & Astrophysics **562**, L7 (2014).

[30] R. W. Goosmann and G. Matt, *Spotting the misaligned outflows in NGC 1068 using X-ray polarimetry,* MNRAS **415**, 3119–3128 (2011).

[31] P. Uttley, E. M. Cackett, A. C. Fabian, E. Kara, and D. R. Wilkins, *X-ray reverberation around accreting black holes,* **22**, 72 (2014).

[32] A. Celotti and G. Matt, *Polarization Properties of Synchrotron Self-Compton Emission,* MNRAS **268**, 451 (1994).

[33] A. L. McNamara, Z. Kuncic, and K. Wu, *X-ray polarization in relativistic jets,* MNRAS **395**, 1507–1514 (2009).

[34] H. Zhang and M. Böttcher, *X-Ray and Gamma-Ray Polarization in Leptonic and Hadronic Jet Models of Blazars,* Astrophysical Journal **774**, 18 (2013).

[35] M. C. Weisskopf, R. F. Elsner, D. Hanna, V. M. Kaspi, S. L. O'Dell, G. G. Pavlov, and B. D. Ramsey, *The prospects for X-ray polarimetry and its potential use for understanding neutron stars,* ArXiv Astrophysics e-prints (2006).

[36] J. K. Daugherty and A. K. Harding, *Electromagnetic cascades in pulsars,* Astrophysical Journal **252**, 337–347 (1982).

[37] K. S. Cheng, M. Ruderman, and L. Zhang, *A Three-dimensional Outer Magnetospheric Gap Model for Gamma-Ray Pulsars: Geometry, Pair Production, Emission Morphologies, and Phase-resolved Spectra,* Astrophysical Journal **537**, 964–976 (2000).

[38] J. Dyks and B. Rudak, *Two-Pole Caustic Model for High-Energy Light Curves of Pulsars,* Astrophysical Journal **598**, 1201–1206 (2003).

[39] F. G. Smith, D. H. P. Jones, J. S. B. Dick, and C. D. Pike, *The optical polarization of the Crab Pulsar,* MNRAS **233**, 305–319 (1988).

[40] R. W. Romani, A. J. Miller, B. Cabrera, S. W. Nam, and J. M. Martinis, *Phase-resolved Crab Studies with a Cryogenic Transition-Edge Sensor Spectrophotometer,* Astrophysical Journal **563**, 221–228 (2001).

[41] R. C. Duncan and C. Thompson, *Formation of very strongly magnetized neutron stars - Implications for gamma-ray bursts,* Astrophysical Journal Letter **392**, L9–L13 (1992).

[42] P. Meszaros, R. Novick, A. Szentgyorgyi, G. A. Chanan, and M. C. Weisskopf, *Astrophysical implications and observational prospects of X-ray polarimetry,* Astrophysical Journal **324**, 1056–1067 (1988).

[43] K. Viironen and J. Poutanen, *Light curves and polarization of accretion- and nuclear-powered millisecond pulsars,* Astronomy & Astrophysics **426**, 985–997 (2004).

[44] S. Y. Sazonov and R. A. Sunyaev, *Scattering in the inner accretion disk and the waveforms and polarization of millisecond flux oscillations in LMXBs,* Astronomy & Astrophysics **373**, 241–250 (2001).

[45] K. Toma, T. Sakamoto, B. Zhang, J. E. Hill, M. L. McConnell, P. F. Bloser, R. Yamazaki, K. Ioka, and T. Nakamura, *Statistical Properties of Gamma-Ray Burst Polarization,* Astrophysical Journal **698**, 1042–1053 (2009).

[46] M. Lyutikov, V. I. Pariev, and R. D. Blandford, *Polarization of Prompt Gamma-Ray Burst Emission: Evidence for Electromagnetically Dominated Outflow,* Astrophysical Journal **597**, 998–1009 (2003).

[47] M. Lyutikov and R. Blandford, *Gamma Ray Bursts as Electromagnetic Outflows,* ArXiv:0312347 (2003).

[48] A. G. Emslie and J. C. Brown, *The polarization and directivity of solar-flare hard X-ray bremsstrahlung from a thermal source,* Astrophysical Journal **237**, 1015–1023 (1980).

[49] N. L. S. Jeffrey and E. P. Kontar, *Spatially resolved hard X-ray polarization in solar flares: effects of Compton scattering and bremsstrahlung,* Astronomy & Astrophysics **536**, A93 (2011).

[50] V. V. Zharkova, A. A. Kuznetsov, and T. V. Siversky, *Diagnostics of energetic electrons with anisotropic distributions in solar flares. I. Hard X-rays bremsstrahlung emission,* Astronomy & Astrophysics **512**, A8 (2010).

[51] P. Kaaret, *X-Ray Polarimetry,* arXiv:1408.5899 (2014).

[52] W. Heitler, *Quantum theory of radiation,* in "International Series of Monographs on Physics, Oxford: Clarendon, 1954, 3rd ed.", (1954).

[53] X. Llopart, R. Ballabriga, M. Campbell, L. Tlustos, and W. Wong, *Timepix, a 65k programmable pixel readout chip for arrival time, energy and/or photon counting measurements,* Nuclear Instruments and Methods in Physics Research A **581**, 485–494 (2007).

[54] T. Michel and J. Durst, *Evaluation of a hybrid photon counting pixel detector for x-ray polarimetry,* Nuclear Instruments and Methods in Physics Research Section A: Accelerators, Spectrometers, Detectors and Associated Equipment **594**, 188 – 195 (2008).

[55] F. Sauli, *GEM: A new concept for electron amplification in gas detectors,* Nuclear Instruments and Methods in Physics Research A **386**, 531–534 (1997).

[56] E. Costa, P. Soffitta, R. Bellazzini, A. Brez, N. Lumb, and G. Spandre, *An efficient photoelectric X-ray polarimeter for the study of black holes and neutron stars,* Nature **411**, 662–665 (2001).

[57] R. Bellazzini, F. Angelini, L. Baldini, F. Bitti, A. Brez, F. Cavalca, M. Del Prete, M. Kuss, L. Latronico, N. Omodei, M. Pinchera, M. M. Massai, M. Minuti, M. Razzano, C. Sgro, G. Spandre, A. Tenze, E. Costa, and P. Soffitta, *Gas pixel detectors for X-ray polarimetry applications,* Nuclear Instruments and Methods in Physics Research A **560**, 425–434 (2006).

[58] R. Bellazzini, G. Spandre, M. Minuti, L. Baldini, A. Brez, L. Latronico, N. Omodei, M. Razzano, M. M. Massai, M. Pesce-Rollins, C. Sgró, E. Costa, P. Soffitta, H. Sipila, and E. Lempinen, *A sealed Gas Pixel Detector for X-ray astronomy,* Nuclear Instruments and Methods in Physics Research A **579**, 853–858 (2007).

[59] J. K. Black, R. G. Baker, P. Deines-Jones, J. E. Hill, and K. Jahoda, *X-ray polarimetry with a micropattern TPC,* Nuclear Instruments and Methods in Physics Research A **581**, 755–760 (2007).

[60] J. R. Toraskar, *Focusing crystal polarimeter designed for X-ray polarimetry - Construction and performance,* Applied Optics **14**, 1727–1735 (1975).

[61] R. Novick, *Stellar and Solar X-Ray Polarimetry,* Space Science Reviews **18**, 389–408 (1975).

[62] E. Silver, J. Holley, K. Ziock, R. Novick, P. Kaaret, M. Weisskopf, and R. Elsner, *Bragg crystal polarimeters,* Optical Engineering **29**, 759–766 (1990).

[63] H. W. Schnopper and K. Kalata, *Polarimeter for Celestial X Rays,* **74**, 854 (1969).

[64] E. Costa, R. Bellazzini, G. Tagliaferri, G. Matt, A. Argan, P. Attinà, L. Baldini, S. Basso, A. Brez, O. Citterio, S. di Cosimo, V. Cotroneo, S. Fabiani, M. Feroci, A. Ferri, L. Latronico, F. Lazzarotto, M. Minuti, E. Morelli, F. Muleri, L. Nicolini, G. Pareschi, G. di Persio, M. Pinchera, M. Razzano, L. Reboa, A. Rubini, A. M. Salonico, C. Sgro', P. Soffitta, G. Spandre, D. Spiga, and A. Trois, *POLARIX: a pathfinder mission of X-ray polarimetry,* Experimental Astronomy **28**, 137–183 (2010).

[65] G. Tagliaferri, A. Argan, R. Bellazzini, J. Bookbinder, O. Catalano, E. Cavazzuti, E. Costa, G. Cusumano, F. Fiore, C. Fiorini, P. Giommi, G. Malaguti, G. Matt, S. Mereghetti, G. Micela, S. Murray, B. Negri, G. Pareschi, G. Perola, S. Romaine, and G. Villa, *NHXM: a New Hard X-ray imaging and polarimetric Mission,* in "Society of Photo-Optical Instrumentation Engineers (SPIE) Conference Series," , vol. 7732 of *Society of Photo-Optical Instrumentation Engineers (SPIE) Conference Series* (2010), vol. 7732 of *Society of Photo-Optical Instrumentation Engineers (SPIE) Conference Series*, p. 17.

[66] K. Jahoda, *The Gravity and Extreme Magnetism Small Explorer,* in "Society of Photo-Optical Instrumentation Engineers (SPIE) Conference Series," , vol. 7732 of *Society of Photo-Optical Instrumentation Engineers (SPIE) Conference Series* (2010), vol. 7732 of *Society of Photo-Optical Instrumentation Engineers (SPIE) Conference Series.*

[67] R. Bellazzini and et al., *A polarimeter for IXO,* in "X-ray Polarimetry: A New Window in Astrophysics by Ronaldo Bellazzini, Enrico Costa, Giorgio Matt and Gianpiero Tagliaferri. Cambridge University Press, 2010. ISBN: 9780521191845, p. 269," , R. Bellazzini, E. Costa, G. Matt, and G. Tagliaferri, eds. (2010), p. 269.

[68] P. Soffitta, X. Barcons, R. Bellazzini, J. Braga, E. Costa, G. W. Fraser, S. Gburek, J. Huovelin, G. Matt, M. Pearce, J. Poutanen, V. Reglero, A. Santangelo, R. A. Sunyaev, G. Tagliaferri, M. Weisskopf, R. Aloisio, E. Amato, P. Attiná, M. Axelsson, L. Baldini, S. Basso, S. Bianchi, P. Blasi, J. Bregeon, A. Brez, N. Bucciantini, L. Burderi, V. Burwitz, P. Casella, E. Churazov, M. Civitani, S. Covino, R. M. Curado da Silva, G. Cusumano, M. Dadina, F. D'Amico, A. De Rosa, S. Di Cosimo, G. Di Persio, T. Di Salvo, M. Dovciak, R. Elsner, C. J. Eyles, A. C. Fabian, S. Fabiani, H. Feng, S. Giarrusso, R. W. Goosmann, P. Grandi, N. Grosso, G. Israel, M. Jackson, P. Kaaret, V. Karas, M. Kuss, D. Lai, G. L. Rosa, J. Larsson, S. Larsson, L. Latronico, A. Maggio, J. Maia, F. Marin, M. M. Massai, T. Mineo, M. Minuti, E. Moretti, F. Muleri, S. L. O'Dell, G. Pareschi, G. Peres, M. Pesce, P.-O. Petrucci, M. Pinchera, D. Porquet, B. Ramsey, N. Rea, F. Reale, J. M. Rodrigo, A. Różańska, A. Rubini, P. Rudawy, F. Ryde, M. Salvati, V. A. de Santiago, S. Sazonov, C. Sgró, E. Silver, G. Spandre, D. Spiga, L. Stella, T. Tamagawa, F. Tamborra, F. Tavecchio, T. Teixeira Dias, M. van Adelsberg, K. Wu, and S. Zane, *XIPE: the X-ray imaging polarimetry explorer,* Experimental Astronomy **36**, 523–567 (2013).

[69] D. Yonetoku, T. Murakami, H. Masui, H. Kodaira, Y. Aoyama, S. Gunji, F. Tokanai, and T. Mihara, *Development of polarimeter for gamma-ray bursts onboard the solar-powered sail mission,* in "Society of Photo-Optical Instrumentation Engineers (SPIE) Conference Series," , vol. 6266 of *Society of Photo-Optical Instrumentation Engineers (SPIE) Conference Series* (2006), vol. 6266 of *Society of Photo-Optical Instrumentation Engineers (SPIE) Conference Series.*

[70] Y. Kishimoto, S. Gunji, Y. Ishigaki, M. Kanno, H. Murayama, C. Ito, F. Tokanai, K. Suzuki, H. Sakurai, T. Mihara, M. Kohama, M. Suzuki, A. Hayato, K. Hayashida, N. Anabuki, M. Morimoto, H. Tsunemi, Y. Saito, T. Yamagami, and S. Kishimoto, *Basic Performance of PHENEX: A Polarimeter for High ENErgy X rays,* IEEE Transactions on Nuclear Science **54**, 561–566 (2007).

[71] T. Kamae, V. Andersson, M. Arimoto, M. Axelsson, C. Marini Bettolo, C.-I. Björnsson, G. Bogaert, P. Carlson, W. Craig, T. Ekeberg, O. Engdegård, Y. Fukazawa, S. Gunji, L. Hjalmarsdotter, B. Iwan, Y. Kanai, J. Kataoka, N. Kawai, J. Kazejev, M. Kiss, W. Klamra, S. Larsson, G. Madejski, T. Mizuno, J. Ng, M. Pearce, F. Ryde, M. Suhonen, H. Tajima, H. Takahashi, T. Takahashi, T. Tanaka, T. Thurston, M. Ueno, G. Varner, K. Yamamoto, Y. Yamashita, T. Ylinen, and H. Yoshida, *PoGOLite A high sensitivity balloon-borne soft gamma-ray polarimeter,* Astroparticle Physics **30**, 72–84 (2008).

[72] P. F. Bloser, J. S. Legere, M. L. McConnell, J. R. Macri, C. M. Bancroft, T. P. Connor, and J. M. Ryan, *Calibration of the Gamma-RAy Polarimeter Experiment (GRAPE) at a polarized hard X-ray beam,* Nuclear Instruments and Methods in Physics Research A **600**, 424–433 (2009).

[73] S. Orsi and Polar Collaboration, *POLAR: A Space-borne X-Ray Polarimeter for Transient Sources,* Astrophysics and Space Sciences Transactions **7**, 43–47 (2011).

[74] F. A. Harrison, F. E. Christensen, W. Craig, C. Hailey, W. Baumgartner, C. M. H. Chen, J. Chonko, W. R. Cook, J. Koglin, K.-K. Madsen, M. Pivavoroff, S. Boggs, and D. Smith, *Development of the HEFT and NuSTAR focusing telescopes,* Experimental Astronomy **20**, 131–137 (2005).

[75] H. Kunieda, H. Awaki, A. Furuzawa, Y. Haba, R. Iizuka, K. Ishibashi, M. Ishida, M. Itoh, T. Kosaka, Y. Maeda, H. Matsumoto, T. Miyazawa, H. Mori, Y. Namba, Y. Ogasaka, K. Ogi, T. Okajima, Y. Suzuki,

K. Tamura, Y. Tawara, K. Uesugi, K. Yamashita, and S. Yamauchi, *Hard x-ray telescope to be onboard ASTRO-H,* in "Society of Photo-Optical Instrumentation Engineers (SPIE) Conference Series," , vol. 7732 of *Society of Photo-Optical Instrumentation Engineers (SPIE) Conference Series* (2010), vol. 7732 of *Society of Photo-Optical Instrumentation Engineers (SPIE) Conference Series.*

[76] M. Beilicke, F. Kislat, A. Zajczyk, Q. Guo, R. Endsley, M. Stork, R. Cowsik, P. Dowkontt, S. Barthelmy, T. Hams, T. Okajima, M. Sasaki, B. Zeiger, G. de Geronimo, M. G. Baring, and H. Krawczynski, *Design and Performance of the X-ray Polarimeter X-Calibur,* Journal of Astronomical Instrumentation **3**, 1440008 (2014).

[77] K. Hayashida, D. Yonetoku, S. Gunji, T. Tamagawa, T. Mihara, T. Mizuno, H. Takahashi, T. Dotani, H. Kubo, Y. Yatsu, F. Tokanai, T. Nakamori, S. Shibata, A. Hayato, A. Furuzawa, Y. Kishimoto, S. Kitamoto, K. Toma, M. Sadamoto, K. Yoshinaga, J. Kim, S. Ide, F. Kamitsukasa, N. Anabuki, H. Tsunemi, J. Katagiri, and J. Sugimoto, *X-ray gamma-ray polarimetry small satellite PolariS,* in "Society of Photo-Optical Instrumentation Engineers (SPIE) Conference Series," , vol. 9144 of *Society of Photo-Optical Instrumentation Engineers (SPIE) Conference Series* (2014), vol. 9144 of *Society of Photo-Optical Instrumentation Engineers (SPIE) Conference Series*, p. 0.

[78] Y. Yatsu, K. Ito, S. Kurita, M. Arimoto, N. Kawai, M. Matsushita, S. Kawajiri, S. Kitamura, S. Matunaga, S. Kimura, J. Kataoka, T. Nakamori, and S. Kubo, *Pre-flight performance of a micro-satellite TSUBAME for X-ray polarimetry of gamma-ray bursts,* in "Society of Photo-Optical Instrumentation Engineers (SPIE) Conference Series," , vol. 9144 of *Society of Photo-Optical Instrumentation Engineers (SPIE) Conference Series* (2014), vol. 9144 of *Society of Photo-Optical Instrumentation Engineers (SPIE) Conference Series*, p. 0.

[79] M. L. McConnell, J. M. Ryan, D. M. Smith, R. P. Lin, and A. G. Emslie, *RHESSI as a Hard X-Ray Polarimeter,* Solar Physics **210**, 125–142 (2002).

[80] W. Coburn and S. E. Boggs, *Polarization of the prompt γ-ray emission from the γ-ray burst of 6 December 2002,* Nature **423**, 415–417 (2003).

[81] P. Moran, A. Shearer, C. Gouiffes, and P. Laurent, *INTEGRAL/IBIS and optical observations of the Crab nebula/pulsar polarisation,* ArXiv e-prints (2013).

[82] D. Götz, P. Laurent, F. Lebrun, F. Daigne, and Ž. Bošnjak, *Variable Polarization Measured in the Prompt Emission of GRB 041219A Using IBIS on Board INTEGRAL,* Astrophysical Journal Letter **695**, L208–L212 (2009).

[83] D. Götz, S. Covino, A. Fernández-Soto, P. Laurent, and Ž. Bošnjak, *The polarized gamma-ray burst GRB 061122,* MNRAS **431**, 3550–3556 (2013).

[84] S. McGlynn, D. J. Clark, A. J. Dean, L. Hanlon, S. McBreen, D. R. Willis, B. McBreen, A. J. Bird, and S. Foley, *Polarisation studies of the prompt gamma-ray emission from GRB 041219a using the spectrometer aboard INTEGRAL,* Astronomy & Astrophysics **466**, 895–904 (2007).

[85] S. McGlynn, S. Foley, B. McBreen, L. Hanlon, S. McBreen, D. J. Clark, A. J. Dean, A. Martin-Carrillo, and R. O'Connor, *High energy emission and polarisation limits for the INTEGRAL burst GRB 061122,* Astronomy & Astrophysics **499**, 465–472 (2009).

[86] R. E. Rutledge and D. B. Fox, *Re-analysis of polarization in the γ-ray flux of GRB 021206,* MNRAS **350**, 1288–1300 (2004).

[87] C. Wigger, W. Hajdas, K. Arzner, M. Güdel, and A. Zehnder, *Gamma-Ray Burst Polarization: Limits from RHESSI Measurements,* Astrophysical Journal **613**, 1088–1100 (2004).

[88] P. C. Agrawal, *A broad spectral band Indian Astronomy satellite 'Astrosat',* Advances in Space Research **38**, 2989–2994 (2006).

[89] K. P. Singh, S. N. Tandon, P. C. Agrawal, H. M. Antia, R. K. Manchanda, J. S. Yadav, S. Seetha, M. C. Ramadevi, A. R. Rao, D. Bhattacharya, B. Paul, P. Sreekumar, S. Bhattacharyya, G. C. Stewart, J. Hutchings, S. A. Annapurni, S. K. Ghosh, J. Murthy, A. Pati, N. K. Rao, C. S. Stalin, V. Girish, K. Sankarasubramanian, S. Vadawale, V. B. Bhalerao, G. C. Dewangan, D. K. Dedhia, M. K. Hingar, T. B. Katoch, A. T. Kothare, I. Mirza, K. Mukerjee, H. Shah, P. Shah, R. Mohan, A. K. Sangal, S. Nagabhusana, S. Sriram, J. P. Malkar, S. Sreekumar, A. F. Abbey, G. M. Hansford, A. P. Beardmore, M. R. Sharma, S. Murthy, R. Kulkarni, G. Meena, V. C. Babu, and J. Postma, *ASTROSAT mission,* in "Society of Photo-Optical Instrumentation Engineers (SPIE) Conference Series," , vol. 9144 of *Society of Photo-Optical Instrumentation Engineers (SPIE) Conference Series* (2014), vol. 9144 of *Society of Photo-Optical Instrumentation Engineers (SPIE) Conference Series.*

[90] S. V. Vadawale, J. S. Hong, J. E. Grindlay, P. Williams, M. Zhang, E. C. Bellm, T. Narita, W. W. Craig, B. H. Parker, C. M. Stahle, and F. Yan, *Multipixel characterization of imaging CZT detectors for hard x-ray imaging and spectroscopy,* in "Hard X-Ray and Gamma-Ray Detector Physics VI," , vol. 5540 of *Society of Photo-Optical Instrumentation Engineers (SPIE) Conference Series*, A. Burger, R. B. James, and L. A. Franks, eds. (2004), vol. 5540 of *Society of Photo-Optical Instrumentation Engineers (SPIE) Conference Series*, pp. 22–32.

[91] S. V. Vadawale, S. Purohit, M. Shanmugam, Y. B. Acharya, J. N. Goswami, M. Sudhakar, and P. Sreekumar, *Characterization and selection of CZT detector modules for HEX experiment onboard Chandrayaan-1,* Nuclear Instruments and Methods in Physics Research A **598**, 485–495 (2009).

[92] A. Nandi, S. Palit, D. Debnath, S. K. Chakrabarti, T. B. Kotoch, R. Sarkar, V. K. Yadav, V. Girish, A. R. Rao, and D. Bhattacharya, *Instruments of RT-2 experiment onboard CORONAS-PHOTON and their test and eval-*

uation III: Coded Aperture Mask and Fresnel Zone Plates in RT-2/CZT payload, Experimental Astronomy **29**, 55–84 (2011).

[93] F. A. Harrison, W. W. Craig, F. E. Christensen, C. J. Hailey, W. W. Zhang, S. E. Boggs, D. Stern, W. R. Cook, K. Forster, P. Giommi, B. W. Grefenstette, Y. Kim, T. Kitaguchi, J. E. Koglin, K. K. Madsen, P. H. Mao, H. Miyasaka, K. Mori, M. Perri, M. J. Pivovaroff, S. Puccetti, V. R. Rana, N. J. Westergaard, J. Willis, A. Zoglauer, H. An, M. Bachetti, N. M. Barrière, E. C. Bellm, V. Bhalerao, N. F. Brejnholt, F. Fuerst, C. C. Liebe, C. B. Markwardt, M. Nynka, J. K. Vogel, D. J. Walton, D. R. Wik, D. M. Alexander, L. R. Cominsky, A. E. Hornschemeier, A. Hornstrup, V. M. Kaspi, G. M. Madejski, G. Matt, S. Molendi, D. M. Smith, J. A. Tomsick, M. Ajello, D. R. Ballantyne, M. Baloković, D. Barret, F. E. Bauer, R. D. Blandford, W. N. Brandt, L. W. Brenneman, J. Chiang, D. Chakrabarty, J. Chenevez, A. Comastri, F. Dufour, M. Elvis, A. C. Fabian, D. Farrah, C. L. Fryer, E. V. Gotthelf, J. E. Grindlay, D. J. Helfand, R. Krivonos, D. L. Meier, J. M. Miller, L. Natalucci, P. Ogle, E. O. Ofek, A. Ptak, S. P. Reynolds, J. R. Rigby, G. Tagliaferri, S. E. Thorsett, E. Treister, and C. M. Urry, *The Nuclear Spectroscopic Telescope Array (NuSTAR) High-energy X-Ray Mission,* Astrophysical Journal **770**, 103 (2013).

[94] S. V. Vadawale, B. Paul, J. Pendharkar, and S. Naik, *Comparative study of different scattering geometries for the proposed Indian X-ray polarization measurement experiment using Geant4,* Nuclear Instruments and Methods in Physics Research A **618**, 182–189 (2010).

[95] Q. Guo, M. Beilicke, A. Garson, F. Kislat, D. Fleming, and H. Krawczynski, *Optimization of the design of the hard X-ray polarimeter X-Calibur,* Astroparticle Physics **41**, 63–72 (2013).

[96] S. Agostinelli, J. Allison, K. Amako, J. Apostolakis, H. Araujo, P. Arce, M. Asai, D. Axen, S. Banerjee, G. Barrand, F. Behner, L. Bellagamba, J. Boudreau, L. Broglia, A. Brunengo, H. Burkhardt, S. Chauvie, J. Chuma, R. Chytracek, G. Cooperman, G. Cosmo, P. Degtyarenko, A. Dell'Acqua,

G. Depaola, D. Dietrich, R. Enami, A. Feliciello, C. Ferguson, H. Fesefeldt, G. Folger, F. Foppiano, A. Forti, S. Garelli, S. Giani, R. Giannitrapani, D. Gibin, J. J. Gómez Cadenas, I. González, G. Gracia Abril, G. Greeniaus, W. Greiner, V. Grichine, A. Grossheim, S. Guatelli, P. Gumplinger, R. Hamatsu, K. Hashimoto, H. Hasui, A. Heikkinen, A. Howard, V. Ivanchenko, A. Johnson, F. W. Jones, J. Kallenbach, N. Kanaya, M. Kawabata, Y. Kawabata, M. Kawaguti, S. Kelner, P. Kent, A. Kimura, T. Kodama, R. Kokoulin, M. Kossov, H. Kurashige, E. Lamanna, T. Lampén, V. Lara, V. Lefebure, F. Lei, M. Liendl, W. Lockman, F. Longo, S. Magni, M. Maire, E. Medernach, K. Minamimoto, P. Mora de Freitas, Y. Morita, K. Murakami, M. Nagamatu, R. Nartallo, P. Nieminen, T. Nishimura, K. Ohtsubo, M. Okamura, S. O'Neale, Y. Oohata, K. Paech, J. Perl, A. Pfeiffer, M. G. Pia, F. Ranjard, A. Rybin, S. Sadilov, E. Di Salvo, G. Santin, T. Sasaki, N. Savvas, Y. Sawada, S. Scherer, S. Sei, V. Sirotenko, D. Smith, N. Starkov, H. Stoecker, J. Sulkimo, M. Takahata, S. Tanaka, E. Tcherniaev, E. Safai Tehrani, M. Tropeano, P. Truscott, H. Uno, L. Urban, P. Urban, M. Verderi, A. Walkden, W. Wander, H. Weber, J. P. Wellisch, T. Wenaus, D. C. Williams, D. Wright, T. Yamada, H. Yoshida, D. Zschiesche, and G EANT4 Collaboration, *GEANT–4, a simulation toolkit,* Nuclear Instruments and Methods in Physics Research A **506**, 250–303 (2003).

[97] F. A. Harrison, S. Boggs, F. Christensen, W. Craig, C. Hailey, D. Stern, W. Zhang, L. Angelini, H. An, V. Bhalerao, N. Brejnholt, L. Cominsky, W. R. Cook, M. Doll, P. Giommi, B. Grefenstette, A. Hornstrup, V. Kaspi, Y. Kim, T. Kitaguchi, J. Koglin, C. C. Liebe, G. Madejski, K. Kruse Madsen, P. Mao, D. Meier, H. Miyasaka, K. Mori, M. Perri, M. Pivovaroff, S. Puccetti, V. Rana, and A. Zoglauer, *The Nuclear Spectroscopic Telescope Array (NuSTAR),* in "Society of Photo-Optical Instrumentation Engineers (SPIE) Conference Series," , vol. 7732 of *Society of Photo-Optical Instrumentation Engineers (SPIE) Conference Series* (2010), vol. 7732 of *Society of Photo-Optical Instrumentation Engineers (SPIE) Conference Series*, p. 0.

[98] M. Türler, M. Chernyakova, T. J.-L. Courvoisier, P. Lubiński, A. Neronov, N. Produit, and R. Walter, *INTEGRAL hard X-ray spectra of the cosmic X-ray background and Galactic ridge emission,* Astronomy & Astrophysics **512**, A49 (2010).

[99] J. Katsuta, T. Mizuno, Y. Ogasaka, H. Yoshida, H. Takahashi, Y. Kano, T. Iwahara, N. Sasaki, T. Kamae, M. Kokubun, T. Takahashi, K. Hayashida, and K. Uesugi, *Evaluation of polarization characteristics of multilayer mirror for hard X-ray observation of astrophysical objects,* Nuclear Instruments and Methods in Physics Research A **603**, 393–400 (2009).

[100] S. V. Vadawale, T. Chattopadhyay, and J. Pendharkar, *A conceptual design of hard X-ray focal plane detector for simultaneous x-ray polarimetric, spectroscopic, and timing measurements,* in "Society of Photo-Optical Instrumentation Engineers (SPIE) Conference Series," , vol. 8443 of *Society of Photo-Optical Instrumentation Engineers (SPIE) Conference Series* (2012), vol. 8443 of *Society of Photo-Optical Instrumentation Engineers (SPIE) Conference Series.*

[101] M. C. Weisskopf, R. F. Elsner, and S. L. O'Dell, *On understanding the figures of merit for detection and measurement of x-ray polarization,* in "Society of Photo-Optical Instrumentation Engineers (SPIE) Conference Series," , vol. 7732 of *Society of Photo-Optical Instrumentation Engineers (SPIE) Conference Series* (2010), vol. 7732 of *Society of Photo-Optical Instrumentation Engineers (SPIE) Conference Series.*

[102] S. Fabiani, R. Campana, E. Costa, E. Del Monte, F. Muleri, A. Rubini, and P. Soffitta, *Characterization of scatterers for an active focal plane Compton polarimeter,* Astroparticle Physics **44**, 91–101 (2013).

[103] R. H. Redus, A. Huber, J. Pantazis, and D. Sperry, *Design and performance of the X-123 compact X-ray and Gamma-ray spectroscopy system,* in "IEEE Nucl. Sci. Symp. Conf. Rec., R15-4," (2006), IEEE Nucl. Sci. Symp. Conf. Rec., R15-4.

[104] F. Muleri and R. Campana, *Sensitivity of Stacked Imaging Detectors to Hard X-Ray Polarization,* Astrophysical Journal **751**, 88 (2012).

[105] J. H. Hubbell, W. J. Veigele, E. A. Briggs, R. T. Brown, D. T. Cromer, and R. J. Howerton, *Atomic form factors, incoherent scattering functions, and photon scattering cross sections,* Journal of Physical and Chemical Reference Data **4**, 471–538 (1975).

[106] M. J. Berger and J. H. Hubbell, *XCOM: Photon Cross Sections Database,* in "NBSIR 87-3597, National Bureau of Standards (former name of NIST), Gaithersburg, MD (1987)," (1987).

[107] P. Buzhan, B. Dolgoshein, A. Ilyin, V. Kantserov, V. Kaplin, A. Karakash, A. Pleshko, E. Popova, S. Smirnov, Y. Volkov, L. Filatov, S. Klemin, and F. Kayumov, *The Advanced Study of Silicon Photomultiplier,* in "Advanced Technology - Particle Physics," , M. Barone, E. Borchi, J. Huston, C. Leroy, P. G. Rancoita, P. Riboni, and R. Ruchti, eds. (2002), pp. 717–728.

[108] P. Buzhan, B. Dolgoshein, L. Filatov, A. Ilyin, V. Kantzerov, V. Kaplin, A. Karakash, F. Kayumov, S. Klemin, E. Popova, and S. Smirnov, *Silicon photomultiplier and its possible applications,* Nuclear Instruments and Methods in Physics Research A **504**, 48–52 (2003).

[109] N. Otte, *The Silicon Photomultiplier-a new device for high energy physics, astroparticle physics, industrial and medical applications,* in "IX International Symposium on Detectors for Particle, Astroparticle and Synchrotron Radiation Experiments, SNIC Symposium, Stanford, California," (2006), pp. 1–9.

[110] P. F. Bloser, J. Legere, C. Bancroft, M. L. McConnell, J. M. Ryan, and N. Schwadron, *Scintillator gamma-ray detectors with silicon photomultiplier readouts for high-energy astronomy,* in "Society of Photo-Optical Instrumentation Engineers (SPIE) Conference Series," , vol. 8859 of *Society of Photo-Optical Instrumentation Engineers (SPIE) Conference Series*

(2013), vol. 8859 of *Society of Photo-Optical Instrumentation Engineers (SPIE) Conference Series*, p. 0.

[111] B. Sanaei, M. T. Baei, and S. Z. Sayyed-Alangi, *Characterization of a New Silicon Photomultiplier in Comparison with a Conventional Photomultiplier Tube,* Journal of Modern Physics **6**, 425–433 (2015).

[112] M. L. McConnell, C. Bancroft, P. F. Bloser, T. Connor, J. Legere, and J. M. Ryan, *GRAPE: a balloon-borne gamma-ray polarimeter,* in "Society of Photo-Optical Instrumentation Engineers (SPIE) Conference Series," , vol. 7435 of *Society of Photo-Optical Instrumentation Engineers (SPIE) Conference Series* (2009), vol. 7435 of *Society of Photo-Optical Instrumentation Engineers (SPIE) Conference Series*, p. 0.

[113] M. Pearce, H.-G. Florén, M. Jackson, T. Kamae, M. Kiss, M. Kole, E. Moretti, G. Olofsson, S. Rydström, J.-E. Strömberg, and H. Takahashi, *Balloon-borne hard X-ray polarimetry with PoGOLite,* ArXiv e-prints (2012).

[114] Y. Dong, *The x-ray timing and polarization satellite - 1, 2, 3: uncovering the mysteries of black holes and extreme physics in the universe,* in "Society of Photo-Optical Instrumentation Engineers (SPIE) Conference Series," , vol. 9144 of *Society of Photo-Optical Instrumentation Engineers (SPIE) Conference Series* (2014), vol. 9144 of *Society of Photo-Optical Instrumentation Engineers (SPIE) Conference Series*, p. 3.

[115] B. Paul, P. V. Rishin, C. Maitra, M. R. Gopalakrishna, R. Duraichelvan, C. M. Ateequlla, R. Cowsik, J. Devasia, and J. Marykutty, *Thomson X-ray Polarimeter for a Small Satellite Mission,* in "The First Year of MAXI: Monitoring Variable X-ray Sources," (2010), p. 68P.

[116] S. V. Vadawale, P. Sreekumar, Y. B. Acharya, M. Shanmugam, D. Banerjee, J. N. Goswami, N. Bhandari, C. N. Umapathy, M. R. Sharma, A. Tyagi, M. Bug, M. Sudhakar, and L. Abraham, *Hard X-ray continuum from lu-*

nar surface: Results from High Energy X-ray spectrometer (HEX) onboard Chandrayaan-1, Advances in Space Research **54**, 2041–2049 (2014).

[117] S. Watanabe, H. Tajima, Y. Fukazawa, R. Blandford, T. Enoto, J. Kataoka, M. Kawaharada, M. Kokubun, P. Laurent, F. Lebrun, O. Limousin, G. Madejski, K. Makishima, T. Mizuno, T. Nakamori, K. Nakazawa, K. Mori, H. Odaka, M. Ohno, M. Ohta, G. Sato, R. Sato, S. Takeda, H. Takahashi, T. Takahashi, T. Tanaka, M. Tashiro, Y. Terada, H. Uchiyama, Y. Uchiyama, S. Yamada, Y. Yatsu, D. Yonetoku, and T. Yuasa, *Soft gamma-ray detector for the ASTRO-H Mission,* in “Society of Photo-Optical Instrumentation Engineers (SPIE) Conference Series,” , vol. 8443 of *Society of Photo-Optical Instrumentation Engineers (SPIE) Conference Series* (2012), vol. 8443 of *Society of Photo-Optical Instrumentation Engineers (SPIE) Conference Series*, p. 26.

[118] H. Tajima and et al., *Polarimetry with ASTRO-H soft gamma-ray detector,* in “X-ray Polarimetry: A New Window in Astrophysics by Ronaldo Bellazzini, Enrico Costa, Giorgio Matt and Gianpiero Tagliaferri. Cambridge University Press, 2010. ISBN: 9780521191845, p. 275,” (2010), p. 275.

[119] T. E. Strohmayer and T. R. Kallman, *On the Statistical Analysis of X-Ray Polarization Measurements,* Astrophysical Journal **773**, 103 (2013).

[120] J. Dyks, A. K. Harding, and B. Rudak, *Relativistic Effects and Polarization in Three High-Energy Pulsar Models,* Astrophysical Journal **606**, 1125–1142 (2004).

[121] J. Pétri and J. G. Kirk, *The Polarization of High-Energy Pulsar Radiation in the Striped Wind Model,* Astrophysical Journal Letter **627**, L37–L40 (2005).

[122] W. H. Baumgartner, J. Tueller, C. B. Markwardt, G. K. Skinner, S. Barthelmy, R. F. Mushotzky, P. A. Evans, and N. Gehrels, *The 70 Month Swift-BAT All-sky Hard X-Ray Survey,* Astrophysical Journal Supplement **207**, 19 (2013).

[123] D. Yonetoku, T. Murakami, S. Gunji, T. Mihara, K. Toma, T. Sakashita, Y. Morihara, T. Takahashi, N. Toukairin, H. Fujimoto, Y. Kodama, S. Kubo, and IKAROS Demonstration Team, *Detection of Gamma-Ray Polarization in Prompt Emission of GRB 100826A,* Astrophysical Journal Letter **743**, L30 (2011).

[124] S. D. Barthelmy, L. M. Barbier, J. R. Cummings, E. E. Fenimore, N. Gehrels, D. Hullinger, H. A. Krimm, C. B. Markwardt, D. M. Palmer, A. Parsons, G. Sato, M. Suzuki, T. Takahashi, M. Tashiro, and J. Tueller, *The Burst Alert Telescope (BAT) on the SWIFT Midex Mission,* Space Science Reviews **120**, 143–164 (2005).

[125] P. Ubertini, F. Lebrun, G. Di Cocco, A. Bazzano, A. J. Bird, K. Broenstad, A. Goldwurm, G. La Rosa, C. Labanti, P. Laurent, I. F. Mirabel, E. M. Quadrini, B. Ramsey, V. Reglero, L. Sabau, B. Sacco, R. Staubert, L. Vigroux, M. C. Weisskopf, and A. A. Zdziarski, *IBIS: The Imager on-board INTEGRAL,* Astronomy & Astrophysics **411**, L131–L139 (2003).

[126] J. Hong, B. Allen, J. Grindlay, N. Chammas, S. Barthelemy, R. Baker, N. Gehrels, K. E. Nelson, S. Labov, J. Collins, W. R. Cook, R. McLean, and F. Harrison, *Building large area CZT imaging detectors for a wide-field hard X-ray telescopeProtoEXIST1,* Nuclear Instruments and Methods in Physics Research A **605**, 364–373 (2009).

[127] G. Sato, T. Takahashi, M. Sugiho, M. Kouda, T. Mitani, K. Nakazawa, Y. Okada, and S. Watanabe, *Characterization of CdTe/CdZnTe detectors,* IEEE Transactions on Nuclear Science **49**, 1258–1263 (2002).

[128] K. Hecht, *Zum Mechanismus des lichtelektrischen Primärstromes in isolierenden Kristallen,* Zeitschrift fur Physik **77**, 235–245 (1932).

[129] E. Kalemci and J. L. Matteson, *Investigation of charge sharing among electrode strips for a CdZnTe detector,* Nuclear Instruments and Methods in Physics Research A **478**, 527–537 (2002).

[130] M. C. Veale, S. J. Bell, D. D. Duarte, A. Schneider, P. Seller, M. D. Wilson, and K. Iniewski, *Measurements of charge sharing in small pixel CdTe detectors,* Nuclear Instruments and Methods in Physics Research A **767**, 218–226 (2014).

[131] A. Castoldi, A. Galimberti, C. Guazzoni, P. Rehak, R. Hartmann, and L. Strüder, *Multi-linear silicon drift detectors for X-ray and Compton imaging,* Nuclear Instruments and Methods in Physics Research A **568**, 89–95 (2006).

[132] D. Yonetoku, T. Murakami, S. Gunji, T. Mihara, K. Toma, Y. Morihara, T. Takahashi, Y. Wakashima, H. Yonemochi, T. Sakashita, N. Toukairin, H. Fujimoto, and Y. Kodama, *Magnetic Structures in Gamma-Ray Burst Jets Probed by Gamma-Ray Polarization,* Astrophysical Journal Letter **758**, L1 (2012).

List of Publications

Publications in Journals

1. **Compton polarimeter as a focal plane detector for hard X-ray telescope: sensitivity estimation with Geant4 simulations.**
   T. Chattopadhyay, S. V. Vadawale, J. Pendharkar
   Experimental Astronomy, vol – 35, page – 391, year – 2013
   doi: 10.1007/s10686-012-9312-3

2. **Measurement of Low energy detection efficiency of a plastic scintillator - Implications on the lower energy limit and sensitivity of a hard x-ray focal plane compton polarmeter.**
   T. Chattopadhyay, S. V. Vadawale, M. Shanmugam, S. K. Goyal
   Astrophysical Journal Supplement Series, vol – 212, page – 12, year – 2014
   doi: 10.1088/0067-0049/212/1/12

3. **Prospects of hard X-ray polarimetry with Astrosat-CZTI.**
   T. Chattopadhyay, S.V. Vadawale, A. R. Rao, S. Sreekumar, D. Bhattachariya
   Experimental Astronomy, vol – 37, page – 555, year – 2014
   doi: 10.1007/s10686-014-9386-1

4. **Hard X-ray Polarimetry with Astrosat-CZTI.**
   S. V. Vadawale, **T. Chattopadhyay**, A. R. Rao, D. Bhattacharya, V. B. Bhalerao, N. Vagshette, P. Pawar, S. Sreekumar
   Astronomy & Astrophysics, vol – 578, id.A73, year – 2015
   doi: http://dx.doi.org/10.1051/0004-6361/201525686

5. **Development of a Hard X-ray focal plane Compton Polarimeter: A compact polarimetric configuration with Scintillators and Si photomultipliers.**
   T. Chattopadhyay, S. V. Vadawale, S. K. Goyal, Mithun N. P. S., A. R. patel, R. Shukla, T. Ladiya, M. Shanmugam, V. R. Patel, G. P. Ubale
   Experimental Astronomy, year − 2015
   doi: 10.1007/s10686-015-9481-y

Full Length Conference Papers

1. **A conceptual design of hard X-ray focal plane detector for simultaneous x-ray polarimetric, spectroscopic, and timing measurements.**
   S. V. Vadawale, **T. Chattopadhyay**, J. Pendharkar
   Proc. SPIE, vol − 8443, 2012
   doi: 10.1117/12.935295

2. **Prospects of hard X-ray polarimetry with Astrosat-CZTI.**
   S. V. Vadawale, **T. Chattopadhyay**, A. R. Rao
   Nuclear Science Symposium and Medical Imaging Conference (NSS/MIC), IEEE, 2013
   doi: 10.1109/NSSMIC.2013.6829564

Papers Under Preparation

1. **Generation of multi-pixel response matrix for CZT detectors.**
   T. Chattopadhyay, S. V. Vadawale, Mithun N. P. S., A. R. Rao, D. Bhattachariya
   To be submitted in Astroparticle Physics

Publications attached with thesis

1. **Measurement of Low energy detection efficiency of a plastic scintillator - Implications on the lower energy limit and sensitivity of a hard x-ray focal plane compton polarmeter.**
   T. Chattopadhyay, S. V. Vadawale, M. Shanmugam, S. K. Goyal
   Astrophysical Journal Supplement Series, vol − 212, page − 12, year − 2014
   doi: 10.1088/0067-0049/212/1/12

2. **Development of a Hard X-ray focal plane Compton Polarimeter: A compact polarimetric configuration with Scintillators and Si photomultipliers.**
   T. Chattopadhyay, S. V. Vadawale, S. K. Goyal, Mithun N. P. S., A. R. patel, R. Shukla, T. Ladiya, M. Shanmugam, V. R. Patel, G. P. Ubale
   Experimental Astronomy, year − 2015
   doi: 10.1007/s10686-015-9481-y.

3. **Prospects of hard X-ray polarimetry with Astrosat-CZTI.**
   T. Chattopadhyay, S.V. Vadawale, A. R. Rao, S. Sreekumar, D. Bhattachariya
   Experimental Astronomy, vol − 37, page − 555, year − 2014
   doi: 10.1007/s10686-014-9386-1